Salinity variability from in situ and satellite retrieved measurements

Meike Sena Martins

Dissertation
submitted for obtaining a doctoral degree
at the Faculty of Mathematics, Informatics and Natural Science
in the Department of Earth Sciences
of the University of Hamburg
April 2016

Dissertation accepted by the
Department of Earth Science, University of Hamburg
under the Examination board:
Prof. Dr. Detlef Stammer
Prof. Dr. Lars Kaleschke

Hamburg, 6^{th} July 2016

Corrected Version

Eidesstattliche Versicherung

Ich versichere an Eides statt, dass ich die Arbeit selbstständig verfasst und keine anderen als die angegebenen Quellen und Hilfsmittel benutzt habe.

Hamburg, den 6.7.2016

Meike Sena Martins
Institute of Oceanography
Universtity of Hamburg
Bundesstr. 53
D-21046 Hamburg
meike.sena-martins@uni-hamburg.de

Abstract

Understanding the changes in the global water cycle due to climate changes is of highest priority in Earth Sciences. The ocean is a principal component of the earth system, and thus part of the global water cycle. The sea surface salinity (SSS) is subject to the atmospheric freshwater forcing and reflects to a certain degree the net sum of evaporation and precipitation. SSS changes therefore are an imprint of global water cycle changes. In order to improve the understanding of the relation between SSS changes and freshwater forcing it is necessary to monitor the global ocean salinity. This monitoring became possible through the Soil Moisture and Ocean Salinity (SMOS) mission by the European Space Agency (ESA), which provides global salinity data with an unprecedented spatial and temporal resolution.

The space born SSS technology is still in a development stage, and a step towards an increased quality of the retrieved SSS is the validation with in situ data. The new data makes new research possible and furthermore provokes to review the statistics needed for producing spatially and temporally averaged SSS fields. Especially, the SSS variability within the footprint of the satellites (50 to 100 km) is so far only poorly documented.

Therefore, the present thesis contributes to the improvement of the SMOS SSS fields, the characterization of the SSS variability and the relation between the SSS and the atmospheric freshwater fluxes.

(1) SSS Variability: The details of the SSS variability in the Atlantic Ocean will be estimated from existing in situ measurements. A high-resolution circulation model of the Atlantic will be used for comparison and extension of the study in scarcely sampled regions. The obtained SSS spatial decorrelation scales of 70 to 100 km are slightly below the estimates of earlier studies, and the variance on small scales is regionally larger than previously estimated, so that the sampling error on the common scales used for averaging is not negligible. These results are published in *Sena Martins et al.* (2015).

(2) Validation and bias-correction of the space born salinity observations of the SMOS mission: The SMOS SSS data still contain inaccuracies and are subject to uncertainties which are described and quantified in the present study. A bias-correction is calculated on the basis of in situ data and applied to the SMOS salinity data. A monthly averaged data set including error estimates was produced and made publicly available at (*http://icdc.zmaw.de/daten/ocean/smos-sss.html*).

(3) Investigation of the relation between the SSS variability and the atmospheric fluxes: The SMOS salinity fields reveal a fresh water anomaly in the south eastern tropical Pacific which recurs seasonally. The assumption that the boreal spring precipitation in the southern Pacific Intertropical Convergence Zone is responsible for this anomaly was investigated in the present study by performing a freshwater budget in the respective region. The linear analysis showed that the precipitation only explains about half of the freshwater anomaly; the advection of fresh water from the north-equatorial Freshwater Pool (EPFP) explains an equal part. The appearance of the freshwater anomaly and the connection to the winterly EPFP are new findings which have been published in *Sena Martins and Stammer* (2015).

Zusammenfassung

Einer der Schwerpunkte der Erdsystemforschung ist es, die Veränderung des globalen Wasserkreislaufs aufgrund des Klimawandels zu verstehen. Der Ozean ist eine Hauptkomponente des Erdsystems, und somit Teil des globalen Wasserkreislaufes. Der Oberflächensalzgehalt (OS) des Ozeans ist den atmosphärischen Süwasserflüssen unterworfen und reflektiert zu einem gewissen Grad die Nettosumme aus Niederschlag und Verdunstung. OS Veränderungen sind daher eng mit dem globalen Wasserkreislauf verknüpft. Um diese Verknüpfung besser zu verstehen, ist die Vermessung des globalen OS notwendig. Das wurde möglich durch die "Soil Moisture and Ocean Salinity" (SMOS) Mission der Europäischen Raumfahrtagentur (ESA), die globale Salzgehaltsdaten mit beispielloser räumlicher und zeitlicher Auflösung liefert.

Die Technik zur Vermessung des OS per Satellit ist noch im Entwicklungsstadium. Ein Prozess zur Verbesserung der SMOS OS Daten ist die Validierung durch in situ Daten. Die neuen Daten ermöglichen neue Forschung, erfordern allerdings auch die Überprüfung der Statistik der in situ OS Daten, die zur Erzeugung der OS Felder und der Validierung der Satellitendaten notwendig ist. Insbesondere die Salzgehaltsvariabilität auf den Skalen des Empfangsbereiches des Satelliten (50 bis 150 km) sind bislang sehr schlecht dokumentiert. Daher trägt diese Arbeit dazu bei, die Details der Salzgehaltsvariabilität zu bestimmen, die satellitengestützten Daten zu verbessern, und die Beziehung zwischen dem OS und den atmosphärischen Süßwasserflüssen näher zu untersuchen.

(1) Salzgehaltsvariabilität: Die Details der OS Variabilität werden im Atlantischen Ozean aus vorhandenen in situ Salzgehaltsmessungen errechnet. Ein räumlich und zeitlich hochauflösendes Zirkulationsmodell des Atlantiks wird als Vergleich und als Erweiterung dieser Studie genutzt. Die sich ergebenden räumlichen OS Dekorrelationsskalen von ca. 70 bis 100 km liegen leicht unter den Angaben vorheriger Studien, und die OS Varianz auf kleinen Skalen ist regional größer als bisher angenommen, sodass ein Sampling-Fehler in den gebräuchlichen Mittelungsintervallen nicht vernachlässigbar ist. Diese Ergebnisse sind in *Sena Martins et al.* (2015) veröffentlicht.

(2) Validierung und Biaskorrektur der OS Satellitenbeobachtungen: Die SMOS Salzgehaltsdaten sind noch ungenau und unterliegen Fehlern, die hier in ihrer zeitlichen und räumlichen Verteilung, sowie in ihrer Abhängigkeit von geophysikalischen Bedingungen dargelegt und abgeschätzt werden. Eine Biaskorrektur wurde auf Basis der in situ Daten errechnet und auf die SMOS OS Daten angewandt. Ein monatlich gemitteltes Salzgehaltsprodukt mit Fehlerangaben ist daraus entstanden und wurde auf *http://icdc.zmaw.de/daten/ocean/smos-sss.html* veröffentlicht.

(3) Überprüfung der Beziehung zwischen den atmosphärischen Süßwasserflüssen und dem Oberflächensalzgehalt (OS): In den satellitengestützten OS Feldern ist eine saisonale Salzgehaltsanomalie im südöstlichen tropischen Pazifik aufgefallen. Die Aufstellung eines Süßwasserbudgets in der betreffenden Region ergab, dass der Frühlingsregen in der südlichen pazifischen

Zusammenfassung

Intertropischen Konvergenzzone nur etwa zur Hälfte für die Salzgehaltsanomalie verantwortlich ist; einen etwa gleich großen Teil trägt der Zustrom aus dem nördlich des Äquators liegenden Süßwasserpool (EPFP) bei. Die neuen Erkenntnisse über die bis dahin kaum dokumentierte Salzgehaltsanomalie im südlichen Pazifik und die Verbindung zum nordäquatorialen EPFP sind in *Sena Martins und Stammer* (2015) veröffentlicht.

Contents

1. Introduction

1.1. Background

Salinity is, besides temperature and pressure, one of the key parameters which determine the density of seawater. Knowledge of the salinity distribution and variability in the ocean is therefore fundamental for any oceanographic and climate research. Whereas salinity changes in the interior of the ocean are driven solely by oceanographic processes such as advection and mixing, the salinity at the sea surface is additionally influenced by atmospheric forcing, runoff from rivers and sea ice melting and freezing. The distribution of the sea surface salinity (SSS) reflects these influences, and presents the effects of the global hydrological cycle (GHC) at the interface between the atmosphere and the ocean.

Processes participating in the GHC are summarized in Fig. 1.1: Water exists on Earth in different states, as ice, gas but mostly in liquid form. These states of water prevail at different places of the world, on land, in the atmosphere and in the ocean. The phase change between these states by evaporation and condensation, sublimation, freezing and melting, and the transport and exchange between the reservoirs of water is called the GHC. Storage in the soil and availability of water on land is most relevant for terrestrial fauna and flora, however, 96 % of the water is stored in the ocean.

Also the exchange of water at the oceans' interface is largest: 86 % of the global evaporation and 78 % of the global precipitation is estimated to happen across the ocean–atmosphere interface. Its quantification is crucial for determining the consequences on weather, climate and ocean dynamics. The exchange of heat and freshwater alters the density of the sea surface layer and thus changes the balance of forces in the ocean's upper layer.

The amount of water fluxes across the ocean's surface and at its boundaries is reflected by the SSS. High salinity due to evaporation or freezing of water increases its density; and dilution i.e. freshwater supply by precipitation, melting or river runoff lightens the water. A direct relation between atmospheric forcing through the net sum of evaporation and precipitation (E–P) and SSS was postulated already by *Wüst* (1936). It was recognized that the knowledge of its distribution improves the characterization of the large-scale water dynamics (*Lagerloef et al.*, 1995). The quantification of the changes in SSS therefore contributes to climate change research. Ocean circulation models as well as ocean models coupled with the atmosphere, benefit from the detailed quantification of SSS changes, since they can be improved in simulating the ocean dynamics and in forecasting weather and climate change.

Global synoptic observations of the SSS in the ocean are necessary to monitor changes in the GHC. So far, trends have been estimated from basin-wide salinity averages from in situ measurements (*Durack and Wijffels*, 2010) which show an intensification of the GHC during the last decades, by turning the salty regions saltier and the wet regions wetter. This corresponds

to results from numerical studies linking the atmospheric temperature increase to a probable enhancement of the GHC (*Held and Soden*, 2006).

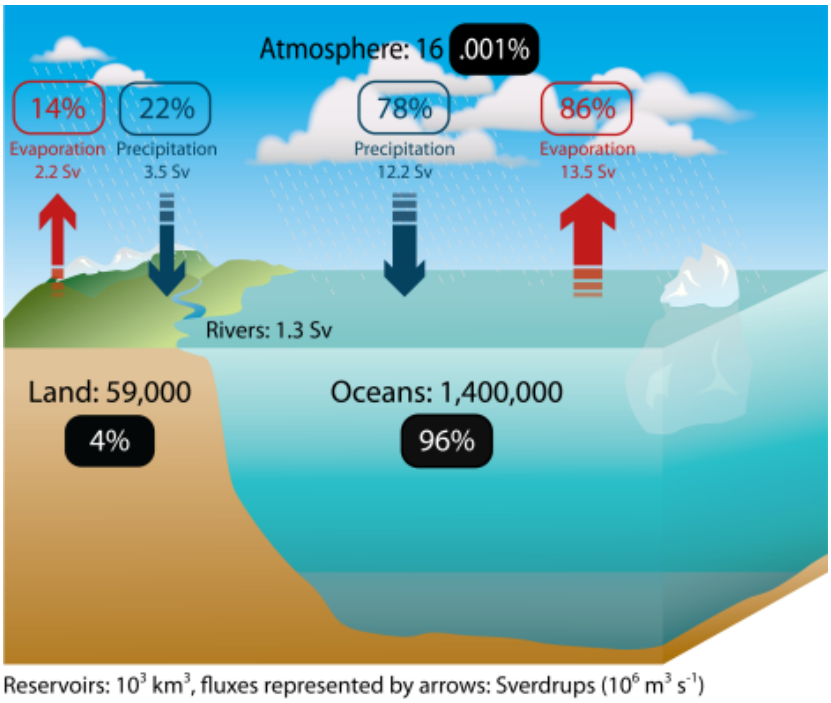

Figure 1.1.: The global water cycle. Credit: Paul Durack/CSIRO

Commonly, the influence of temperature on the density is twice that of salinity in the mixed layer on large scales (*Stommel*, 1993). On smaller scales of the order of 10 km however, salinity changes exert an influence on the density as strong as temperature (*Rudnick and Ferrari*, 1999), hereby, the density of cold water is more sensitive to salinity than temperature. Regionally, salinity plays a key role for water mass formation. Water mass characteristics, i.e. typical temperature and salinity values, are formed at the surface and are subject to the surface conditions such as heating and cooling, evaporation and precipitation. Usually in the winter months, when cooling prevails, it is the salt content resulting from the atmospheric conditions during the preceding season that determines the density and depth levels to which the water mass is sinking, or to which depth levels the convection occurs. In the following season, the water mass is disconnected from the surface by capping with a seasonally heated surface layer and its water mass characteristics are maintained along its path through the ocean, since the process of mixing is usually slower than advection. Salinity anomalies can be followed (e.g. *Dickson et al.*, 1988), and mean advection rates can be deduced when knowing the surface conditions and the sea surface salinity at its origin. Thus, salinity is a good "tracer" of water masses and is often well correlated to biogeochemical characteristics (e. g. *Lefèvre et al.*, 2010).

Although the importance of a better understanding of the GHC and of the role played by SSS is obvious, until recently it has been very difficult to measure salinity on a synoptic scale

and with sufficient resolution. Salinity is usually measured in situ, from a seawater sample as a conductivity ratio to a standard water probe. However, the data availability has been scarce, especially in remote areas and in regions of harsh weather. An improvement of data availability has been reached in the beginning of 2000 by the Argo program: the autonomous profiling floats were developed in the nineties and are being deployed in the global oceans in high numbers by 27 contributing nations from 2000 onwards. Nowadays, the Argo floats gather routinely 300 conductivity, temperature and pressure profiles per day in the global ocean, providing on average at least one measurement each 10 days in a box of $3\,^{\circ}\times\ 3\,^{\circ}$. However, this frequency and data coverage still does not produce the high temporal and spatial resolution we need to monitor salinity in the ocean, since vast regions of the global ocean are not sampled on a regular basis.

In situ salinity is actually not measured but calculated from measured temperature, conductivity and pressure and is reported on the practical salinity scale (*UNESCO and IAPSO*, 1981). The scale is developed from the conductivity of the Standard Seawater (or SSW) which is seawater with a particular composition of salts, obtained from a reference material (IAPSO Standard Seawater). As the composition of salts in the seawater can change regionally or temporally, the calculation of the salt content using the practical salinity scale is not correct. However, the actual composition of salts in a water probe is difficult to measure, and therefore the practical salinity scale is and will be still in use. Salinity is often given in practical salinity units (psu) because the salinity represents only the ratio (g salt in 1 kg of water) and thus has no physical units. However, the use of psu is not recommended by *IOC and IAPSO* (2010), therefore, in this thesis salinity is used without any units to meet the recommendations of *IOC and IAPSO* (2010). Only the absolute salinity denoted by S_A, actually also a unitless quantity, has the SI units g/kg in order to express the absolute weight of the different salts in 1 kg of water.

The accuracy of in situ salinity data is 0.002 for single CTD stations and 0.01 for the Argo profilers. This high accuracy is necessary for the study of water mass formation and variability. Moreover, small salinity variations are important for the dynamics in the ocean: a salinity change of 0.1 over 100 km corresponds to a change in density by only about $75\,\mathrm{g/m^3}$, less than 0.01 % of the total density. But when applying simple geostrophic estimates, this relates to a geostrophic surface velocity change of several cm/s.

Salinity in the surface layer varies between 34 and 37 in vast parts of the global ocean. Extreme values of salinity are found in arid regions like the Mediterranean Sea or the Red sea, where salinity values exceed 40. In contrast, very low salinity, with values less than 20, occurs e.g. in the Baltic sea and in the Arctic ocean shelfs. However, relevant for the global ocean are the high values in the subtropical areas around 37.4, and low salinity in the regions of strong river run-off and ice melting in the polar regions, leading to regionally averaged salinity values of 30. The amplitude of salinity variability in most regions of the global ocean amounts to several tenth, the annual amplitude in 37 % of the global ocean area between 60 °S and 60 °N is 0.19 (*Bingham et al.*, 2012). The same authors report that in most tropical and subtropical ocean regions the annual and semiannual variability explains up to 60 % of the total variability. These overall estimates lead the oceanographic community to claim the need for an accuracy in salinity for the SMOS mission of at least 0.1 on large scales.

While sea surface temperature (SST) has been measured from space by satellites already since several decades, it is only since recent years, that the scientific community is able to monitor salinity from space after the launch of the ESA's SMOS mission in November 2009 and the National Aeronautics and Space Administration's (NASA) Aquarius mission in June 2011. Advantage is taken from the fact that the brightness temperature at L-Band (1.4 GHz) is sensitive to the sea surface salinity and less sensitive to temperature (*Njoku et al.*, 2000). Moreover, this frequency band is legally protected from human-made emissions. An interferometric technology is used to help overcome the limitation which the needed antenna size imposes on microwave remote sensing from space.

The data products from those satellite missions allow to calculate monthly SSS maps of the global ocean with a resolution of 100 km×100 km. The theoretically possible accuracy is about 0.1 for temporally and spatially averaged maps. With those high-resolution salinity fields, interannual variability in regions of strong salinity signals has been monitored, like it has never been possible before; e.g. the Amazon river discharge and its pattern of fresh water distributing across the tropical Atlantic (*Reul et al.*, 2013); or the imprint of the monsoon in the Indian ocean, reflecting the phases of the Indian Ocean Dipole (*Durand et al.*, 2013).

However, the sensitivity of the brightness temperature to salinity is low and depends on sea surface temperature, incidence angle, and sea surface roughness. Many disturbing phenomena influence the radiometer's measurements which have to be corrected. The validation is still in progress and the quality of the data is not yet satisfactory. Characterizing the bias in the salinity retrieval and proposing corrections of the bias based on existing in situ data is of highest importance for increasing the quality of the SMOS salinity data. The different steps to a high quality and validated salinity data product inspires basic research not only in the improvement of the complex salinity retrieval algorithms but also in the exploration of the in situ data acquired so far.

Detailed knowledge of salinity variability is still missing. In situ data are gathered pointwise, section-wise and on non-synoptic scales. A collection of data is usually gridded and objectively analysed to produce salinity maps within certain intervals of averaging. Using as many data as possible, the unknown variability on small scales, so called "noise", is reduced. But the often underestimated small scale variability is important for estimating the representativeness of a single measurement provided, e.g., by the Argo profilers. The spatial and temporal SSS variability within a satellite footprint (between 50 km and 150 km) is also relevant for the satellite retrieved SSS validation. Especially in frontal regions, or regions where the SSS is influenced by river runoff or strong, intermittent precipitation, the SSS variability is often unknown. In other regions, frequently sampled by thermosalinographs on merchant ship lines, the SSS variability on a scale of 100 km is estimated to be 0.1 in 25 % of grid boxes (*Boutin et al.*, 2015). However, the statistics of the global SSS variability are poorly documented. One of the open questions, which will be addressed in this thesis, is therefore the SSS variability on the scales typically used for producing the SSS maps. The results contribute not only to fill this gap, but are also relevant for the processing of the SSS data retrieved from satellite measurements, in terms of averaging scales and in terms of validation. The accuracy of the space born salinity fields cannot be claimed if the sampling error or the salinity variability in the intervals of averaging are unknown.

Another question is how far the SSS changes reflect the atmospheric fresh water input or ocean processes. On the one hand we know from global maps, that the SSS distribution follows roughly the patterns of the satellite derived estimates of the atmospheric fresh water forcing (E–P), however, these contain strong uncertainties. Thus, as the ocean salinity is better observed than P or E, its monitoring could also contribute to better understand the pattern and variability of the E–P field (*Sommer et al.*, 2015). On the other hand, fresh water budgets show that the atmospheric freshwater forcing accounts for only part of the SSS changes, other contributions are due to oceanographic processes (*Yu*, 2011; *Hasson et al.*, 2013b). Therefore, another focus of this thesis deals with the effects of the freshwater forcing on the SSS in the tropical eastern Pacific. In that region the mixed layer is very shallow, currents and winds are weak, and evaporation is quite constant, so that the precipitation is assumed to exert a direct effect on the SSS.

1.2. Addressed open questions

The following three questions, introduced above, will be addressed:

1. **What are the characteristics of the sea surface salinity variability in the existing in situ data; how large is the salinity variability within the averaging time and space intervals used for typical fields of salinity products?**
2. **What is the accuracy of the SMOS sea surface salinity and how suitable are the in situ data for validation and bias correction?**
3. **At what extent does the atmospheric freshwater forcing contribute to changes in the sea surface salinity?**

1.3. Outline

Data basis

A huge in situ data base exists from several international observational programs from which the information about the upper ocean salinity is extracted, quality controlled and compiled for use in the different investigations. In this chapter the origin and deliberate selection of these data sets are presented. A special in situ data set is created from surface drifters equipped with a conductivity cell. The use of drifters for the validation of satellite derived salinity is a pilot study, and the drifters' salinity data quality for this purpose still has to be proven. Therefore this chapter comprises the drifters' data processing and validation. The measurement principle and the processing of the data from the SMOS mission will be summarized. Other data used are the SSS output from an ocean circulation model, an atmospheric flux product and velocity data from a combined data set using drifters and satellite observations.

Spatial and temporal scales of sea surface salinity variability in the Atlantic Ocean

This particular study aims at characterizing the SSS variability, investigating the in situ data gathered in the Atlantic Ocean over more than 30 years, complemented by a high-resolution

simulation of the Atlantic circulation.

Detailed estimates of the amplitude of the annual SSS cycle in the Atlantic Ocean are presented, and the fraction of the annual cycle from the total salinity variability is estimated for all regions. The comparison between observational and model results validates the model to sufficiently simulate the SSS variability. Subsequently, spatial and temporal decorrelation scales are computed from observational and model data. Missing model physics account for the minor differences. Additionally, the influence of the relaxation of the SSS to climatological fields, which is used in the circulation model in order to prevent a long term drift, is evaluated. The sampling error within the averaging time and space intervals used for typical fields of salinity products is quantified. The results of this study are published in *Sena Martins et al.* (2015).

Validation of the sea surface salinity from SMOS

Numerous in situ data are used here to validate the SMOS salinity on a global scale and for the period 2010 to 2014, and to infer the dependence of the salinity retrieval from geophysical parameters such as wind and temperature. Moreover, the retrieval deficiencies due to the so-called land contamination and the dependence on latitude are estimated.

Weekly maps of salinity bias are computed on the basis of the difference between satellite retrieved and in situ salinity. An empirical bias correction is applied to the SMOS salinity, and a data set of monthly, bias-corrected SMOS salinity is compiled. The new data are validated with monthly maps from other data centres and from independent data showing significant improvement to the biased data.

Freshwater Variability underneath the Pacific double ITCZ

This chapter addresses the co-variability of the precipitation and SSS. The focus of the present study is on the eastern tropical Pacific where the mixed layer depth is shallow and the pycnocline is strong. There, even weak precipitation should leave a clear imprint in SSS fields so that it is particularly suited for investigating whether SSS signals may serve as a "rain gauge".

A novel finding from the innovative satellite monthly salinity fields consists in a thin, short living band of less saline water along about 5 °S in the eastern Pacific which could be shown by the SMOS mission for the first time, since the monthly fields constructed by optimal interpolation are too smooth to reveal this phenomenon. The fresh anomaly is associated with precipitation in the south equatorial Pacific Intertropical Convergence Zone. The occurrence and forcing of this pattern is analyzed in detail on the basis of particular in situ data. The results of this study have been published in *Sena Martins and Stammer* (2015).

Summary and Conclusion

This chapter summarizes the results of the three main parts, concerning the salinity data variability, the SSS data accuracy and the relation between the atmospheric forcing and SSS. Recommendations concerning needed resolution and accuracy are expressed in anticipation of future salinity observation missions, either in situ or space born ones.

2. Data basis

The study is based on satellite and on in situ observations, on the ouput of a circulation model and on other data products. All data sources are described in the next subsections.

2.1. Satellite derived salinity data

The SMOS mission, one of the ESA Explorer Opportunity science missions, was designed with the main objective of observing sea surface salinity (SSS) and soil moisture over land for understanding the global water cycle. The main goal of the mission is to obtain fields of SSS on a basis of averaged time spans of 10 or 30 days and spatial averages of 100 to 200 km. The aimed accuracy is at 0.1 to 0.2, which seems to be possible when looking at the theoretical salinity retrieval errors reduced by temporal and spatial averaging, and which is necessary to monitor interannual variations of salinity during phenomena such as El Niño and the Southern Oscillation (ENSO) or the Indian Ocean Dipol (IOD), as well as annual variations wherever the seasonal amplitude of SSS reaches an amplitude of at least 0.2.

2.1.1. The SMOS Satellite

The SMOS satellite was launched in November 2009 into a sun-synchronous polar orbit at a mean altitude of 755 km, with an inclination of 98.44 °. The local equator crossing time is at 6:00 AM on ascending node and 6:00 PM on descending node. Within 2.7 days a global coverage is reached. The exact repeat cycle of a single orbit is 149 days. The SMOS satellite carries a radiometer antenna with 69 Lightweight Cost-Effective Front-end (LICEF) receivers, arranged on 3 arms mounted in an Y-shaped construction (Fig. 2.1). Each module detects radiation in the microwave L-band, both in horizontal and vertical polarisation. The SMOS spacecraft's boresight of the antenna is forward tilted by 32.5 ° with respect to nadir. This configuration enables measurements at line-of-sight angles between 0 °–50 °.

The arrangement and orientation of the Microwave Imaging Radiometer using Aperture Synthesis (MIRAS) makes the instrument a two dimensional interferometric radiometer which allows to generate the brightness temperature images. In aperture synthesis, one measures the correlation of signals from pairs of antennas at different spacing. Each spacing provides a sample point in the Fourier spectrum of the scene. The brightness temperature of the source is computed as the inverse Fourier transform of the so-called visibility function (*Corbella et al.*, 2004; *Le Vine et al.*, 1994). This inversion or image reconstruction process involves an antenna model for the conversion of visibilities into brightness temperatures. Moreover, the calculation of the full set of visibilities in the data processing requires the correction of the instrument drifts in amplitudes, phases and offsets of each of the subsystems. This is described in *Corbella*

et al. (2010); *Oliva et al.* (2013).

A snapshot brightness temperature map in the field of view (FOV) is taken every 1.2 seconds and due to the platform motion in orbit, each pixel is measured several times with different spatial and radiometric resolutions and incidence angles. The minimum FOV along-track dimension is about 800 km. The average resolution of SMOS satellite is about 43 km, ranging from 35 km in the centre of the swath to about 80 km at the edges. MIRAS has two types of in-orbit calibration: external, in which the instrument makes a maneuver to point to the cold sky, and internal, in which noise is injected to the receivers.

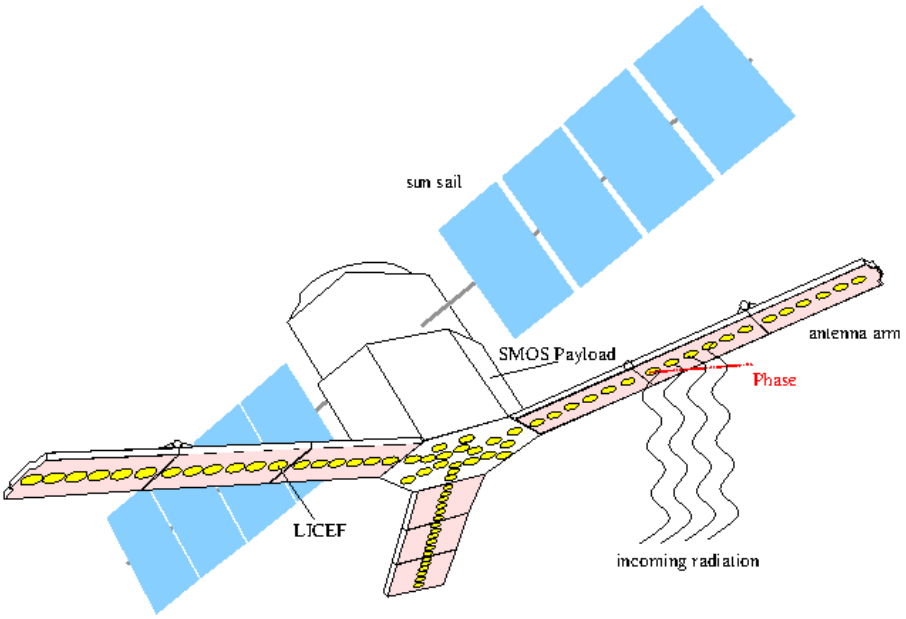

Figure 2.1.: Schematic presentation of the antenna configuration on the SMOS satellite. LICEF are the Lightweight Cost-Effective Front-end receivers.

2.1.2. Measurement principle

Physical Background

According to the theory of (*Planck*, 1901), an ideal black body completely absorbs the incident electromagnetic energy at all frequencies and emits the energy again at all frequencies after having reached its thermal equilibrium. Thereby, the radiated energy spectrum depends only on its physical temperature T_0 and on frequency f.

With h_P the Planck's constant ($h_P = 6.63 \cdot 10^{-14} Js$), c the light speed in vacuum ($c = 3 \cdot 10^8 ms^{-1}$) and k_B the Boltzmann konstant ($k_B = 1.38 \cdot 10^{-23} JK^{-1}$) the spectral radiation density B_f is after *Planck* (1901)

$$B_f = \frac{2h_P f^3}{c^2} \frac{1}{e^{\frac{h_P f}{k_B T_0}} - 1} \tag{2.1}$$

For L-Band, i.e. in the frequency range used by the SMOS antenna, $h_P f << k_B T_0$ and the above equation simplifies to the Rayleigh Jeans law:

$$B_f \simeq \frac{2k_B f^2 T_0}{c^2} = \frac{2k_B T_0}{\lambda^2} \tag{2.2}$$

In reality the Earth does not behave as an ideal black body or a perfect emitter, but emits a smaller energy than the ideal black body at the same physical temperature T_0. Its spectral radiation density B_f is

$$B_f \simeq \frac{2k_B T_B}{\lambda^2} \tag{2.3}$$

with T_B being the brightness temperature of the Earth.

The relationship between the spectral density of the Earth to the one from an ideal black body (B_{ideal}) is equal to the relation of the Earth's brightness temperature T_B and its physical temperature, the sea surface temperature (SST). This ratio is called emissivity e and

$$e = \frac{B_f}{B_{ideal}} = \frac{T_B}{SST}, \text{ with } 0 \leq T_B \leq SST, \tag{2.4}$$

or

$$T_B = e\, SST. \tag{2.5}$$

The emissivity is dependent on frequency f and is related to the dielectric properties of the sea surface (ϵ is the dielectric constant of seawater). In the case of seawater, it is dependent on conductivity that in turn is a function of salinity. In the frequency band of SMOS the captured radiation is emitted from the first cm of the ocean (*Font et al.*, 2004). The choice of the L-Band with a wavelength of 21 cm, the hydrogen band, is due to a much better radiative signature of salinity and moisture in microwave than at higher frequencies. It has the advantage of penetrating the clouds, i.e. the radiation is not absorbed by the humidity in the atmosphere. Moreover, it is a protected band in radio astronomy, i.e. it is forbidden to use this band for other purposes than for science.

The incident radiation from the Earth's surface upon an antenna may contain components originating from different sources such as the radiation from the atmosphere or the radiation from the atmosphere that is reflected at the Earth surface. This leads to the definition of the apparent radiometric temperature T_{AP}, which is the brightness temperature measured at the top of the atmosphere. T_{AP} can be approximated by a radiative transfer model which includes a sum of different contributors:

$$T_{AP} = e^{-\tau}(T_B + \Gamma(e^{-\tau} T_{COS} + T_{DN})) + T_{UP} \tag{2.6}$$

the surface contribution (T_B) attenuated by the atmosphere's opacity ($e^{-\tau}$); the atmospheric contribution already attenuated by the atmosphere on the way to the earth's surface (T_{DN}), then reflected (Γ) and attenuated by the atmosphere ($e^{-\tau}$) again; the cosmic background (T_{COS}) attenuated by the atmosphere ($e^{-\tau}$) on the way to the earth's surface, then reflected (Γ), scattered and attenuated by the atmosphere again; and the direct atmospheric contribution from the atmosphere (T_{UP}). For a schematic presentation see Fig. 2.2. To estimate the emitted T_B the other effects have to be corrected.

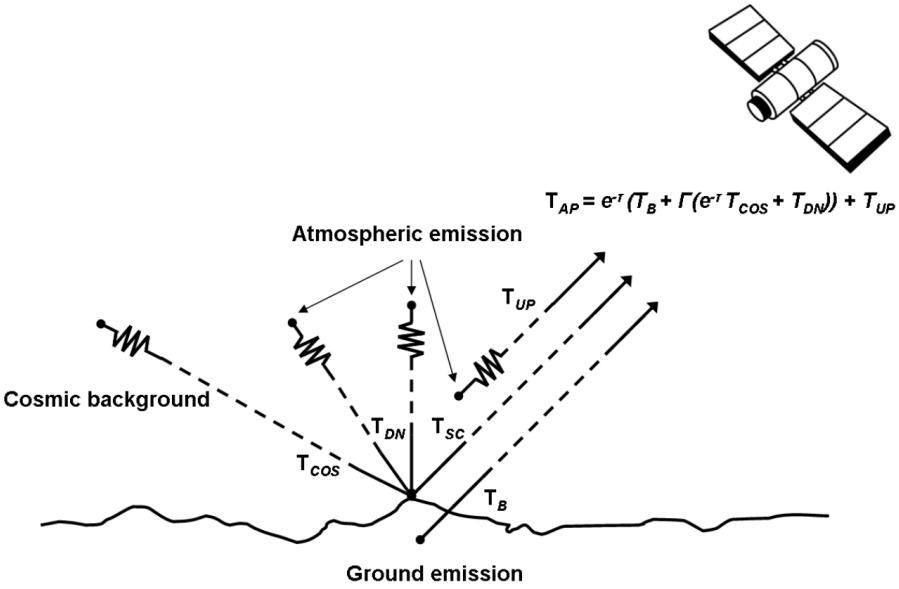

Figure 2.2.: Schematic presentation of the radiation influences on the apparent brightness temperature measured by the satellite (*Talone*, 2010).

Sea surface emission

For the flat sea the emissivity at thermal equilibrium can be written as $e = 1 - \Gamma$, Γ being the reflectivity of the sea surface, and the $T_{B,flat}$ is described by the Fresnel law :

$$T_{B,flat}(f,\theta,p) = e^{sp}(f,\theta,p)SST = (1 - \Gamma^{sp}(f,\theta,p))SST \tag{2.7}$$

with Γ^{sp} being the specular reflectivity, a function of frequency (f), the incidence angle (θ) and the polarisation p.

The specular reflection is expressed by the Fresnel coefficients (*Ulaby et al.*, 1982) for the horizontal and vertical polarization:

$$\Gamma_V^{sp}(\theta) = \left| \frac{\sqrt{\epsilon - \sin^2(\theta)} - \epsilon \cos(\theta)}{\sqrt{\epsilon - \sin^2(\theta)} + \epsilon \cos(\theta)} \right|^2 \quad \text{and} \quad \Gamma_H^{sp}(\theta) = \left| \frac{\sqrt{\epsilon - \sin^2(\theta)} - \cos(\theta)}{\sqrt{\epsilon - \sin^2(\theta)} + \cos(\theta)} \right|^2 \tag{2.8}$$

These coefficients depend on the relative permittivity (ϵ) or the dielectric constant. This constant depends on the physical properties of sea water, i.e. SSS and SST, and on the frequency. In the context of SMOS, the model of the dielectric constant given by *Klein and Swift* (1977) is used.

Usually, the sea surface is not flat but affected by wind causing waves and often also foam. Both, waves and foam, result in scattering the electromagnetic radiation of the sea surface. Whereas satellite scatterometers use signals of the back scattering from wind-generated capillary-gravity waves, which are generally in equilibrium with the near-surface wind over the

ocean (known as Bragg scattering) at a specific wavelength, the roughness contribution to a radiometer signal is simulated by specific models. As described in *Guimbard et al.* (2012) the surface is divided into a foam free and a foam covered area within the radiometer footprint. In the forward model a part simulating the contribution of the foam covered area and a coverage parameter F have to be introduced:

$$T_B = (1 - F)\, T_{foam,free} + F\, T_{foam}. \tag{2.9}$$

The foam free area can be divided into an ideal flat sea surface term $T_{B,flat}$ (see above) and a term accounting for roughness characteristics of the sea surface T_r:

$$T_{foam,free} = T_{B,flat} + T_r \tag{2.10}$$

$T_{B,flat}$ is the specular contribution of a perfectly flat sea surface which explains most of the sea surface emissivity. T_r can be viewed as a correction term taking into account sea surface roughness impact and foam contribution (*Guimbard et al.*, 2012).

Wave spectra depend on the sea state, which is influenced by surface wind speed (WS) and its history, the surface currents, atmospheric stability, and swell. The relationship between the atmospheric WS and the radiometric signal is very complex, and a function of more parameters. For the roughened sea surface a correction term in three different models were developed. Three of them are applied for the SMOS data:

S1: **The two-scale model and foam model**
The two scale model is based on a semi-analytic spectrum model by *Durden and Vesecky* (1985) which has been widely used to simulate T_r at L-band. In the two-scale model, the sea surface is modeled as the superposition of small waves upon large waves. Small scales are sea waves whose height is small compared to the radiometer wave length and large scales are waves whose curvature radius is large compared to the radiometer wave length.
A weighted average of the curvature wave spectrum over a broad range of wavelengths spanning gravity–capillary and short gravity waves is used, whose weights depend on the radiometer wavelength and on incidence angles (*Dinnat et al.*, 2002; *Johnson and Zhang*, 1999). In addition to a roughness model, a foam coverage model is applied which is based on *Monahan and O'Muircheartaigh* (1986). For both models updated parametrizations were calculated from the first L-Band data from SMOS in version 5.50.

S2: **The Small Perturbation Method**: The SPM/SSA (Small Perturbation Method/ Small Slope approximation) applies standard small perturbation theory to predict the bistatic scattering coefficients of a rough surface, and integrates these scattering coefficients to obtain the reflectivities and hence brightness temperatures (*Johnson and Zhang*, 1999). The weighting functions of the second order emission harmonics demonstrate that the brightness temperature prediction has the highest sensitivity to short scale waves, i.e. on the order equal to the electromagnetic wavelength on the ocean surface (*Johnson and Zhang*, 1999).

S3: **The empirical method**: The models above describe the increment on T_B in a theoretical basis. In contrast, the empirical model describes the change in T_B through several

physically measurable parameters and coefficients which are derived from measurements. It was developed at the SMOS Barcelona Expert Center (SMOS-BEC) using WISE oil-platform campaign measurements (Gab). The most important parameter that affects the roughness of the sea is the WS, but the spectra as described by the models above e.g. do not include swell, which may affect the T_B by several tenths of degree; also the direction of the wind may affect the horizontal and vertical polarisations in a different way at high wind speeds (*Camps et al.*, 2003). The empirical model therefore considers the incidence angle, the neutral WS from the WS components, the wind direction and the wave height, obtained from the ECMWF wave model. It does not involve a special foam model, because this is already included in the empirical model.

Inversion

From the preceding considerations, a geophysical so called 'forward' model of the brightness temperature at the antenna frame is computed, which is assumed to be modulated by the geophysical parameters such as SST, SSS, and the WS for the roughness contribution. As described in *Zine et al.* (2008), a maximum-likelihood Bayesian approach is used, taking advantage of the a priori data P_i of the geophysical parameters. Errors on T_B and retrieved parameters are assumed to be Gaussian.

The modeled T_B is fitted to a set of measured T_B reconstructed at different incident angles θ by minimizing the cost function:

$$\chi^2 = \frac{1}{N}\sum_{i=1}^{N}\frac{[T_{B_i}^{meas} - T_{B_i}^{model}(\theta_i, P_i, ...)]^2}{\sigma_{T_{B_i}}^2} + \sum_{j=1}^{M}\frac{[P_j - P_{j0}]^2}{\sigma_{P_j}^2} \tag{2.11}$$

Here, N is the number of measurements available for retrieval at different incident angles in horizontal and vertical polarisation, and ranges between 240 at the center to about 20 at the edges of the swath. $T_{B_i}^{model}$ is simulated at incidence angle θ_i using one of the three models for roughness described above, and the error $\sigma_{T_{B_i}}^2 = \sigma_{T_{B_i}^{meas}}^2 + \sigma_{T_{B_i}^{model}}^2$, is composed by the radiometers' noise and the estimated error of the modeled T_B. P_{j0} is the a priori estimate of the geophysical parameters, with an a priori error $\sigma_{P_j}^2$.

A Levenberg and Marquardt least square algorithm (*Marquardt*, 1963) is used to retrieve the geophysical parameters P_i that minimize the cost function. The theoretical error is retrieved from the Jacobian of T_B with respect to the geophysical parameters and from the a posteriori covariance matrix of errors in T_B and geophysical parameters (*Zine et al.*, 2008).

The a priori values for P_{j0} are obtained from the European Centre for Medium-Range Weather Forecast (ECMWF). Some other geophysical parameters have to be used as auxiliary parameters, and one of them is the total electron content (TEC) which is produced by the International Global Navigation Satellite System Service (IGS *Dow et al.*, 2005) or the International Reference Ionosphere model (*Bilitza*, 2001).

2.1.3. ESA SMOS Data processing

Throughout the present study, the SMOS L2 SSS User Data Products (UDP) distributed by ESA were used. These consist of reprocessed data (version 5.50) during the period from 28 January 2010 to 31 December 2013 and non-reprocessed, i.e. operational data during the year 2014, however, processed with the same retrieval version. Whereas during the first months until June 2010, during the commissioning phase, the dual mode is the two basic polarisations, i.e. horizontal (X) or vertical (Y) polarisation were acquired, from July 2010 on, the antenna is used in the full polarization mode. In this mode the antenna records the horizontal and vertical, but also the cross polarisations (XY) and (YX) alternating at each snapshot, i.e. it obtains all components of the Stokes vector.

Besides high radiometric noise, the SMOS L2 SSS data suffer from several disturbances and and temporal biases:

The frequency band used by SMOS, the L-band at about 1.4 GHz, is reserved for scientific use. However, since launch this frequency band was widely used for unauthorised emissions in the 1400-1427 MHz passive band or excessive unwanted emission from systems operating in the adjacent bands. despite the International Telecommunication Union (ITU) recommendations to preserve this band for scientific use. Successful efforts were undertaken by ESA to shut off those illegal radiation sources at least in the European and North Atlantic areas (*Oliva et al.*, 2014), which allowed from May 2012 onwards to retrieve salinity in the northern North Atlantic (*Köhler et al.*, 2015). However, RFI detection and mitigation still remains a problem for the retrieval of salinity and also soil moisture over land (*Soldo et al.*, 2015), especially for low or moderate signal strengths (on the order of 10 K or less *Aksoy and Johnson*, 2013).

Due to imperfect knowledge of the antenna patterns and the instruments characteristics resulting in insufficient antenna calibration, the visibility functions include residual errors (*Anterrieu*, 2007). These systematic errors were corrected by introducing an "Ocean Target Transformation" (OTT) in version 5.50 of the salinity retrieval. This transformation aims at correcting SMOS (T_B) from systematic differences with respect to modeled T_B in the FOV (*Yin et al.*, 2013) in an oceanic region far from land and very low anthropogenic Radio Frequency Interference (RFI) contamination between 45°S and 5°S in the eastern Pacific (*Yin et al.*, 2014). In contrast to the operating mode which uses the preceding 2 weeks for calculating the T_B bias, in the reprocessing mode the bias within the region can be calculated for each day centred in a 2 week interval. The OTT bias correction was done in phase with the Noise Injection Radiometer (NIR) calibration (*Oliva et al.*, 2013), every 10 days. However, the systematic biases vary geographically, so that the SMOS SSS data are still affected by several shortcomes in the salinity retrieval. One of the largest bias is due to the land contamination, deteriorating the salinity in a belt of about 1000 km width around the continents and ice covered areas. Moreover, seasonal and latitudinal biases are still present likely due to the not totally known thermal response of the antenna (*Reul et al.*, 2012; *Boutin et al.*, 2012). Attempts to reduce such biases remain under study. So far they were tried to overcome with a salinity bias correction applied in the L3 products based on in situ salinity fields.

In radiometric measurements from space, as microwave radiation from earth propagates through the ionosphere, the electromagnetic field components are rotated an angle, called Faraday rotation, that depends on the total ionospheric electron content (TEC), the frequency

and the geomagnetic field. At the SMOS operating frequency, the Faraday rotation is not negligible and must be corrected. It is presently estimated using a classical formulation (*Vine and Abraham*, 2002) that makes use of data provided by external sources to get the necessary TEC and geomagnetic field. Improved data processing requires getting the Faraday rotation directly from the radiometric data in a continuous way (*Corbella et al.*, 2015) which will be implemented in future versions of the retrieval algorithms.

The estimates of the TEC for the salinity retrieval are based on the Global Postioning System (GPS) measurements, i.e. external data source, for the version 5.50. It has been shown recently by *Vergely et al.* (2014) that an estimate of the TEC from the SMOS data set itself after spatial averaging and a thorough filtering improves the salinity retrieval compared to the TEC estimate from GPS data, when applied also at the OTT calculation.

I filtered the L2 SSS data by considering the flags according to the recommendations relative to the flag sorting given in *Boutin et al.* (2013), these imply excluding data taken at too low or too high WS ($3\,\mathrm{m/s} < \mathrm{WS} < 12\,\mathrm{m/s}$), a land mask of only 40 km and SMOS SSS data based on T_B measurements with a theoretical salinity retrieval error of < 1.2, a criterion corresponding to a distance of less than 300 km from the satellite center track. Additionally, data with more than 30 % of RFI influence have been discarded. For the purpose of validation, the data were included which revealed WSs out of the range given above. It will be indicated when these data will be used.

As stated e.g. by *Hernandez et al.* (2014), the theoretical error depends to the first order on the number of T_B data used in the SSS retrieval and on Sea Surface Temperature (SST; because of the strong dependency of $\mathrm{d}T_B/\mathrm{dSSS}$ with SST). When averaging the single swath L2 SSS on a grid of $1\,^\circ \times 1\,^\circ$, each retrieved SSS is weighted by the inverse of its theoretical uncertainty (*Yin et al.*, 2013). These data, though averaged spatially and consequently not conserving the spatial resolution for decreasing the noise, are still called L2 data in the following.

2.1.4. Other satellite salinity products

SMOS L3 products from other centers

The thesis also uses data from the Level 3 SMOS SSS product, available from the Barcelona Expert Centre (BEC; for data access see http://cp34-bec.cmima.csic.es/ocean-reprocessed-dataset), which is based on the same data set as described above with the same calibration process by using the southeast Pacific as a reference region for the OTT. BEC only used the third roughness model (*Guimbard et al.*, 2012), and applied geographical, retrieval and geometrical filters to the reprocessed L2 data and then constructed the L3 product by weighted averaging (*Boutin et al.*, 2012). For a detailed Level 3 product description see *SMOS–BEC Team* (2014). For the analyses in chapter 5, a combination of uncorrected SSS data from ascending and descending orbits were used. Respective BEC L3 maps contain SSS averaged over one month, and sampled over a $0.25\,^\circ$ x $0.25\,^\circ$ grid. Remaining uncertainties in SMOS SSS retrievals in the tropical Pacific are especially related to the use of wind data from the European Centre for Medium-Range Weather Forecasts (ECMWF) as proxies of surface roughness information during the retrieval process. As a result, the salinity in the Pacific equatorial band is biased high (*Yin et al.*, 2014). For computing the monthly salinity anomalies I subtracted

the 4 year mean salinity field (2010–2013) from each month.

The Centre Aval de Traitemenent des Donnees SMOS (CATDS) at Ifremer, Plouzané, developed a L3 SMOS SSS product which is based on the ESA L2 user data product V550 as well. Calculating the differences to climatological in situ salinity values for each of the ascending and descending orbit, resulted in maps from which the SMOS salinity was corrected. Because SSS biases are not stable at high latitude, and because an ice mask has not been implemented yet, a mask has been applied at latitudes north of 65 °N and south of 55 °S. An additional bias correction on retrieved SSS was applied that were derived from observed differences between SMOS SSS and WOA 2009 climatology in the 'OTT region' (see below).

This procedure was a similar bias correction which is proposed in the present study, and was made available only recently, in June 2015. It is involved here in the comparison with other L3 satellite products.

Aquarius SSS retrievals

The Aquarius mission is a joint program between the National Aeronautics and Space Administration (NASA) and Argentina's space agency, Comisión Nacional de Actividades Espaciales (CONAE). The Satélite de Applicaciones Científicas (SAC)-D spacecraft was launched in June 2011 and flies at 657 km above Earth in a sun-synchronous, polar orbit, crossing the equator at 6:00 am when descending and 6 pm local time when ascending. The NASA Aquarius/SAC-D instrument carries a passive radiometer operating also in the L-Band at 1.413 GHz. It directly retrieves brightness temperature using three individual horn-antennas, viewing three spatially displaced surface regions with slightly different footprint size. Aquarius carries an active scatterometer providing simultaneous surface roughness measurements within the three surface regions. This information is used in the CAP (Combined Active-Passive) data (http://podaac.jpl.nasa.gov/announcements/2013-06-06_Aquarius_Salinity_Cap_Data). For Aquarius, the FOV is smaller than for SMOS; and the spatial resolution is less than for SMOS. Aquarius provided salinity data with a spatial resolution close to 150 km. In the present study, monthly fields were used which are available on a $1^\circ \times 1^\circ$ geographic grid for the period September 2011 to December 2013. These fields are based on the L3 CAP product (version 3.0), and are available from ftp://podaac-ftp.jpl.nasa.gov/allData/aquarius/L3/mapped/CAPv3/monthly/SCI/. More information about the algorithm and the data validation can be found in *Yueh et al.* (2014) and *Tang et al.* (2014). The version 3.0 contains a bias correction which is based on the comparison to the SSS from the HYbrid Coordination Model (HYCOM). This model is a coupled ocean data assimilation, including Argo profile data for the assimilation . An SST dependent bias was found and adjusted in the Aquarius SSS fields (*Meissner and Scott*, 2014). Aquarius ceased its operation in June 2015.

2.2. Sea Surface Salinity in situ observations

All studies carried out as part of the thesis use in situ salinity measurements, for characterizing the sea surface salinity (SSS) variability in the Atlantic Ocean, for the validation of the satellite SSS retrieval and for the test of the atmospheric forcing being responsible for the SSS variability in the tropical Pacific. The data basis encompasses in situ measurements from a variety of platforms, and were compiled as single measurements or as objectively analyzed monthly fields.

Argo and CTD salinity observations

An essential prerequisite for the analysis of surface salinity performed in the Atlantic Ocean was the compilation of a comprehensive in situ upper-ocean salinity database suitable for the investigation of variability. For that purpose, I collected all available salinity observations obtained through Argo floats, from ship-based conductivity, temperature and depth (CTD) measurements, from moorings and, concerning the thermosalinograph data, collected by research vessels (RV) and voluntary observing ships (VOS). The resulting data set covers the period 1980–2013 and entails roughly 1.2 billion quality-controlled and consistency-checked near-surface salinity measurements.

To date, the most comprehensive in situ near-surface salinity data set with global overage is provided since 2000 by the Argo system (*Gould et al.*, 2004). This global float system collects more than 3000 temperature and salinity profiles every 10 days from the top 2000 m. The Argo data used in the present work were retrieved from the European Argo repository (ftp://ftp.ifremer.fr/ifremer/argo/geo/atlantic_ocean and geo/pacific_ocean) after passing an automated quality control.

For the present study, the near-surface values from the real-time Argo profiles were extracted to form a data set of near-surface salinity and temperature covering the period 2000–2013 in the Atlantic Ocean north of 33 °S. Since the profiling instruments do not provide data directly at the surface but usually stop recording below 4 m, I extracted the uppermost data point in the depth interval 4 to 12 dbar to represent the salinity in the surface layer. As was already shown by *Boutin and Martin* (2006), about 85 % of the Argo surface data points are located between 4 m and 5 m depth. But to what extent mixed layer processes, such as the transient influences of rain events on the surface salinity and the regionally important formation of barrier layers, can be sufficiently observed by the Argo profilers, has yet to be determined. *Henocq et al.* (2010) estimated a vertical salinity gradient due to the influence of rain and revealed possible gradients of 0.1 g kg^{-1} m^{-1} in regions of strong precipitation.

Only Argo data were used, whose quality flags where set to "good". In addition, a further quality check was performed to eliminate remaining outliers. All data values outside of the likely open-ocean salinity range of $[25 - 42]$, as well as those deviating by more than 3 standard deviations from the local mean (within the box considered), were eliminated from further processing. The resulting Argo data in the Atlantic were augmented by other near-surface in situ salinity measurements included in the 1980–2013 EN3 data set (*Ingleby and Huddleston*, 2007), providing additional observations in shelf regions of the North Atlantic usually not populated by Argo floats. For each geographic position only the uppermost data point was kept per profile. The merged data set was further tested for double occurrences and only data

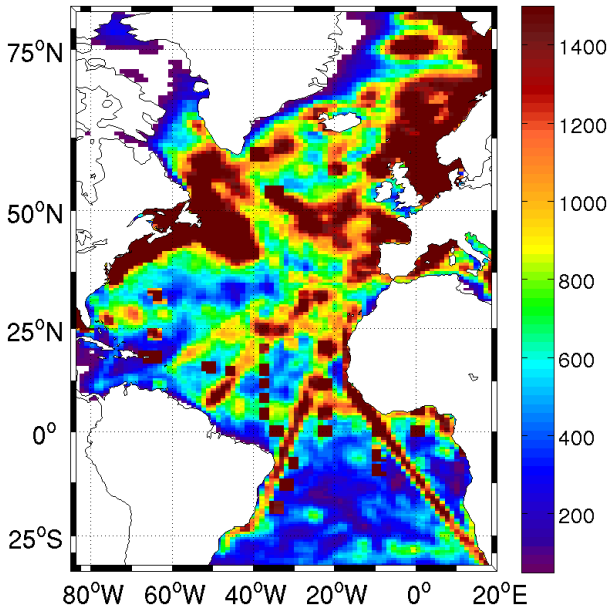

Figure 2.3.: Number of valid in situ salinity observations (between 4 and 12 dbar) in 1.2 ° longitude × 0.6 ° latitude boxes with varying search radius as detailed in the text in the period 1980–2013.

referenced as best quality were kept for further analysis.

The quality-checked data in the Atlantic Ocean were gridded into 1.2 ° × 0.6 ° boxes (in longitude and latitude, respectively) taking into consideration data within a latitudinal-varying search radius, which ranges from about 160 km in the tropics decreasing to about 100 km north of 65 °N. The search radii used imply a certain overlap in the gridding procedure and were chosen as a compromise between involving enough data points, favoring the significance of the results, and on the other hand not smoothing too much the obtained structures. It should be kept in mind that the results shown later are representative of scales within the search distances chosen here, namely 320 km in the tropics decreasing to 200 km north of 65 °N. As no temporal objective mapping or averaging to monthly fields was performed, the analysis does not repeat past efforts based on monthly salinity fields. The aim is to assess the variability one can encounter when analyzing instantaneous data.

Fig. 2.3 shows the amount of data points in the Atlantic Ocean available per grid cell based on the gridding. Despite many years of Argo salinity profiles, the observational basis still remains small in many regions of the Atlantic. During the two decades 1980-2000, data coverage is concentrated on certain regions (offshore North America and in the Norwegian and North Seas) and resulted from historical ship-based measurements.

For the study in the tropical Pacific, profiles were extracted from the same European Argo repository for the Pacific ocean between 25 °S to 25 °N and the period 2005–2013. Some of these profiles have a high vertical resolution of 1 m, the majority provide data at 10 m vertical resolution. The profile data were used here to calculate density profiles and stability conditions

of the upper water column. Additional quality checks were concerned with assuring stably stratified density profiles, and excluding data exceeding 3 times the standard deviation of the world ocean atlas (WOA09, *Antonov et al.* (2010); *Locarnini et al.* (2010)) climatology.

For the validation study of the SMOS satellite derived salinity data I used an advanced global data set of *Ingleby and Huddleston* (2007), who made a collection of in situ data available, which is called EN4 in the following (*Good et al.*, 2013). In this validation study, data were used from January 2010 to December 2014, encompassing the operation period of the SMOS satellite. Also used in this validation study is the objectively analyzed EN4 salinity data set (*Good et al.*, 2013) (called EN4OBJ henceforth), comprising mostly Argo data, but also other in situ data. These data have a monthly resolution and are provided as optimum interpolations on a 1 ° spatial grid. The covariance length scales used during the optimal interpolation are of 300 and 400 km in zonal and meridional direction, respectively. The EN4OBJ salinity distribution shows more detailed structures than earlier versions of objectively analyzed salinity fields from IPRC (url: http://apdrc.soest.hawaii.edu/projects/argo/) or the ISAS fields (http://wwz.ifremer.fr/lpo/SO-Argo/Products/Global-Ocean-T-S).

2.2.1. Mooring data

Mooring time series of SSS were used to estimate the amplitude of the annual cycle and temporal scales of variability in the Atlantic Ocean. The uppermost salinity records from several moorings (in the range 0–35 m) were extracted, notably from the PIRATA moorings in the equatorial Atlantic region; from the ESTOC time series located at 29 °N, 15.9 °W; from the BATS station near 31 °N, 64 °W; from the PAP mooring at 49 °N, 16.5 °W; from the CIS mooring located at 60 ° N, 40 °W; and finally from station M located at 66 °N, 2 °E. All data were retrieved from publicly available databases (http://bats.bios.edu/bats_form_bottle.html, http://www.eurosites.info/data.php and http://www.brest.ird.fr/pirata).

2.2.2. Thermosalinograph data

The global thermosalinograph (TSG) data are merged into the gridded data set for the Atlantic being averaged before to a daily 0.5 °resolution in order not to weight the daily grid values. While preserving the original variability, all derived statistics are consequently not weighted to the numerous data available on one particular day. However, for the calculation of spatial decorrelation scales as well as for independent data validation of the drifter data (section 2.2.3) as well as for validation of the SMOS data (section 2.1.3), I used the numerous single thermosalinograph sections from the French data collection first under the Gosud program (found at *http://www.gosud.org/Data-access/Gosud-FTP-Access*) and later made available by the French Sea Surface Salinity Observation Service (http://www.legos.obs-mip.fr/observations/sss).

Those in situ observations used for the calculation of the spatial decorrelation scales in the Atlantic were obtained by voluntary observing ships (VOS) along 89 transects completed during 2000–2013, crossing the Atlantic quasi zonally at about 60 °N (75 sections) and 45 °N (14 sections). Additional TSG data which comprise 14 quasi-meridional sections performed by the German RV "Polarstern", crossing the Atlantic Ocean from the Nordic Seas, at 78 °N, to the Drake Passage, were retrieved from http://www.pangaea.de and incorporated in the study.

The latter TSG records are not included in the Atlantic in situ salinity data set compiled above and were selected according to two criteria: (1) ship speed had to be at least 3 m s^{-1} (i.e. all ship stops were removed); (2) for each subsection considered, all data deviating from the mean more than 2.5 standard deviations were discarded. Data were then separated into smaller sections resulting from interruptions of transects lasting longer than 5 hours. Within resulting segments, salinity data were interpolated spatially onto an equidistant 2 km grid and detrended over 1500-km long sections (where possible; otherwise smaller but only up to a minimum length of 500 km). The data availability and the locations of the sections will be described in the chapters.

2.2.3. Salinity data from surface drifter

The drifter type used in the present study is the widely used surface drifter manufactured in our case by Pacific Gyre^{TM} which was designed for tracking the ocean surface currents in the Surface Velocity Program (SVP). The drifters were equipped with a salinity measurement device. This measurement device has so far been used on a project basis (*Reverdin et al.*, 2014; *Hormann et al.*, 2015), for global use the quality and usefulness of the salinity data for the validation of space born salinity has to be proven. The present study contributes to this proof.

The surface drifter consists of a spherical float of about 38 cm diameter (Fig. 2.4), which contains the telemetry device. Below the float, a device is mounted carrying the measuring instruments. A drogue having a diameter of 91 cm and a length of 10 m is attached by a steel cable of about 10 m length. The Seabird conductivity cell (Modell SBE37) is installed at a centered depth of 38 cm below the assumed water line, the second thermistor at about 45 cm depth, having a distance of 7 cm between each other. At about 15 cm below the water surface, a supplementary thermistor measures temperature with an accuracy of 0.05 °C. Seven drifters of an older type launched in the Greenland Sea were equipped with only one thermistor at 45 cm having an accuracy of 0.1 °C.

Two sets of drifters were launched in the frame of the German SMOS Calibration and Validation (CalVal) project by ships of opportunity in one of the warmest world's ocean region, in the tropical Pacific, and one of the coldest region, the Greenland Sea, with the aim to get validation samples for the satellite derived salinity at the ocean's surface in the extreme temperature ranges. The exact launch position and dates can be found in Table A.1.1 in the appendix. Here, a summary is given.

Ten drifters were launched in March 2010, along 14 °S in the western tropical Pacific, within 2 clusters, one at 164 °W, the other at 160 °W. Other fourteen drifters were launched in June 2010 in the North Atlantic Ocean, the Greenland Sea, along 75 °N in clusters of three to four drifters at 6 °W and 2 °W, 1 °W and at 1 °E. A last drifter was launched later in September 2010 at 78 °36.65' N 2 °24.74' E. For launching the drifters, opportunities were taken from several RVs passing at or even deviating their cruise tracks to the planned positions.

The drifters kept their drogue 346 days on average, all drifters have transmitted during 545 days on average. Four drifters launched in the Greenland Sea failed or transmitted only once (3), or died after some days (1) in the cold sea. Drifter 83299 was launched later and very near to sea ice, perhaps there has been a collision with some ice, therefore only 9 days of

reasonable data are available. Details about lifetime and fate of the drifters, loss of the drogue and availability of the salinity and temperature data are given in Table A.1.1 in the appendix.

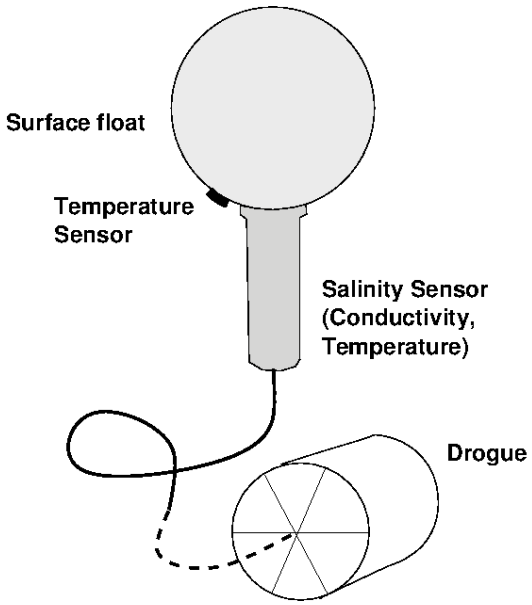

Figure 2.4.: Schematics of a surface drifter manufactured by Pacific Gyre ^{TM} in the ordered configuration.

The drifters measured temperature and conductivity every minute during a 5 minute interval before transferring averaged values of temperature and salinity of the 5 minute periods at intervals of half an hour. Data from the drifters were transmitted via satellite by the ARGOS system. The data were transmitted whenever the constellation of the ARGOS satellites is adequate, only data with a quality index "Location Class" 3 or 4 were used. They include header information (Time, latitude and longitude, submergence, battery voltage and quality index) and additionally temperature and salinity data each 30 minutes during the preceding 3.5 hours for the newer types, and the preceding 5.5 hours for the older ones, respectively. The shorter measurement period is due to the second temperature sensor, increasing the number of data to be transmitted. The 'age' of the most recent measurement was transmitted too, and allows reconstructing the time of measurement of the preceding hours. The 'checksum' was considered to discard data with bad transmissions. Good transmissions occur each 50 minutes on average, containing data series of 4 (for the newer drifter types) or 6 hours (for the older types), so time coverage is multiple on an irregular basis.

The constellation adequate for data transmission lasts for about one minute and data are transmitted repeatedly each 10 seconds. In more detail, the streams of temperature or salinity data only transmit one absolute value, the other data are relative in respect to the last one, i.e. if the only absolute datum is erroneous, the whole data stream had to be erased. In case of ambiguous salinity or temperature data, the whole message has been erased. Moreover, the salinity in a message in some cases showed a shift of its value comparing to the preceding

and following message. An empirical criterion was chosen to select out bad data, by allowing single changes to be less than 0.1 within a 20 minute interval in either positive or negative direction. If this error is due to the erroneous transmission of the whole message in spite of a 'good' checksum or due to the erroneous measurement is not clear, however, it is considered unrealistic and was erased.

A data set was produced at an half hourly resolution, and the processing is done by applying the following steps:

- Data were discarded if they were out of the range $25 < S < 40$.
- The standard deviation (std) during the 4 or 6 hours of measurements was calculated and values exceeding 2 times the std were discarded, if the std > 0.01.
- All the salinity and temperature data were superposed and sorted according to their time of measurement, however latitude and longitude as well as submergence and quality index is available only at the time of transmission.
- A filter was set which discarded data exceeding 3 times the std over the whole trajectory from the median value.
- A more detailed filter despiked the data on a monthly basis afterwards, hereby allowing 2 times std(S) in the positive direction, and 3 times the std(S) in the negative direction because of eventual rain events.
- Then, data were interpolated onto 1 hour intervals, applying a rectangle median average of the data occurring within the 3 hours interval. Though a thoroughful despiking was done before, there were still data showing a salinity offset of 0.1 to 1 to neighbouring values. So another filter was set up: if the mean value and the most frequent value within a 5 hour interval differed by more than 0.05 (which is an empirical value), salinity data exceeding the median value in that interval by 2 times std(S within 5 hours) were discarded and a new median value within the 3 hours was computed.
- A last filter was applied to detect erroneous data in the hourly data: within a moving 17 point rectangular window a difference of the middle value to the median salinity was allowed to be 1.5 times the std(S within 17 h). For deviations higher than this critical value, the salinity was forced to a median average of the 17 point window. This subjective criterion erased spikes additionally.
- Conductivity was measured at about 8 cm distance to the temperature sensor. So in cases of temperature gradients, the salinity was calculated from not aligned values. These conditions prevail during days of very nice weather, i.e. strong diurnal heating with weak wind (< 2 m/s). Then salinity spikes could occur in both directions, because the temperature gradient might be waved around the conductivity cell. In order to detect these cases automatically in the drifter data with only one temperature sensor, the temperature time series was low pass filtered (cutoff frequency = 2.25 days) and subtracted from the original one. Absolute differences between the filtered and the original time series of more than 0.25 °C were excluded. For the drifter data containing two temperature measurements the temperature gradients (dT) were calculated. On days with strong diurnal heating the dT was often > 1 °C. The salinity data showing spikes on these days were excluded.
- Finally, a Hamming filter was applied over 30 hours with a cutoff frequency of 1/8 h, in this

last step salinity was interpolated, but accuracy cannot be better than 0.01. Interpolated and filtered data of salinity was stored.

The percentage of data excluded is different for each drifter. High fractions of salinity spikes occur indirectly due to the loss of the drogue, especially drifters no. 92793 and 92795 show very noisy temperature records and therefore also salinity is useless. Why the other drifters' salinity records are not affected by the loss of drogue in the same manner is not clear. A higher number of outliers is presumed to occur in the case of loss of the drogue because the drogue has a stabilizing effect in strong waves. Even without bubbles in the conductivity cell, it may be flushed with high velocity not corresponding to the prescribed alignment of temperature and conductivity and thus salinity is erroneous.

In general, there is no clear leaning of the spikes to either side of the mean monthly values, showing a general good alignment of conductivity and temperature. Drifters entering the fresher surface water (Drifters 82042, 82043 and 92785, not shown) tend to have more negative spikes. Drifters subject to bad weather and probable bubbles in the conductivity cells (i.e. lower conductivity measured in the cell) or subject to some biological material stuck or grown in the cell presumably show negative salinity spikes. Though these disturbances are likely to occur in the Greenland Sea or in the Pacific subtropical waters, it cannot be shown that dominantly negative spikes occur in the range of the monthly standard deviations. *Hormann et al.* (2015) showed a dominance of negative salinity spikes which, in the author's opinion, occurs due to the averaging of salinity prior to data transmission. In general, salinity outliers are negative, because the processes perturbing the conductivity measurement mentioned before result in fresher salinity values. However, there are cases of strong daily heating giving rise to positive salinity anomalies due to the vertical temperature gradient and consequent misalignment of temperature and conductivity.

Validation of drifter salinity

For validation of the drifters' salinity, there are a few Argo profilers providing independent salinity data, with measurements at 5 to 10 dbar depth, and several TSG measurements from VOS. The drifters' salinities are compared to these data sets by selecting pairs of data within a distance of $\pm$ 50 km and a time period of $\pm$ 2 days. If there are more than one datum of salinity within the considered period, the average and the standard deviation (std) within the period of coincidence are calculated.

Figures 2.5 show the comparisons between the salinity from drifters and Argo profile measurements and between the drifter salinity and underway ship data with error bars indicating the std during the collocation period. The comparison reveals neither significant bias nor temporal drift (not shown) within the drifters' measurements. The RMS difference amounts to 0.15 between the drifter and Argo salinity and to a similar value of 0.13 between drifter and TSG salinity data. The standard deviation (std) within the period of 10 days given by the bars in the Figure 2.5 shows, that the sampling error of the single measurements may explain the high RMS difference. On the other hand, there are not many in situ measurements for validating the drifters' salinity, 134 data pairs in case of Argo data and 41 pairs in case of TSG measurements. Local spatial distance (marked in Fig. 2.5, left panel) and temporal mismatch

may cause uncertainties in the differences. However, a dependence on the distance between the measurement from drifter to shipboard TSG or Argo instruments was not conclusive and within the RMS difference.

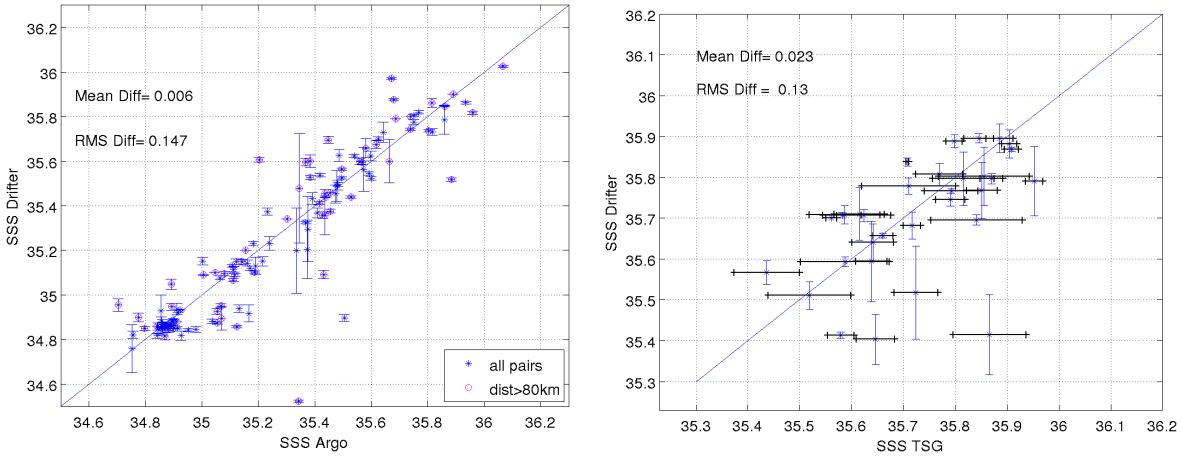

Figure 2.5.: Comparison of collocated salinity values from Argo profilers (left) and TSG (right) nearby the surface drifters within a distance of up to 100 km and a time window of 10 days (left). Collocations with a distance of > 80 km are marked pink in the left panel. The standard deviation of drifter and TSG salinity during the corresponding time and region is indicated by bars in the right panel. The mean difference between all pairs and the root mean square (RMS) difference is given in the upper left.

The results presented here are part of a study by *Reverdin et al.* (2014) who showed occasional salinity shiftings in the time series of the drifters' data, thereby, the present validation results are included in the latter publication. The authors used Argo measurements nearby to correct the shifted salinity chunks. In the present time series, shifts in salinity by 0.1 or 0.2 are present, too. I checked the time series of salinity by calculating the differences between the low-passed salinity (cutoff frequency 1/35 h) to the original time series and inspected all abrupt changes in salinity exceeding 0.1. Some shifts and spikes were identified and could be correlated to rain events. The rain data was a combination of daily rain data from several satellite missions, the Special Sensor Microwave Imager (SSM/I), the Tropical Rainfall Measuring Mission (TRMM) with the TRMM Microwave Imager (TMI) and the Advanced Microwave Scanning Radiometer (AMSR). From the gridded data with a spatial resolution of 0.25 ° the surrounding grid boxes of the drifters' position were selected in order to account for the daily estimated drift of the instrument of about 25 km/day. Some coincidences were found between a salinity drop and precipitation. However, the most cases of salinity drops or shifts could not be correlated to any rain event recorded in the precipitation data. A lot of rain events had no subsequent salinity drops, either. I haven't found any correlation between salinity drop-offs with rain events. An example with salinity and rain is given in Fig. 2.6. However, based on the studies of *Reverdin et al.* (2014) I cannot rule out that the drifters' salinity is erroneous

during some periods of time.

The final salinity data set of the surface drifters is publicly available at *http://icdc.zmaw.de/daten/ocean*). The data include an error estimate and flags indicating possible errors or corrected temperature values.

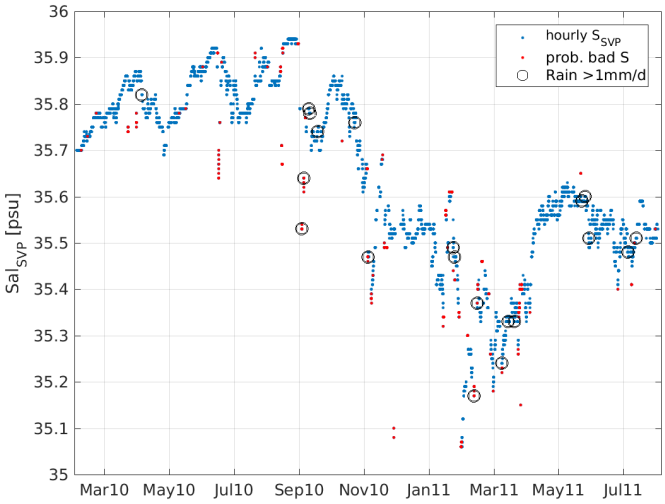

Figure 2.6.: Salinity time series from the surface drifters no 92789 (blue) with probably bad values (red) and rain events with precipitation of > 1 mm/day marked as black circles.

2.3. Salinity from a numerical simulation

The temporal and spatial variability of SSS was also analyzed using the output from a numerical eddy-resolving simulation integrated over the period 2002-2011 obtained using the MIT ocean general circulation model (*Marshall et al.*, 1997). The model was configured with a spatial resolution of about 4 km (equivalent to $1/24\,^\circ$ at the equator) for the Atlantic Ocean north of 33 °S and included the Mediterranean Sea, the Nordic Seas and the Arctic Ocean, as described in *Serra et al.* (2010). The vertical resolution varies from 5 m in the upper ocean to 275 m in the deep ocean (100 vertical levels). The model bottom topography was extracted from ETOPO2 (*Smith and Sandwell*, 1997) and the initial temperature and salinity conditions were retrieved from a 8-km resolution integration of the same model for the period 1948-2003 (to achieve a good degree of spin-up), which in turn started from rest initialized by the World Ocean Climatology 2005 (*Boyer et al.*, 2005, WOA05).

At the surface, the model was forced by fluxes of momentum, heat and freshwater computed using bulk formula and the 6-hourly atmospheric state from the ECMWF/ERA-interim reanalysis (*Dee et al.*, 2011). At the volume-balanced open northern and southern boundaries, the model is forced by a $1\,^\circ$ resolution global solution of the MITgcm. Vertical mixing is pa-

rameterized by the KPP formulation. The used background coefficients of vertical viscosity and diffusivity were 1×10^{-4} m^2 s^{-1} and 1×10^{-5} m^2 s^{-1}, respectively. The coefficient of horizontal biharmonic viscosity was set to 3×10^9 m^4 s^{-1}. The model includes a dynamic-thermodynamic sea ice model, realistically simulating the impact of respective surface freshwater fluxes in the Arctic Ocean and along the coasts of Greenland (*Köhl et al.*, 2014). An annual averaged river run-off derived from *Fekete et al.* (1999) is imposed in the model by adding a corresponding freshwater flux to the Precipitation-minus- Evaporation field at grid points adjacent to river mouths. The model dynamics are then responsible for distributing this low salinity signal into the ocean interior.

The model sea surface salinity was relaxed to the Polar Science Center Hydrographic Climatology 3.0 (*Steele, Michael et al.*, 2001), which corresponds to the monthly WOA05 climatology further improved in the Arctic region. The surface relaxation of SSS towards the monthly climatology is unfortunately unavoidable since it prevents large spurious trends in the multi-annual integration. Without such a relaxation term, salinity biases would accumulate during the course of the integration mainly due to errors in surface freshwater flux (precipitation minus evaporation, P-E), and partly due to unrealistic river runoff. The impact of the model SSS damping on the SSS variability scales computed in the present work will be discussed in section 2.4. The study uses daily averages of simulated SSS for the 7-year period 2003–2009.

2.4. Other data used

Surface velocity

Surface velocity data were needed in chapter 5 to compute the lateral freshwater transports. Monthly mean zonal and meridional near surface velocity components, u and v, available from the OSCAR project (see www.oscar.noaa.gov), were used after interpolating the velocity files to a 1° geographic grid. Alternatively, freshwater transports were computed using the monthly climatological velocity data which were derived from surface drifters by *Lumpkin and Johnson* (2013).

Atmospheric fluxes

To estimate the atmospheric freshwater fluxes, $E - P$ monthly accumulated evaporation fields were computed. Evaporation data were obtained from the OAFlux project, ftp://ftp.whoi.edu/pub/science/oaflux/data). For precipitation the Version 2.2 Satellite and Gauge combined Precipitation Data Set was used from the Global Precipitation Climatology Project (GPCP) obtained under ftp://precip.gsfc.nasa.gov/pub/gpcp-v2.2/psg/.

3. Spatial and temporal scales of sea surface salinity variability in the Atlantic Ocean

3.1. Introduction

The hydrological cycle in the Atlantic Ocean plays a major role in changing the near-surface salinity and, in particular, the density of the upper subpolar North Atlantic. Understanding this role is of general interest, since it has a strong impact on the formation of deep water masses and thus on the meridional overturning circulation of the Atlantic. In the past, a quantitative investigation of processes involved in ocean salinity changes was hampered by the lack of salinity observations suitable to quantify salinity variability on relevant space and time scales. With the availability of Argo float temperature and salinity profiles, but also through the advent of satellite missions measuring sea surface salinity (SSS), today, the community is able to investigate salinity changes and their role in the climate system. In this context, it is noticed that there is a difference between satellite derived SSS and in situ measurements of salinity since the latter measurements usually originate from a depth of one to several meters. In this study, for simplicity, I use the abbreviation SSS to refer to the uppermost salinity from in situ data or from model simulations.

Previous studies aimed at quantifying the Atlantic SSS variability from an analysis of various types of measurements obtained during the earlier decade. Among those, *Bingham et al.* (2012) estimated the annual amplitude of the variability of the mixed layer salinity and investigated underlying causes in the global ocean by applying an annual harmonic fit and relating it to the surface forcing by evaporation and precipitation. *Delcroix et al.* (2005) used thermosalinograph data collected by voluntary observing ships along various sections to investigate space and time decorrelation scales (the scale over which the time series loses significant correlation with itself) of near-surface salinity in the tropical and subtropical band of the global ocean. The authors reported salinity decorrelation scales of $2\,^\circ$ to $4.5\,^\circ$ and 2 to 3 months for the Atlantic, depending on season and geographical region. Larger ($3.8\,^\circ$ to $4.2\,^\circ$) and longer ($>$ 6 months) scales were found in the southwestern Pacific due to the influence of El Niño. On the other hand, shorter scales of 2.3 and 5.0 days were found by the same authors when calculating decorrelation scales by splitting the long term measurements from moorings into periods of 10 and 30 days, respectively.

The goal of the present chapter is to expand the analysis by *Delcroix et al.* (2005) of SSS variability and associated space and time scales by providing a substantially more detailed description of SSS variability in the Atlantic Ocean than was possible before, now using all available near-surface salinity observations from the period 1980–2013 jointly with the output from an eddy-resolving (4 km) model simulation of the Atlantic Ocean circulation. In addition to the WOCE dataset, the updated observational database includes: salinity data recorded at

various Atlantic mooring stations and from underway ship measurements (thermosalinograph data) and, especially, Argo float data. The results derived from these observations in terms of salinity variability are compared with, and expanded by, those found in the numerical simulation, the latter providing unprecedented geographic details of non-seasonal eddy-related salinity variability, which can be used to extend observational-based estimates into regions usually not covered by available SSS measurements (notably the ocean boundaries and shelf regions, as well as parts repeatedly or always covered by sea ice). An analysis of model SSS variability in terms of forcing factors like surface freshwater fluxes and oceanic lateral and vertical fluxes (like e.g. the work performed by *Yu*, 2011; *Vinogradova and Ponte*, 2013a) is out of the scope of the present subject. Instead, the main aim here is to present and discuss the scales of SSS variability. It is anticipated that results will be helpful for processing and understanding satellite SSS retrievals as well as for SSS assimilation studies.

3.2. Atlantic SSS variability from in situ measurements and model

The aim of the current section is twofold: (1) to present the total SSS variability and the amplitude/phase of the SSS annual cycle emerging from the observational data set, discussing possible sampling errors, and (2) to show how the model variability is in good agreement to that estimated from observations, thus building confidence in further analyzing the model results in the following concerning the scales of SSS variability, a computation difficult to perform from in situ measurements due to the poor spatial and temporal data coverage.

3.2.1. Total SSS variability

The time-average SSS from observations and from the model compare well and are also consistent with the WOA2009 climatological distribution (*Antonov et al.*, 2010) (not shown). The SSS total standard deviation (std), estimated from the detrended observations, is shown in the left panel of Fig. 3.1. In the figure, an overall background level of observed SSS variability appears to be on the order of 0.2, but in the region of the eastern North Atlantic (in particular in the areas west of the United Kingdom and southwest of Iceland) and in the Norwegian Sea, the SSS variability is below 0.1. North of 25 °N, regions of large variability (> 0.7) occur along the pathways of the East and West Greenland Currents, the Labrador Current, the Norwegian Coastal Current and north of the Gulf Stream Axis. South from 25 °N, the large variability regions are concentrated at the discharge regions of the Amazon and Plata Rivers in the west, the former extending northwest of the Lesser Antilles and into the Caribbean Sea, and the Congo River in the east.

The model reproduces the spatial patterns of the observed std (Fig. 3.1, right), but with lower variability along the paths of the North and South Equatorial Currents and smaller values of std in the high variability regions seen in the observations. The overall higher variability in the observations in comparison to the model is due to the computation of the std in a grid box whereas the model allows to calculate the variability from a time series at one point. However, the model results present much more spatial detailed features of the variability than can be inferred from the insufficient observations (like for instance the very localized aspect of the

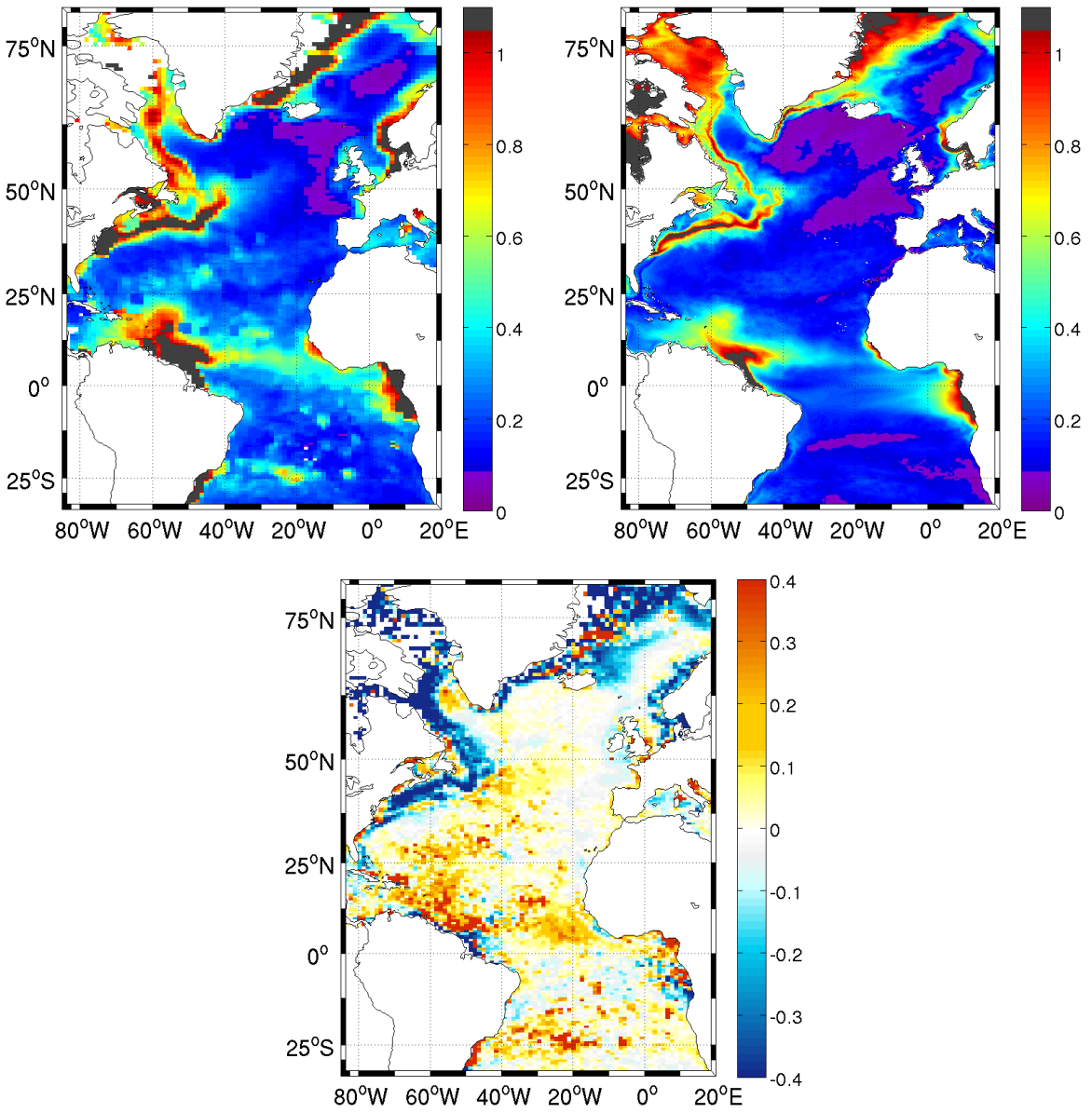

Figure 3.1.: Standard deviation (upper row) of detrended SSS from in situ measurements (in the grid boxes detailed in the text, left panel) and from the 4 km resolution simulation (at each model grid point, right). Lower panel: Over-/under- estimation of the SSS variability in the grid boxes due to the observational sampling.

variability in the Labrador Current and off Greenland in the Irminger Sea) and extends the variability estimate to regions seasonally covered with sea ice.

Moreover, the observational estimate of the SSS variability suffers from sampling errors, i.e., both temporally and spatially, the measurements are not enough to resolve the variability. In order to quantitatively estimate how much of the std in Fig. 3.1 can potentially come from sampling errors, the model SSS monthly climatology (derived from the 7 years of daily output) was resampled for each month at the positions where measurements took place during that month. After gridding those resampled results and the total monthly climatology with the same methodology described in Section 2, the difference between resampled and total climatologies was computed (Fig. 3.1, lower panel). According to the figure, the distribution of measurements leads to an underestimation of the SSS variability (negative values) notably in the Amazon River plume, north of the Gulf Stream axis, in the Labrador Sea, off the eastern Greenland coast and at the exit of the Baltic Sea. These are regions where indeed the observational std is underestimated due to the insufficient sampling.

In other regions, namely along the Gulf Stream axis, in the West Greenland Current and the Labrador current, and off the Norwegian coast, the observational sampling promotes a potential variability overestimation. Indeed these regions show larger variability in the observational std than the model. The open ocean, on the other hand, shows low uncertainties in the estimation of the std, so in general the std from observations is only little overestimated in the interior. I therefore conclude that the observational estimate is regionally biased and that the model solution has substantial added value, even despite some unresolved subgrid-scale processes being absent in the simulation.

3.2.2. Annual component of the SSS variability

In order to investigate how much of the variability shown in Figs. 3.1 is annual, a sinusoidal annual cycle was least-squares fitted to the observational data set, a method also used by *Bingham et al.* (2012) on a coarser grid (2.5 ° latitude and longitude) and on a global scale. In the present analysis I discarded grid boxes with less than 50 observations. Due to the overlapping boxes and most recent data originating from December 2013, more details of the variability and of the annual amplitude can be shown than in previous studies. The correlation (and its significance) between the fit and the available data was computed and where the significance was lower than 95%, results were discarded. As before, also here the annual amplitude may be biased in part due to the uneven spatial sampling within a grid box.

The distribution of the SSS annual amplitude and phase (Fig. 3.2) is interesting in its own right, as the observations show a lot of new details. Most of previous studies were confined to regional analysis or to older data sets, and do not present such a comprehensive and detailed overview for the entire Atlantic basin. These results in the tropical and subtropical regions correspond in overall terms well to *Boyer and Levitus* (2002), the analysis of *Dessier and Donguy* (1994) between 10 °S and 30 °N, to the results on sections in *Delcroix et al.* (2005) and also to the results found by *Bingham et al.* (2012). In the latter study, however, the color scale was saturated at 0.5, and their study region was confined to 60 °N.

In terms of amplitude (Fig. 3.2), two areas with an annual cycle larger than 1.2 can be

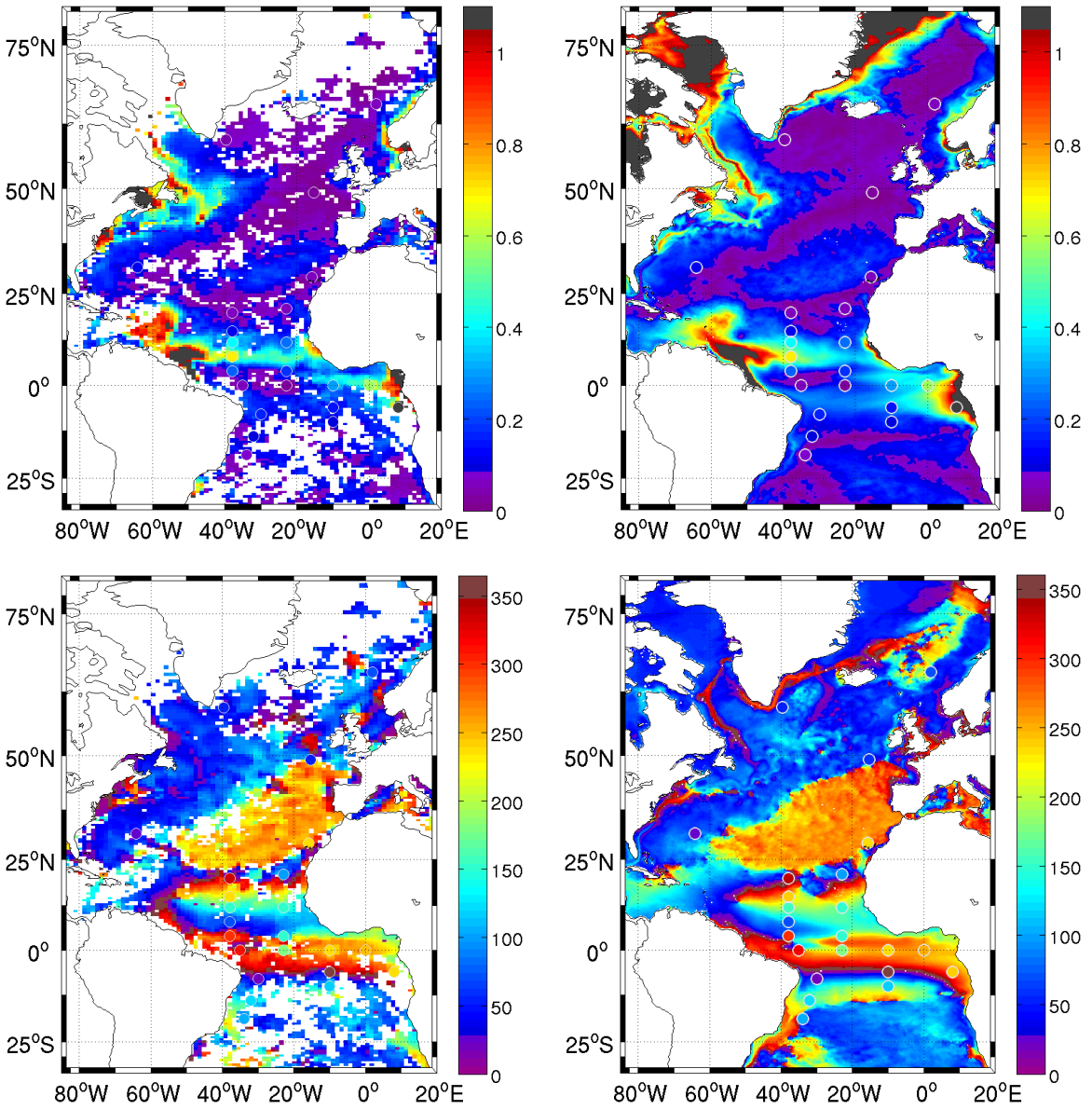

Figure 3.2.: Amplitude (upper row) and phase (day of maximum, lower row) of the detrended SSS annual cycle from (left) in situ data and (right) 4 km resolution model. The amplitude and phase of the annual cycle of the uppermost salinity from the mooring data (PIRATA, BATS and EUROSites stations) are overlaid (colored dots) at their respective positions. White gaps correspond to boxes where the annual fit to the SSS is not significant.

found: (1) the Amazon River plume and the retroflection region into the North Equatorial Countercurrent, and (2) the eastern tropical Atlantic due to river discharge and due to coastal as well as equatorial upwelling (here *Dessier and Donguy* (1994) also found amplitudes of 1.8). The annual signal produced in the interior of the Labrador Sea is small (up to 0.2) but it reaches high values along its rim (up to 0.9). *Schmidt and Send* (2007) found an annual salinity variability of up to 1 within the Labrador Sea boundary currents and a similar annual variability (0.2) in the central Labrador Sea at the Bravo station. From freshwater budget estimations they deduced, that the boundary currents contribute significantly to the variability within the central Labrador Sea, either by advection or by intruding eddies shed from the West Greenland Current and possibly also from the Labrador Current, with local effects as sea ice melting having less importance.

The annual component of the SSS variability along the Gulf Stream and North Atlantic Current amounts only to about 0.2, i.e. the large SSS variability there is dominated by time scales outside the annual frequency band. The annual amplitude in the subtropics was found to be insignificant in the study of *Bingham et al.* (2012). Also in the present study the amplitude is low, but with more data coverage is found here to be significant. In my results, the South Atlantic shows low annual variability, whereas *Boyer and Levitus* (2002) (based on monthly objectively interpolated fields) and *Bingham et al.* (2012) claim an annual amplitude of up to 0.3 along about 6 °S. The reasons for this discrepancy is unknown; on the other hand the study of *Bingham et al.* (2012) is about the surface mixed layer and not only about the uppermost or near surface salinity as in the present study.

As the model annual cycle compares well with the observational field, the model results can be used further to extend the observational results into unobserved areas. High annual amplitudes were found in the model along the edge of the seasonally varying sea ice advected by the East and West Greenland Currents, a feature not well sampled in the observations and therefore with not enough significance in the annual fit estimate.

In the South Atlantic south of 10 °S, the observations are also not sufficient to produce significant results; here the model helps in completing the picture. Throughout the South Atlantic, the annual cycle has low amplitudes and the only region with an amplitude exceeding 0.2 is off the South American coast near 25 °S. This is a region of relatively small observational data coverage but also strong freshwater forcing (note that in the present model simulation a realistic forcing from La Plata River is missing since it resides out of the domain).

The observed annual phases, corresponding to the year day of the SSS annual cycle maximum, are presented in Figs. 3.2c. In general terms, SSS reaches a maximum in late winter in the western North Atlantic and over the subpolar gyre. The freshwater related to sea ice melting in summer/fall is responsible for the minimum salinities at northern latitudes during those seasons. The results correspond favorably to the study of *Boyer and Levitus* (2002) and *Bingham et al.* (2012) but show a much more detailed result.

Over the central and eastern parts of the subtropical gyre, strong evaporation leads to a maximum SSS during boreal summer. The phase change of the SSS annual cycle in the latitudinal band 13 °N to 25 °N is explained both by an annually varying northward progression of the maximum evaporation area (leading to a northward moving maximum SSS) and the northward advection of low salinity water by the North Equatorial Countercurrent. The phase

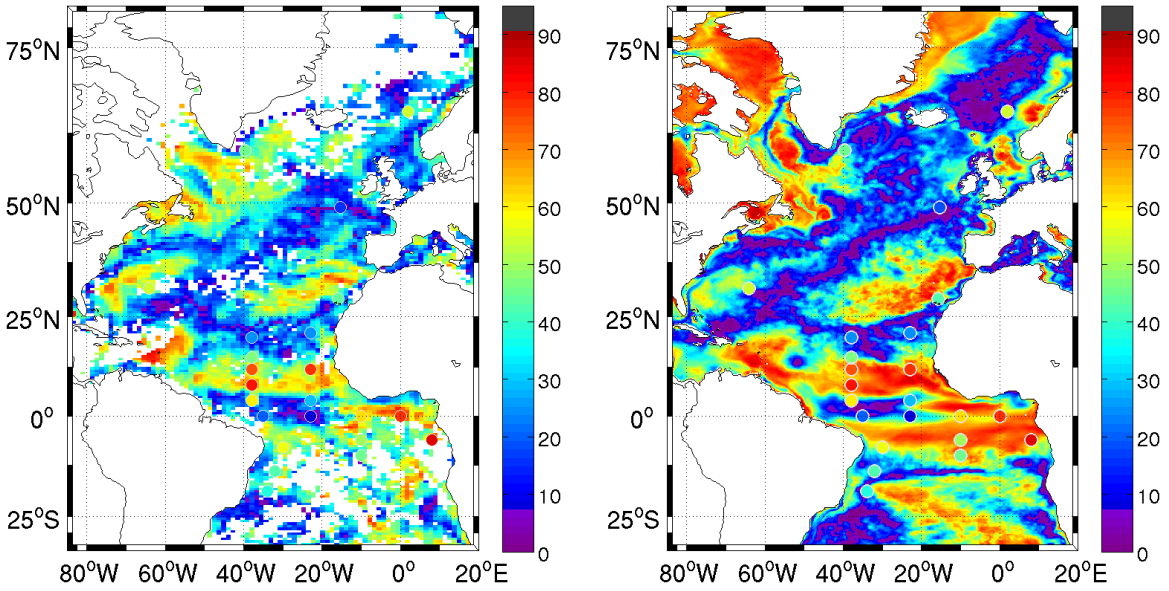

Figure 3.3.: Percentage of the total SSS variance explained by the SSS annual cycle from (left) in situ data and (right) the 4 km resolution model. Colored dots present the estimated variance fraction based on mooring data.

of the SSS annual cycle in the western tropical Atlantic is influenced by the timing of the Amazon River runoff and the advection of its low salinity by the North Brazil Current rings (to the north and into the Caribbean Sea) and the North Equatorial Countercurrent. Indeed, despite the amplitude of the annual SSS variability being controlled by the magnitude of the Amazon outflow, the phase of the SSS in the region depends mainly on the ocean dynamics and not on the river output strength (*Masson and Delecluse*, 2001). The low salinity signal of the Amazon River peaks in spring but the tropical region is affected mostly after the development of the North Brazil Current retroflection in summer.

In the equatorial Atlantic, the appearance of a low-salinity tongue in late winter/spring relaxing towards boreal summer marks the SSS annual cycle there. The maximum SSS takes place in boreal winter and the annual cycle is marked by a small zonal shift of the SSS maximum. The annual cycle at the equator west of 15 °W is very low and there the semi-annual and higher frequency components are strong (*Richardson and Walsh*, 1986; *Lumpkin and Garzoli*, 2005).

To corroborate the results with better temporal data coverage, and as an independent test of the observational results, I used the salinity data from several moorings providing observations after year 2000. The colored dots included in Figs. 3.2 and 3.3 present the estimates of SSS annual amplitude/phase results. The mooring results corroborate the other observational estimates, except for one PIRATA location in the equatorial region of the North Atlantic.

The model presents similar spatial patterns of SSS annual phases as the measurements. Although the SSS in the model is damped towards a monthly climatology, the latter does not present realistic patterns of total variability and of amplitude/phase of the SSS annual

cycle, specially in localized regions like the Labrador Sea and Gulf Stream. Therefore, the model provides valuable additional information about SSS annual variability in areas of poor observational sampling.

The fraction of the total variance explained by the annual cycle, taken as the ratio between the std of the annually-fitted SSS to the total std, is shown in Fig. 3.3. The annual component of SSS is large (fraction of variance larger than 60%) in the tropical region between 10 °N and 20 °N, off the Lesser Antilles, in the eastern equatorial Atlantic, in the subtropical eastern North and South Atlantic, south of the Gulf Stream, over the Grand Banks and in the central Labrador Sea (Fig. 3.3).

In the tropical region this is associated with both the seasonally varying Inter-Tropical Convergence Zone (ITCZ), where precipitation largely exceeds evaporation, and the seasonal behavior of the North Equatorial Countercurrent (e.g. *Dessier and Donguy*, 1994). East of the Lesser Antilles it is related to the seasonally-changing fate of the North Brazil Current rings, transporting freshwater to that region. In the subtropical regions, the relative importance of the annual cycle reflects the annually changing position of the subtropical salinity maximum (also included in the Fig. 2c of *Dessier and Donguy*, 1994). *Qu et al.* (2011) explain the salinity maximum variability there being only partly due to the summer maximum of evaporation; ocean advection and entrainment also play major roles. Ocean advection, as a cause for the annual variability, was also found by *Vinogradova and Ponte* (2013a).

South of the Gulf Stream, at about 30 °–35 °N extending to about 55 °W, the large annual component is due to surface forcing, specifically evaporation, as noted by *Yu* (2011). For the region off the Grand Banks *Vinogradova and Ponte* (2013a) found variability on all scales caused by ocean processes. Finally, in the central Labrador Sea, seasonal deep-water formation occurs, which strongly impacts the salinity variability. The mooring results again point to similar explained variances by the annual component as the other observational sources.

Despite the SSS variability in the model, relatively speaking, having a larger annual component than the observations (as seen by the overall larger percentages and in Fig. 3.2), partially this being a result of the model SSS relaxation, the obtained spatial patterns of the annual cycle contribution are like those from observations. On the other hand, the smaller percentages of explained variance by the annual cycle in the observations is partly due to larger total std in that case deriving from the sampling issues discussed above.

The model brings, however, additional information around Greenland, in the Caribbean Sea and in the South Atlantic. Along the path of the low salinity water transported by the East and West Greenland Currents and the northern Labrador Current, the SSS variability does not surprisingly show a predominance of the annual component. There, the variability has dominant scales at sub annual and/or interannual timescales (*Brandt et al.*, 2004). This is also the case along the Gulf Stream and North Atlantic Current. In the South Atlantic, where the amplitude of the annual variability (between 7 °S and 18 °S) is low (Fig. 3.2), the model shows a large percentage of variability being annual. The off-equatorial region between 0 and 10 °S shows also a prominent band of high annual component, however the amplitude is small (< 0.2) there.

The SSS variance ratios presented by *Delcroix et al.* (2005) along several sections through the tropical and subtropical Atlantic correspond well in their distributions to these results,

however, that study was based on gridded monthly values, which underestimate the total std, thus present higher values.

3.3. Spatial and temporal scales of SSS variability

Space and time scales of SSS variability are here estimated from thermosalinograph and mooring data and compared with respective results from the daily model output. Furthermore, in the model case, the scales were calculated for the entire Atlantic, thereby giving a complete ocean-wide perspective of the SSS variability scales, which is not possible using the measurements. In all cases, the spatial/temporal scales were computed, respectively, as the spatial/temporal lags of the e-folding decrease of the SSS auto-correlation functions. Scales were computed for both the total detrended SSS fields and the non-seasonal detrended SSS field (i.e., with the annual cycle discussed in Section 3 removed from the time series at each grid point). The aim in this case is to assess the scale differences imposed by the SSS annual cycle.

3.3.1. Spatial scales

The observed spatial SSS scales were computed from the thermosalinograph data available from quasi-meridional RV "Polarstern" transects (Fig. 3.4) and from quasi-zonal voluntary observing ships sections along 45 °N and 60 °N. The resulting spatial scales are shown in the right panel of Fig. 3.4 together with zonal averages (in the longitudinal range of the RV "Polarstern" sections) of the zonal and meridional SSS decorrelation scales computed for the model in windows of 400 km running in the zonal and meridional directions. For the model the analysis was performed on the native model orthogonal grid, so that zonal and meridional directions do not exactly correspond to earth geographical coordinates north of 10 °N. Also shown as vertical bars for the RV "Polarstern" sections and as dashed lines for the zonal and meridional model sections are the standard deviations of the decorrelation scales.

The observed decorrelation scales decrease from maximum 230 km in the tropical Atlantic to about 100 km in the northern North Atlantic. The meridional decorrelation scales of about 100 km resulting from the thermosalinograph data are smaller than the decorrelation scales of 2 to 3 ° found by *Delcroix et al.* (2005), who based their calculation on data with a spatial resolution of 1 °. The model shows slightly larger values (see above for a possible explanation of the larger values) and a similar pattern of latitudinal variation. On average, the zonal scales tend to be larger than the meridional scales between 15 °S and 15 °N in the model; north of this latitude the meridional scales are larger than the zonal ones. However, the meridional scales along the RV "Polarstern" sections do not show the strong latitudinal dependence, as found in the decorrelation scales from (not strictly meridional) sections further west in the Atlantic by *Delcroix et al.* (2005). On the other hand, the standard deviations are quite high, and a larger number of meridional sections is probably needed for significant estimates. Decorrelation scales derived from zonal sections along 45 °N and 60 °N (green line and bars in Figure 3.4b) show a high standard deviation, partly due to longitudinal variations in spatial scales (see below). The zonal scales derived from the model are again slightly larger than the observed mean values of 110 km at 45 °N and 80 km at 60 °N.

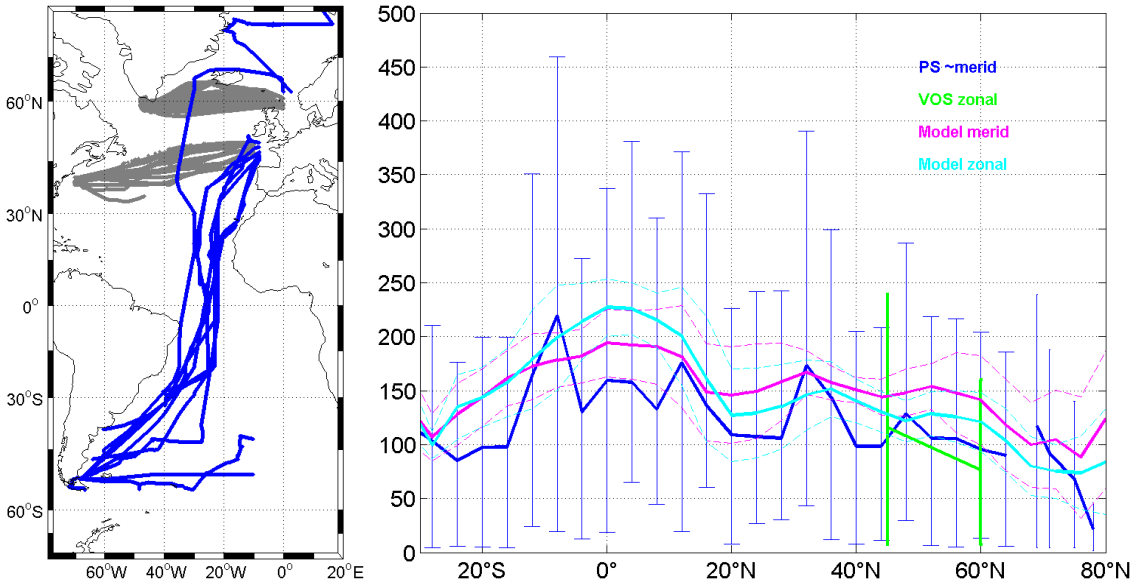

Figure 3.4.: Cruise tracks (left panel) of RV "Polarstern" (blue) and voluntary observing ships sections (gray) along which themosalinograph data were acquired. Latitudinal dependence of the along-track decorrelation scales (in km) from the cruise transects (dark blue and error bars, right panel). Superimposed in cyan (magenta) are the zonal (meridonal) model scales averaged in the longitudinal extent of the RV "Polarstern" cruises (solid lines) and their respective standard deviation (dashed lines). Mean spatial decorrelation scales from voluntary observing ships sections at 45 °N and 60 °N and their standard deviation bars are shown in green.

The model provides much more details and results suggest that outside the equatorial region an overall high degree of isotropy seems to prevail in the Atlantic SSS variability. Spatial SSS decorrelation scales larger than 200 km reside in tropical regions (Fig. 3.5) in zonal broad bands with maxima at about at 5 °N–10 °N and 5 °S–12 °S. In the northern hemisphere, spatial scales below 100 km are found along the Gulf Stream/North Atlantic Current and the North Equatorial Current, which are known for their large eddy activity. Further north, scales are also small in the interior of the Nordic Seas and along the East and West Greenland Currents. In the southern hemisphere, the South Equatorial Current features scales smaller than 150 km in a diagonal band from the southeast corner of the model domain to about 10 °W.

Spatial scales of SSS anomalies decrease dramatically when not including the annual cycle, in particular in extratropical regions (Fig. 3.5). Between 20 °S and 20 °N, zonal scales still achieve values as large as 200 km. Some seasonality may still persist in the residuals from the annual cycle, since these scales seem a bit large to be due to eddies or other small-scale processes. The semi-annual signal, for instance, was reported to be quite important in the tropical Atlantic (*Richardson and Walsh*, 1986; *Lumpkin and Garzoli*, 2005).

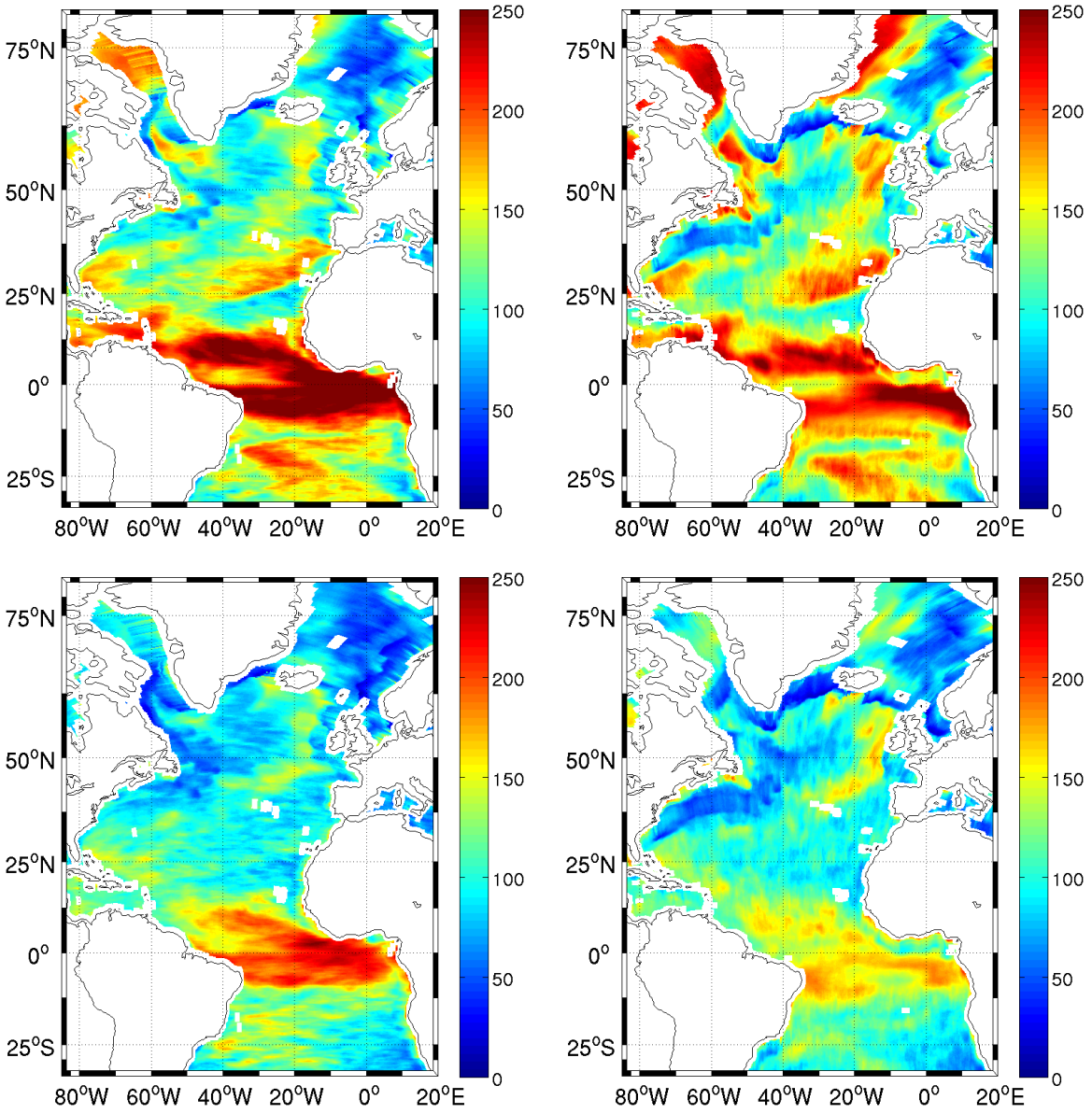

Figure 3.5.: Zonal (left panels) and meridional (right panels) decorrelation scales (in km) calculated from the 4 km resolution model detrended SSS (upper row), and from the model SSS anomaly data (2003–2009, lower row), i.e. with trend and annual cycle removed.

The vast majority of the North Atlantic is dominated by spatial scales smaller than 100 km at non-seasonal timescales, which are related to high-frequency fluctuations due to eddies and local fast atmospheric forcing. There are only few studies about spatial decorrelation scales; however, the scales found here for the Labrador Sea of <50 km are confirmed by *Frajka-Williams et al.* (2009). Interestingly, the anisotropy in fast current regions of the western North Atlantic

is now more obvious (scales approaching 50 km in the quasi meridional direction and about 100 km in the quasi zonal direction) than when including the annual cycle, revealing scales that are related to eddies and frontal processes. Assuming that the spatial scales of non-seasonal SSS variability are due to ocean circulation (currents and eddies) and not due to local surface forcing terms (evaporation, precipitation and river runoff) one can compare the obtained scales with eddy scales derived from altimetry data.

Some agreement is found with results reported by *Stammer* (1997), who determined eddy scales from TOPEX/POSEIDON altimetric records showing a decrease in eddy scales by about 50% from low to high latitudes. *Stammer* (1997) and later *Eden* (2007) related the decay of the spatial decorrelation scale to the first mode baroclinic Rossby radius of deformation north of about 30 °N and to the Rhines scale equatorward of this latitude. As noted in *Eden* (2007) the eddy scales south of 30 °N are anisotropic, with zonal fluctuations being larger than meridional ones. The model results here presented confirm the pattern of zonal spatial scales found by *Delcroix et al.* (2005), however, the present study shows smaller scales than reported before.

3.3.2. Temporal scales

Because of their sparse sampling in time, I cannot compute temporal scales from the merged Argo and CTD SSS database; however, the model daily output offers an excellent basis for their computation (Figs. 3.6). In regions where the model showed a large fraction of the SSS variability being of a mostly annual nature (Fig. 3.3), temporal scales of decorrelation are larger than 60 days. This is in accordance with *Delcroix et al.* (2005), who arrived to decorrelation scales of 2 to 3 months within the tropical band up to 30 ° latitude.

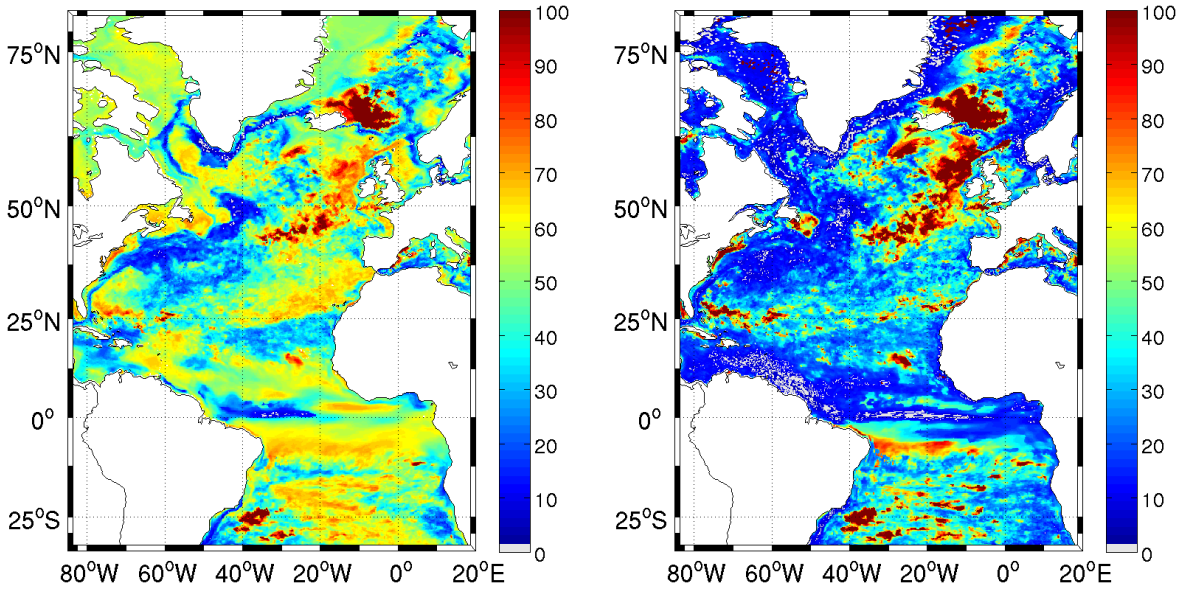

Figure 3.6.: Temporal decorrelation scales (in days) calculated from the 4 km resolution model detrended SSS (2003-2009, left panel), and calculated from same model SSS anomaly data (2003-2009), i.e. with trend and annual cycle removed (right panel).

Regions of persistent currents have temporal scales between 10–40 days, namely along the East and West Greenland and Labrador Currents, the Gulf Stream and its extension, the Canary Current and the North Equatorial Current. In the equatorial region, temporal scales between 20 and 30 days can be seen. It is a region where the annual cycle was not so predominant and short term variability is important. Tropical instability waves have associated periods of around 30 days (*von Schuckmann et al.*, 2008) and may be the cause for the temporal scales estimated in the equatorial band. The small scales in the southeastern South Atlantic (south of 15 °S) are due to eddy activity in the South Equatorial Current, also fed by rings generated in the Agulhas Retroflection.

As can be expected, the temporal scales are reduced (to values below 40 days) almost throughout the entire Atlantic after removing the annual cycle from the model data. This happens especially along the ocean margins and in areas of strong currents (Fig. 3.6, right). In particular the temporal scales can in some places be less than 10 days, making it a difficult task for satellite missions to properly sample the below-seasonal SSS variability. Only in interior ocean regions, where the spatial scales of non-annual variability show large values as well (but the SSS variability is actually low), temporal scales larger than 60 days are found. Some of these places (e.g., off the western coast of Brazil at 5 °S) show residuals from the annual cycle containing still a large seasonal amplitude and therefore, the scales presented in Fig. 3.6 might not solely contain scales related to eddies, but on the other hand, reveal year-to-year variability of the annual cycle.

In the northeastern North Atlantic and in the region north of Iceland the simulated large scales seen in Fig. 3.6 are due to large inter-annual variability, since this signal persists even after removing the annual cycle and happens to occur in places where the SSS std is small.

3.3.3. Impact of SSS relaxation on the estimated scales

As most model studies, also the present model uses a relaxation of the surface salinity field toward a climatology. The need for this SSS damping comes solely from the fact that large uncertainties exist in the precipitation data set of the atmospheric reanalysis used in the forcing (*Lorenz and Kunstmann*, 2012). In past experience, large imbalances of freshwater could lead to a salinity trend and consequently to a huge impact on the Atlantic Meridional Overturning Circulation, rendering the ocean model integration useless. Furthermore, river runoff is only roughly represented in the simulation and most of the seasonal freshwater run-off into the model is insured by the relaxation to the PHC climatology. Therefore, employing surface damping is unavoidable. The choice of a SSS relaxation timescale parameter is, however, difficult since it should be one employed in the whole domain.

In order to have an approximated idea of what oceanic time scales would be physical, the e-folding decorrelation timescales of de-trended and de-seasoned monthly-averaged AMSRE microwave sea surface temperatures were computed. Despite the fact that air-sea coupling might be of importance for setting the temperature damping scales, it is assumed that at the below-seasonal eddy-related timescales, the damping of temperature and salinity should be similar. Microwave data was preferred since it is free from cloud- and aerosol-derived contamination. Not unexpectedly, the scales vary considerably across the Atlantic (not shown), ranging from about 30 days in the northern and eastern parts of the Subtropical gyre to 120

days over the Subpolar gyre and to 150 days in the regions of the North and South Equatorial Currents. These scales actually correspond to the physical eddy/wave ocean scales. This implies that since these features can be seen in the observations, they do not get damped away but survive for quite some time, defining a lower boundary for the relaxation scale.

According to the way the relaxation is implemented in the present model, the SSS relaxation acts only in the first model layer (which in the present case is 5 m thick). Due to mixing, however, the whole mixed layer is affected and the "effective" SSS damping is therefore acting on a much longer time scale as that suggested by the imposed value of the relaxation parameter (in the present case tau=30 days). In fact, one has to take into account the (spatially- and temporally-varying) depth of the mixed layer (mld). The "effective" relaxation timescale is therefore tau*mld(x,y,t)/5. With a mixed layer depth varying in the Atlantic from 25 m to more than 150 m (depending on region and season), "effective" relaxation timescales imposed with tau=30 d range from 150 days to more than 2 years. My conclusion from these comparisons is that the imposed relaxation should not drastically affect the simulated scales of SSS variability.

The field towards which the model is relaxed to is a climatology, thus having only large spatial scales and a seasonal temporal cycle. Although, once again, the eddy/wave structures are "faster" than seasonal and therefore should not be much affected by the "effective" salinity relaxation, it is possible that the spatial scales can be affected. To quantify at which extent this is so, it is used a version of the model at the eddy-permitting (and in some places eddy-resolving) resolution of 16 km, and performed two 10-year-long integrations: the first using the relaxation parameter of the 4-km run (tau=30 d) and the second with a much longer relaxation parameter (tau=180 d). The latter is considered to be a very weak relaxation, with effective damping timescales between 3 and 14 years. Spatial and temporal scales of SSS variability were computed from both experiments and compared.

The scales obtained with the lower-resolution version are, as expected, a bit larger than those obtained with the 4-km model since the resolution does not allow for small scale eddies to be resolved. However, the regional patterns of the zonal, meridional and temporal scales remain the same as found in the high-resolution. Although one can not be completely sure that the sensitivity results presented next can be applied to the high-resolution, running the 4-km model with a longer damping scale was computationally too expensive.

Fig. 3.7 presents the results from the sensitivity of the spatial and temporal scales to the relaxation magnitude. Histograms of the differences in spatial (Fig. 3.7, left) and temporal (Fig. 3.7, right) scales between the moderately strong relaxation and the rather weak relaxation runs show that, when retaining the annual cycle, the relaxation is mainly imposing a shift towards larger scales (the peak of the histogram lies at 10 km but significant occurrences up to 50 km are seen). On the other hand, when removing the annual cycle, the spatial scales seem to be biased low when introducing a stronger relaxation. The peak of the histogram is now centered at 10 km with a larger negative tail. The impact of relaxation on the temporal scales is different from that of the spatial scales in that if retaining the seasonality or not, damping makes the temporal scales always shorter. This can be seen by the tail of the histogram of the differences being biased towards negative values.

Interestingly, there is a regional character to the impact of relaxation; some regions con-

sistently show an overestimation of scales and some other an underestimation. The fraction (as a percentage) between the scale differences relative to the scales from the weak relaxation case is presented in Fig. 3.7, lower panels, showing where the moderate relaxation is overestimating or underestimating the scales of the weak relaxation.

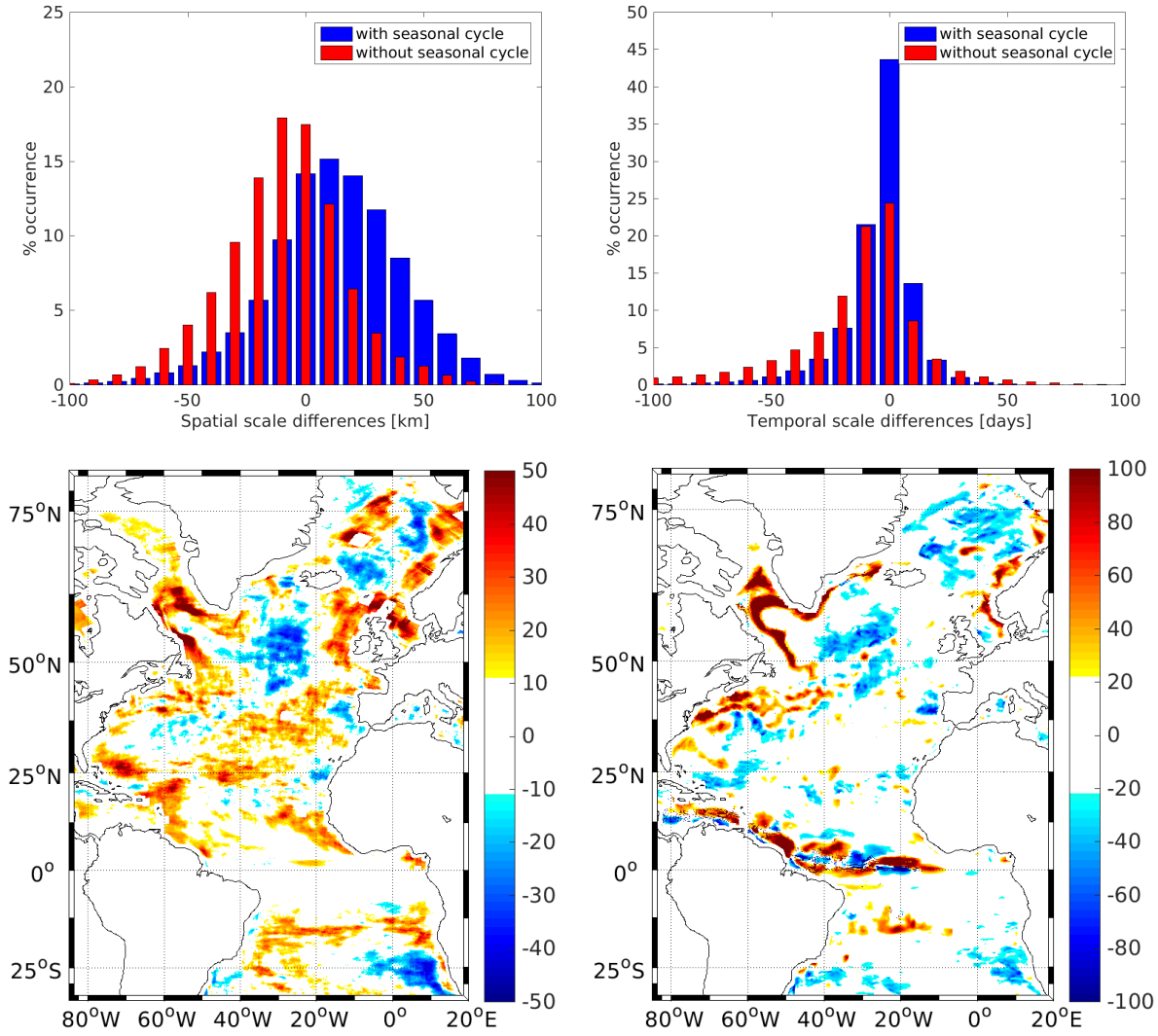

Figure 3.7.: Histograms of the spatial scales differences (upper left) and the temporal scales differences (upper left) between the model runs including a moderate and a weak SSS relaxation to the PHC monthly climatology. Percentage overestimation (positive values) and underestimation (negative values) of the spatial (lower left) and temporal scales (lower right) relative to the weak relaxation run, for the cases retaining the seasonal cycle. The results in this figure were obtained with a lower resolution version (at 16 km) of the 4-km resolution model.

For the spatial scales, it turns out that scales are mainly estimated high by the moderate relaxation in the rim currents of the Labrador Sea, north of the Gulf Stream, in the eastern Atlantic and in the southwestern Atlantic (Fig. 3.7, lower left). On the other hand, spatial scales are consistently biased low in parts of the Subpolar gyre (namely in the Iceland Basin), in the central parts of the Nordic Seas basins and in the southeastern Atlantic.

Turning to the temporal scales (Fig. 3.7, lower right), the places where overestimation occurs seem to correspond to those from the spatial scales, these are regions where a strong low salinity signal is present either from runoff (Amazon and Baltic outflows) or from sea ice melting (East and West Greenland and Labrador Currents). The underestimation regions, i.e., where the moderate relaxation is imposing high-frequency signals, are once again concentrated in the subpolar region north of the North Atlantic Current and in the Iceland Sea and Lofoten Basin.

Translating these results to the high-resolution run, the pattern of spatial scale overestimation shown in Fig. 3.7 accounts for the small discrepancy between the zonal and meridional scales of model and thermosalinograph data presented in Fig. 3.4. The 10 to 20% larger scales found in the model seem to be due to the impact of relaxation. In conclusion, the scales presented in Figs. 3.5 and 3.6 together with the uncertainties shown in Fig. 3.7 are my best estimates of the "true" SSS decorrelation scales.

3.4. Variance Spectra

The preceding analysis of decorrelation scales was motivated by the question which scales characterize the salinity variability. The high-resolution simulation used for the studies above seems to overestimate the mean spatial decorrelation scales by 10 % to 20 % especially in the tropics compared to the observed thermosalinograph sections. It remains unclear if a misrepresentation of the mixing processes in the model might be responsible for the overestimation. However, the standard deviations of the observational scales' estimates are quite high especially for the quasi meridional sections, therefore the differences in scales might contain a high uncertainty.

Another result of the analysis carried out above is the relative strong annual cycle of the model salinity in comparison to its total salinity variance. In order to analyse the scales of salinity variability in more detail, spectral estimates of the potential density changes are calculated for wave numbers and for frequencies of model data in comparison to the observations on thermosalinograph sections and on time series stations.

Power spectral density (PSD) estimation is used to determine how the variance in a signal is distributed in the frequency or wavenumber domain, often enabling inferences about the nature of underlying physical processes. The slope of the wavenumber spectra's decay at the mesoscale and small scales characterizes the spatial distribution of the tracer examined, since it indicates whether the small-scale structures are energetic or not relative to the structures of larger scales.

Surface quasi-geostrophic theory describes the dynamics in the surface mixed layer and predicts surface kinetic and potential energy spectra to scale like $k^{-5/3}$, with k being the wavenumber. Observed surface mixed layer flows have potential energy spectra with a slope of k^{-2} (*Callies and Ferrari*, 2013), the steeper spectral slope than predicted by the surface quasi

geostrophic theory is explained by *Callies et al.* (2015) being due to ageostrophic processes leading to a collapse of the frontal structures.

In surface quasi geostrophic theory the mixed layer dynamics are driven by buoyancy (*Blumen*, 1978), and the potential energy (PE) can be given by:

$$PE = \frac{1}{N^2}[b^2] \tag{3.1}$$

where N^2 is the Brunt-Väisälä Frequency, and b the buoyancy: $b = g\frac{\rho'}{\rho_0}$, i.e. the PE is $\sim \rho'^2$, the lateral density fluctuations. To the first order, the density fluctuations can be written as a linear combination of temperature (T') and salinity (S') fluctuations:

$$\frac{\rho'}{\rho_0} = \beta\ S' - \alpha T', \tag{3.2}$$

α and β are the constant coefficients of thermal expansion and of haline contraction of sea water and $\rho_0 = 1025\ kgm^{-3}$ is the reference density (e.g. *Yeager and Large*, 2007). The seawater density anomalies used for estimating the wavenumber spectrum was calculated using the formula of *Fofonoff and Millard* (1983).

Wave number spectra

With this approximation, it is investigated how far the model SSS variability is reflecting the variability of potential energy, i.e. how large is the variance in the surface density fluctuations due to temperature and salinity. These wavenumber spectra will be compared to spectra derived from the TSG "Polarstern" sections, focusing on the mesoscale to submesoscale (from 300 km to what is possible to resolve with the model resolution applied). The power spectral density (PSD) is estimated via the Thomson multitaper method (MTM *Thomson*, 1982) from the scaled salinity, temperature and the potential density changes along the "Polarstern" thermosalinograph sections. This method attempts to reduce the variance of spectral estimates by using a small set of tapers rather than the unique data taper or spectral window used by Blackman-Tukey methods. A set of independent estimates of the power spectrum is computed, by pre-multiplying the data by orthogonal tapers which are constructed to minimize the spectral leakage due to the finite length of the data set. Averaging over this ensemble of spectra yields a better and more stable estimate than do single-taper methods (*Percival and Walden*, 1993).

The salinity data from the TSG sections were interpolated to a 1 km resolution and the spectra were averaged for overlapping sections of 600 km length. The power spectral density of the scaled model salinity was averaged for one degree latitude and longitude in steps of about 5 ° latitude and longitude and for one year of model data output, i.e. the spectral densities represent an average of more than 8000 sections in the case of the model data, but only up to 14 sections in the case of the "Polarstern" data..

In Figure 3.8 the spectral density resulting from the RV "Polarstern" salinity and temperature section data is compared to the results of the 4 km resolution model data. The geographic origin of the RV data is approximated by the positions of the model output and indicated in the

subplots, the latitudinal distribution from north to south is arranged in two lines of subplots from left to right (compare Figure 3.4 for the positions of the RV data). The mesoscale is defined here ranging from 70 to 250 km, the small scale range from 30 to 55 km and indicated as underlying gray shadows in the plots.

The temperature and salinity sections from the observations show similar energy estimates to the ones from the model output at large spatial scales. The spectral energy level resulting from the observed seawater density anomalies (black lines) are lower than the ones from the respective observed temperature and salinity data. Salinity and temperature changes compensate in terms of density fluctuations, i.e. the salinity and temperature fluctuations correlate well so that they oppose their effect on density, also observed by *Kolodziejczyk et al.* (2015). However, this is not always the case for the model output. The northernmost region seems to be an exception in this respect, there, the observed salinity fluctuations seem to determine the seawater density fluctuations, since the spectral density level of temperature fluctuations is lower than the ones from salinity and seawater density, however, the observational spectral estimate is based on only few TSG sections and thus do not represent a general behaviour. The observations in all other regions reveal a flat plateau at large scales (>300 km) and decay with spectral slopes of $k^{-1.4}$ to $k^{-1.8}$ at mesoscale reflecting the surface quasi geostrophic predictions. At smaller scales (< 55 km) the slopes are getting steeper when after *Callies and Ferrari* (2013) ageostrophic processes are becoming relevant. The model temperature and salinity data show already steeper slopes of $k^{-2.2}$ to $k^{-3.7}$ at mesoscale and decay strongly at small scale.

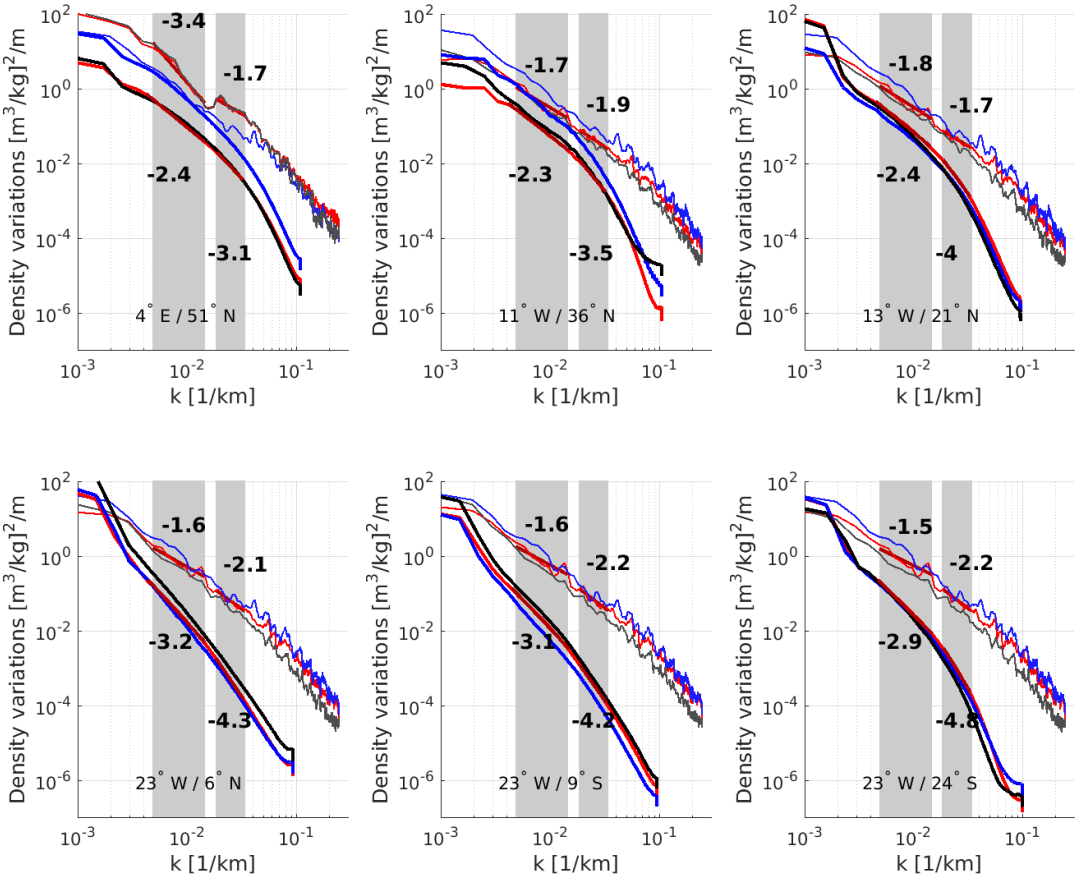

Figure 3.8.: Power spectral density of scaled salinity, temperature and seawater density anomalies (red, blue and black lines) averaged along quasi meridional sections from RV "Polarstern" thermosalinograph data during several cruises across the Atlantic during 2005 to 2010 (thin lines), and from model data (thick lines) at similar positions from one year of model output. Averaged positions are given in the subplots, passing from the North to the South Atlantic. Slopes of the salinity spectra were fitted in the mesoscale (70 to 250 km) and the small scale (30 to 55 km) ranges (gray shadings) and overlaid as thick red line, the respective spectral slopes are indicated.

The salinity diffusion in the model is parametrized by a Laplacian operator, which damps the grid scale anomalies with very low damping time. However, the salinity equation also includes advection, and the velocity is damped by a biharmonic viscosity operator. The intention of biharmonic mixing is to damp numerical oscillations. Assuming that a disturbance in the velocity can be described as a wavelike feature, so that e.g. its variation in the horizontal direction x is $S(x,t) \sim e^{(\sigma t + ikx)}$, with wave number $k = 2\pi/\lambda$ and $\sigma = -\kappa k^{-4}$, κ the coefficient of horizontal biharmonic viscosity, the exponential damping time τ due to the biharmonic diffusion is $\tau = \frac{1}{\kappa}(\frac{2}{\delta x} sin(k\frac{\delta x}{2}))^{-4}$ (*Delhez and Deleersnijder*, 2007). With a resolution of

$\delta x = 4\,\text{km}$, the damping time is $\tau < 10\,\text{days}$ for $\lambda < 40\,\text{km}$ whereas $\tau > 160\,\text{days}$ for $\lambda > 90\,\text{km}$, i.e. the disturbances on smaller scales are damped rapidly, whereas the disturbances on longer wavelengths are maintained.

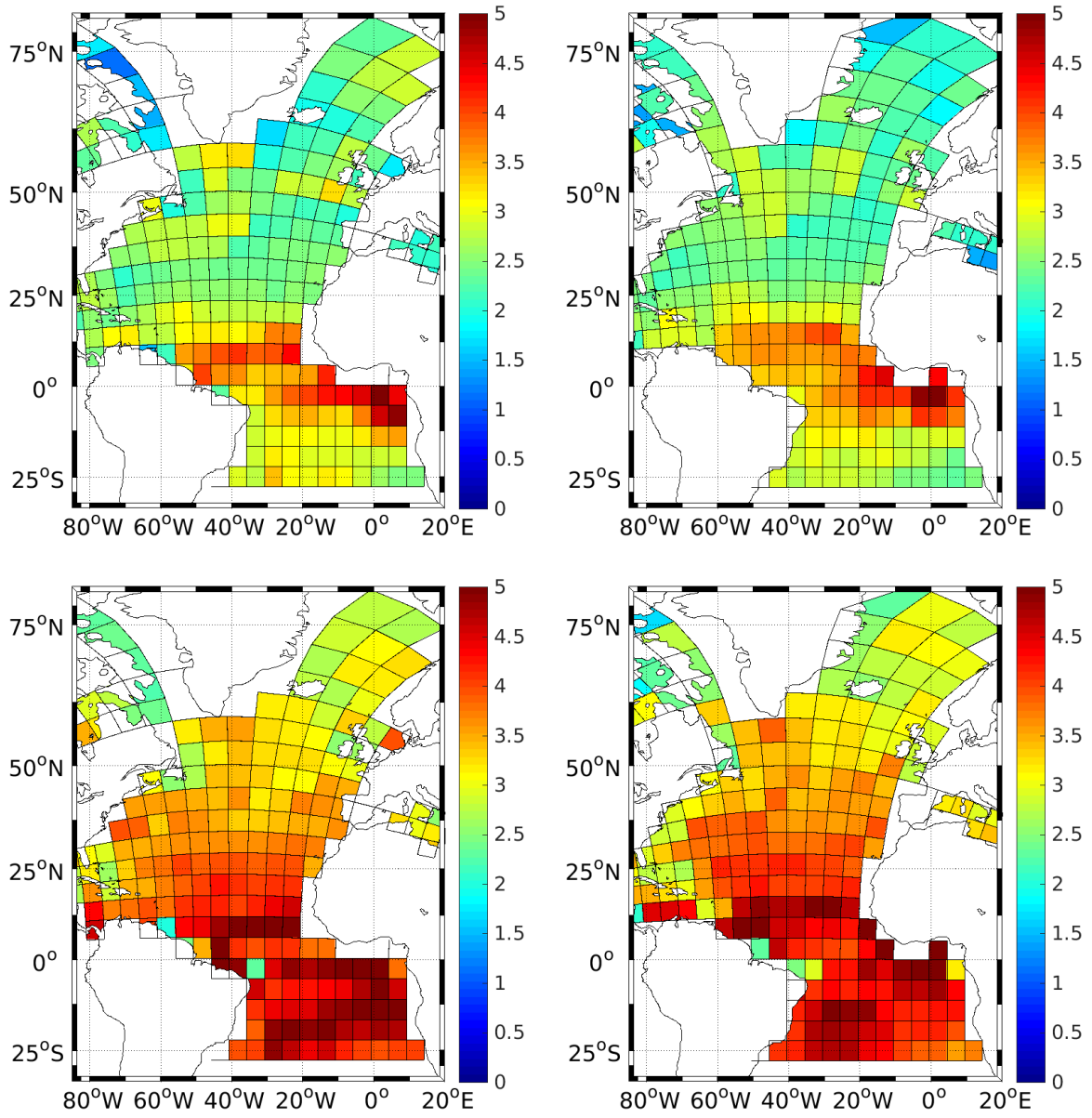

Figure 3.9.: Slopes of of wavenumber power spectral density from zonal (left) and meridional (right) sections of model salinity anomalies from one year of model output, fitted in the mesoscale (70 to 250 km, upper panels) and in the small scale (30 to 55 km, lower panels) ranges.

The spectral slopes at the small or mesoscales can be interpreted as being representative

for the damping strength due to the dissipation of small-scale buoyancy disturbances. Figure 3.9 shows the geographic distributions of the spectral slopes in the model domain. Strong dissipation of the mesoscales is found in the tropics, while the small scale disturbances are damped strongly everywhere in the model domain, however, steepest slopes, i.e. lowest energy at the small scale range is found in the off-equatorial tropics.

The latitudinal distribution of the slopes in the mesoscale range may reflect also a natural feature of the mixing scales. The latitudinal distribution of the spectral slopes resulting from the thermosalinograph sections was checked in this respect. The slopes revealed similar values of -2 throughout the latitudinal range of the Atlantic (not shown in detail, but this statement can be inferred from Fig. 3.8). However, the thermosalinograph sections reflect the spectral characteristics of the mixing regimes in certain longitudinal areas, moreover constitute an average of only a small number of sections. The choice of fixed spatial intervals for the mesoscale and the small scale also may influence the distributions of the spectral slopes in Fig. 3.9. A latitudinal dependence of these intervals, e.g. dependent on the first mode baroclinic Rossby radius of deformation could give different slopes, especially for the mesoscale range.

Stammer (1997) and later *Eden* (2007) related the decay of the spatial decorrelation scale to the north of about 30 °N and to the Rhines scale equatorward of this latitude. As noted in *Eden* (2007)

Frequency spectra

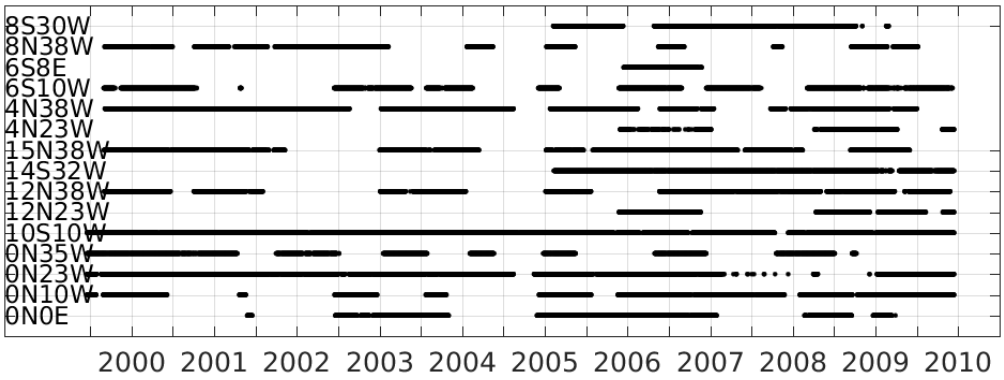

Figure 3.10.: Availability of uppermost salinity data at the time series stations of the PIRATA array during the time period 2000 to 2010. The geographic coordinates are given at the left side.

The frequency spectra, computed from the uppermost time series station data, are compared to the spectra computed from time series at the correponding positions from the model data. The availability of the time series measurements (Figure 3.10) do not allow to derive the full spectra including the annual cycle at all stations, so the spectral estimates are confined to the longest continuous time series section available. The gaps between the sections were filled by linear interpolation in order to minimize any spectral leakage.

The spectral energy levels of the salinity anomalies resulting from the observations and the model data shown in Figure 3.11. They are similar to each other at large temporal scales >20 days. Especially in the frequency band of 1/80 to 1/20 days^{-1}, including the tropical instability waves along the equator and at 4 °N, the model captures well the observed variance levels. The annual cycle in the model results is evident in the off-equatorial regions, and the annual and semiannual frequencies show a flat spectrum. The annual cycle at the in situ mooring stations is hardly resolved, so that the variance levels at the annual frequency cannot be compared.

At the shorter time scales (< 20 days) the model reveals much lower variance in the salinity anomalies than the observations. Whereas the observational results follow the k^{-2} decay in the spectrum, the model results follow the k^{-3} or even k^{-4} decay. At the southequatorial stations, (8 °S/30 °W and 10 °S, 10 °W), the decay begins at about 1/70 days^{-1}, whereas the equatorial stations show the strong decay in the model's variance only below 20 to 10 days.

These results of the spectral estimates explain better why the annual cycle contributes to a higher rate to the total salinity variability as the one calculated from the observed salinity data. They show, that the salinity variability is present also in the model an short time scales, however, at a lower energy level in comparison to the variability on longer time scales.

Accordingly, also the wavenumber spectra show, that there is small-scale variability in the model, but this is when competing to variance on larger scales underrepresented by averaged spatial decorrelation scales. Since the distribution of the relation large to small scale variance is regionally different, this introduces a latitudinal relation. The dependence of the spatial scales of variability on latitude still deserves further investigation. In the present study the question remains open if the apparent maxima of spatial variability scales in the tropics (Fig. 3.5) is due to the underlying physics, or due to the parametrizations applied in the circulation model.

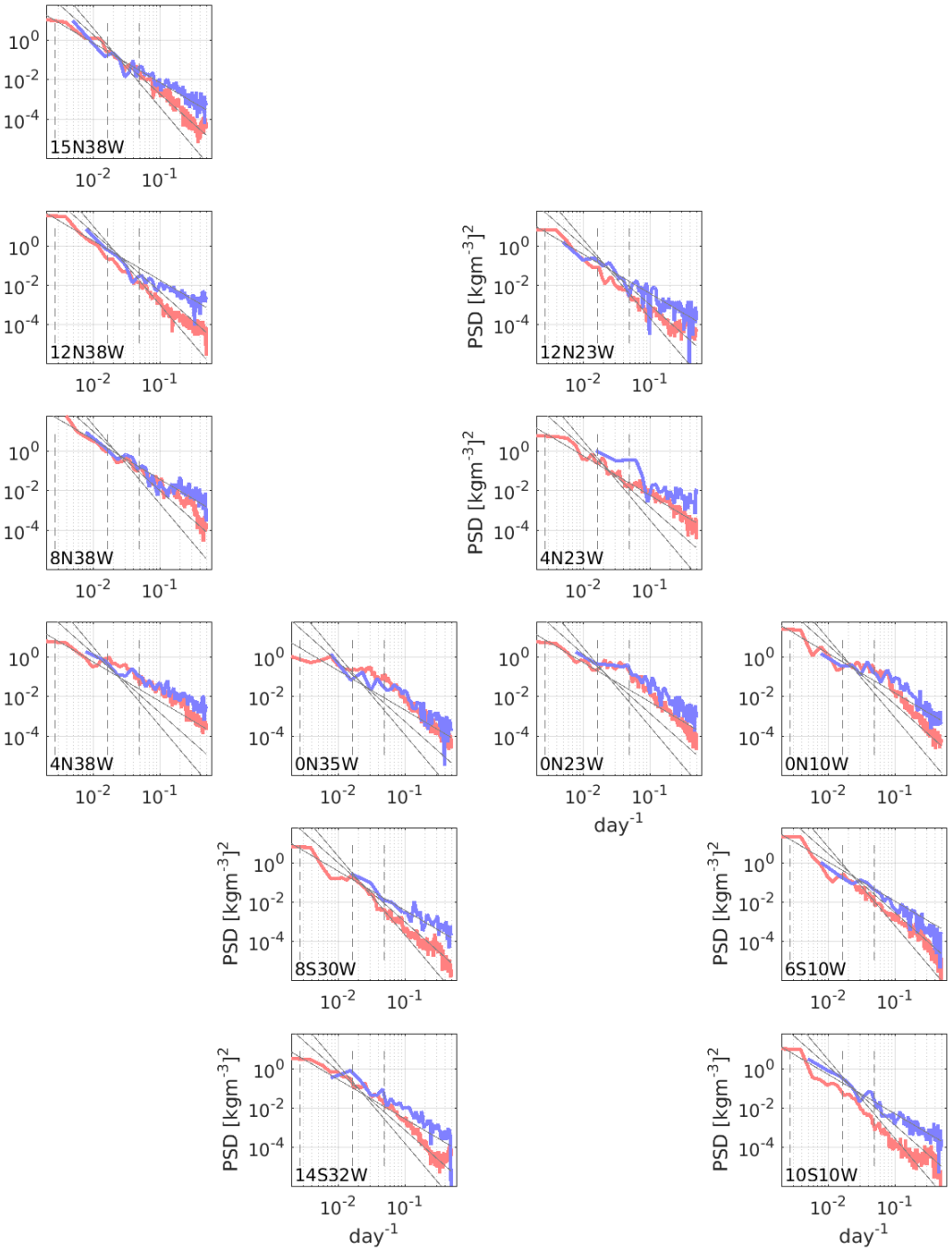

Figure 3.11.: Power spectral density from the uppermost scaled salinity data at the time series stations of the PIRATA array (blue) and the corresponding time series from the high resolution (4 km) MIT gcm output (red). The thinner gray lines show the spectral slopes of f^{-2}, f^{-3} and f^{-4} and serve as a reference. The vertical dashed lines correspond to periods of 365, 60 and 20 days. The arrangement of the subplots roughly corresponds to the geographical positions of the PIRATA moorings, which are given in each subplot.

3.5. Summary

In order to quantify spatial and temporal variations of SSS variability, the total SSS variance and the contribution of its annual component, as well as spatial and temporal decorrelation scales, were computed from observations and model results for the Atlantic Ocean between 30 °S and 80 °N. The in situ measurements showed that a large fraction of the SSS variability in the Atlantic is explained by the annual harmonic, especially in the tropical band, the western rim of the Atlantic and in the eastern subtropics.

As the model results for the uppermost salinity resemble well the observational estimates in terms of total and annual variability, and since very similar spatial scales along the sections sampled by thermosalinographs on voluntary observing ships and on the RV "Polarstern" were obtained, the model SSS fields were further used to compute decorrelation scales in the entire Atlantic, i.e., also in regions that have not been observed sufficiently. Since the SSS variability has a strong annual component, the latter has an impact on the estimated spatial and temporal scales. Therefore, decorrelation scales were not only computed for the total SSS field but also for the SSS anomalies from the annual cycle. The scales including the annual cycle are similar to the ones found by *Delcroix et al.* (2005) in the tropical Atlantic; but subtracting the annual cycle of SSS resulted in much smaller spatial and temporal scales.

While of interest in its own right, the results can serve as a basis for studies dealing with the interpretation of SSS variability observed by the ESA "SMOS" and the NASA "Aquarius" missions, which, depending on the region under study, need to average the satellite retrievals taking into account the SSS variability scales. As shown here, a spatial resolution of a 100 km×100 km of a satellite SSS product will hardly be able to resolve all scales of SSS variability, especially not in high latitudes, where much of the non-seasonal SSS signal will be averaged out. However, in the equatorial Atlantic, and, to some extent, also in the subpolar basin, zonal variability could be captured on these large scales. As shown in *Köhler et al.* (2015), SSS variability patterns can be reproduced quite well in the North Atlantic using the SMOS SSS L4 data (http://cp34-bec.cmima.csic.es/data/available-products), a data set produced by fusing the SSS retrievals with sea surface temperature data and conserving spatial gradients.

Satellite missions will be capable of detecting the annual signal with acceptable accuracy after averaging with a monthly basis (*Grodsky et al.*, 2014). However, one should be aware of the short term variability within the averaging period to prevent large aliasing. With the purpose of finding the decorrelation temporal scales within the period of averaging, the time series at the mooring stations and from the model were divided into intervals of 30 days. After temporally detrending inside those periods of 30 days, the e-folding scales were recomputed and averaged, thus giving averaged temporal decorrelation scales associated with exclusively eddies/waves and fast atmospheric processes (Fig. 3.12). The SSS from several moorings show temporal decorrelation scales below 30 days of 3.4 days for the northern moorings (Stations M and BATS were not included since the temporal sampling is not sufficient) and between 3.8 and 4 days in the tropics. In the model, the decorrelation scales are about 4 ± 1 days. There is a slight dependence on latitude and a tendency towards longer scales along the North and South Equatorial Currents, but this lies within the standard deviation of the temporal scales

and its significance is questionable. These short decorrelation scales compare well with the ones found by *Delcroix et al.* (2005).

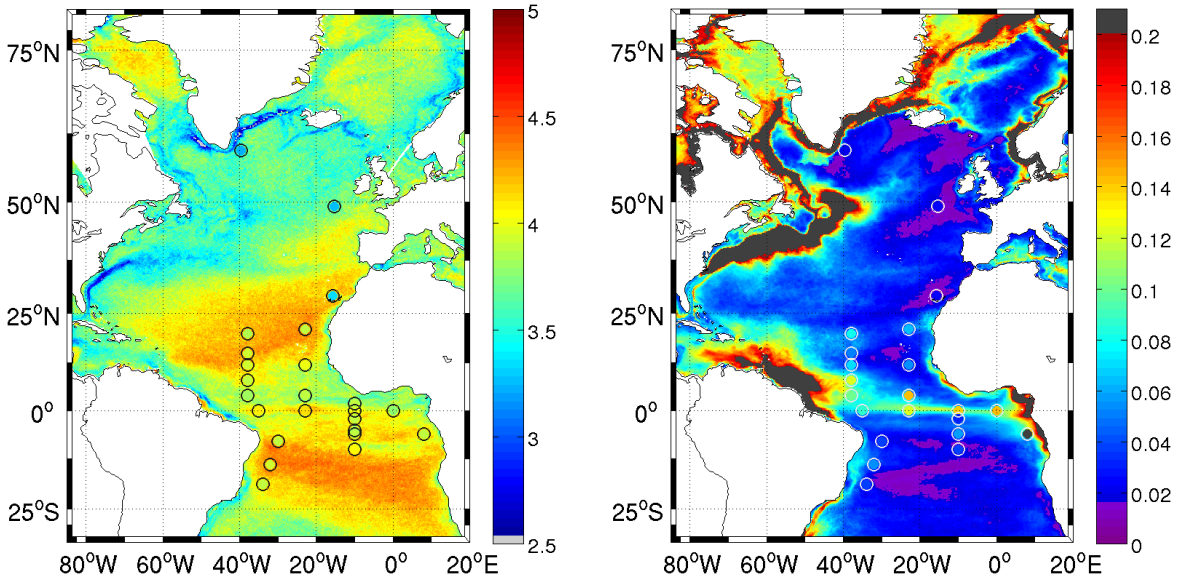

Figure 3.12.: Temporal scales (in days) computed from model SSS output in time segments of 30 days. Superimposed are the respective results computed with mooring data from the PIRATA and EUROSites stations (left). Standard deviation of SSS (in) computed in time segments of 30 days for the same datasets (right).

Decorrelation scales of 4 days imply that there are at most three independent observations in a period of 10 days, and therefore an averaging period with more than 10 days is recommended in order to avoid the possibility of aliasing. Finally it is computed how much of the variance still remains in these temporal segments of 30 days (Fig. 3.12, right panel). The remaining processes still account for a very significant amount of SSS standard deviation, namely up to 0.06 throughout the Atlantic. The spatial pattern of the remaining variance closely resembles the total SSS variability: values up to 0.3 at the sea ice edge in the Nordic Seas and Labrador Sea; also comparably large values north of the Gulf Stream, at the mouth of major rivers and at the exit of the Baltic Sea. These are regions where large-amplitude fast processes make observing SSS challenging.

Vinogradova and Ponte (2012) attempted to derive the aliasing error from the HYCOM model data. They found typical values in the open ocean of 0.02, where SSS variability is weak in general. In contrast, several coastal, tropical, and western boundary current regions yield high values of a >0.1 with a maximum >0.9.

The temporal decorrelation scales (below 30 days) of about 4 to 5 days derived in this work from the mooring and model results suggest that attention has to be payed to the period of averaging. SMOS retrievals cover the globe within 3 days, whereas Aquarius reaches global coverage after 7 days, i.e. a 10 day average just includes 2, maximum 3, independent SSS observations, which are deemed insufficient for obtaining an un-aliased SSS product. *Vino-*

gradova and Ponte (2012) found that aliasing energy is still negligible at annual periods, but can account for more than 17 % at periods <4 months in tropical regions, western boundary currents or regions of river discharge. From model fields the SSS variability within the periods of 1 month still may achieve 0.1 or higher in half of the model domain, i.e. this represents a sampling error of > 0.1 in vast areas (*Köhler et al.*, 2015, see also). The sampling error resulting from the model output seems to be underestimated when compared to the results of observed time series stations showing slightly higher energy levels in the spectral estimates (Fig. 3.11) and also in Fig. 3.12.

The non negligible salinity variability found on short scales is also relevant for validation studies of the satellite derived salinities. Validation is done with direct comparison of in situ data, from Argo profilers or from ship-borne measurements, and collocation of data pairs is taken within a radius of 50 to 100 km, and a time window of several days. This validation cannot be better than the sampling error in the region.

As shown by *Yu* (2011) and *Bingham et al.* (2012), there are regions where the dominant forcing term is the atmospheric forcing (evaporation minus precipitation). In these regions, one could expect that the satellite-derived SSS would show a higher seasonal amplitude forced by the seasonal variations of E-P. However, *Köhl et al.* (2014) assimilating SMOS SSS data into a global coupled ocean-sea ice circulation model, and therefore adjusting the fresh water forcing to the SSS fields, could not confirm any enhancement of the annual cycle in the surface salinity.

4. Validation of SMOS salinity

4.1. Introduction

A first step in new measurement technologies is the validation of the acquired data by comparing them with the existing ones. The validation of the SMOS data is done with in situ data, originating from several different measurement platforms as described in chapter 2.2. An estimate of the accuracy of SMOS SSS can be given by comparing the satellite derived SSS data product to similar products from in situ observations. SMOS data is available in several processing levels: Whereas L1 data contain the brightness temperature, L2 data contain the sea surface salinity based on half-orbit wise data. It is distributed by the ESA to the different calibration and validation efforts in several countries, and the data used here are based on the salinity retrieval version 5.50, downloaded in the frame of the German calibration and validation activity 'SMOS Cal/Val I+II'. L3 data products contain data filtered and averaged on certain spatial and temporal intervals. For L3 products several data centres have produced bias corrected products, and validated these. Summarizing these studies, the salinity accuracy results in 0.3 under favourable conditions, i.e. with moderate wind and temperature exceeding 10 °C, and excluding problematic regions such as high latitudes, rainy regions and regions close to land (*Boutin et al.*, 2012; *Hernandez et al.*, 2014).

Each of the in situ salinity measurement method is different from that of the satellite derived salinity, therefore the direct comparison has its caveats: The point-to-area-transfer, the different depths of the measurements or Eulerian versus Lagrangian measurements. The point measurements are subject to an often unknown sampling error which can reach 0.2 in the open ocean (*Vinogradova and Ponte*, 2013b; *Sena Martins and Stammer*, 2015, see also chapter 3). Moreover, the vertical salinity gradients between the surface and a few meters depth can reach > 1 in regions of high precipitation or river run-off (*Henocq et al.*, 2010).

Measurements very near to or directly at the sea surface are not available on a global basis, the data nearest to the surface used here are the surface drifters in a region south of Tahiti. The drifters are equipped with a conductivity cell at about 45 cm below the sea surface (see chapter 2.2).

In the present chapter the SMOS SSS data validation will be carried out on the L2 level. In contrast to the monthly mapped L3 products, the L2 data still suffer from radiometric noise and uncertainties due to the assumptions and models included in the salinity retrieval. However, it has the advantage of closer collocation in time and space with the in situ data. In this aspect, a better knowledge of temporal and spatial decorrelation scales is very useful, then the collocation may be confined to these scales. Unfortunately, the in situ data are too sparse, to use the scales developed in chapter 3. Therefore wider radii in time and space are used for finding the pairs of collocation.

The available in situ data are used for analyzing salinity differences to SMOS in order to develop a bias correction for the L2 data. Any dependency of the salinity differences on parameters such as temperature, wind and latitude as well as the geometry of the satellite measurements is checked for its use in developing a potential bias correction function. After validation, a bias correction is calculated from the differences to the in situ data and applied to the L2 data. Subsequently, the monthly SSS products are computed which include an estimate of the errors in the bias corrected salinity fields.

The development of the salinity retrieval algorithms is done at the expert salinity laboratories (ESL) commissioned by ESA and will not be subject here. The SMOS data used in this study have undergone already a step of correcting the bias in the open ocean (OTT, see section 2.1.3) and the task of the present study is to depict the regional and temporal distribution of the remaining bias and the accuracy of the salinity at different surface conditions.

4.2. SMOS Salinity differences to in situ data

For calculating the differences between in situ and space born salinity measurements, data pairs have to be collocated. Precise collocations are performed by taking in situ data found within the grid boxes of the gridded L2 SSS SMOS salinity (1 °× 1 °) within 3 days before and after the satellite overpass. This time period is slightly higher than the temporal decorrelation scale derived in chapter 3 spanning one week. It constitutes a compromise between the derived temporal scale and the data availability.

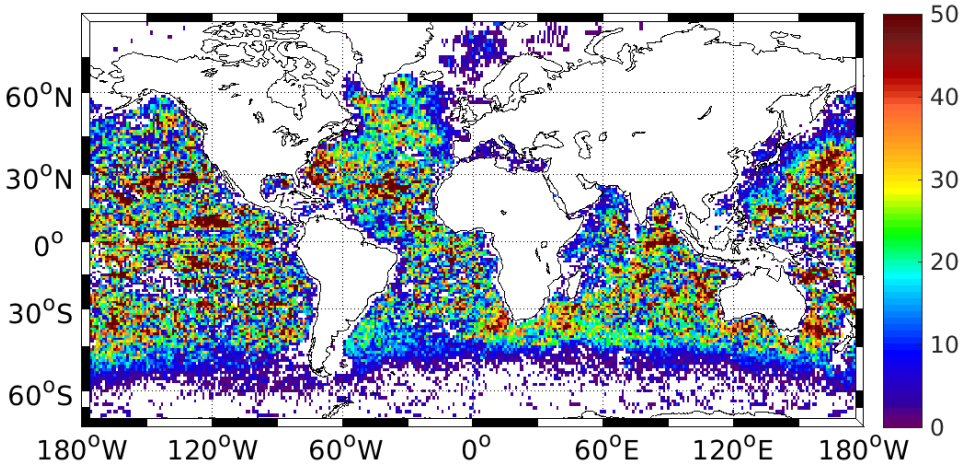

Figure 4.1.: Total number of data pairs per grid box (1 °× 1 °) used for the validation of the SMOS L2 salinity data collocated within ± 3 days for the descending half orbits within the time period February 2010 to December 2014.

The number of collocations per grid box from the descending satellite half orbits and the in situ data within the years 2010 to 2014 is shown in Figure 4.1. The distribution for the ascending half orbits is very similar to the one of the descending arcs.

The data pair coverage available for the SMOS L2 validation is sparse in the polar and subpolar regions as well as in some other regions of the global ocean, e.g. in regions of swift currents, broad shelf areas and around China and India. This is not only due to the Argo profilers being rapidly advected out of a region with strong currents, but also due to the SMOS data which are discarded because of RFI or other reasons for bad retrieval quality. Figure 4.2 shows that most grid boxes have 10 to 50 collocations, but also that about 22 % have < 10 collocations during almost 5 years considered in the present study. At the positions of time series stations (e.g. TAO array) the data coverage shows > 100 collocations, but they constitute only 0.5 % of all sampled grid boxes.

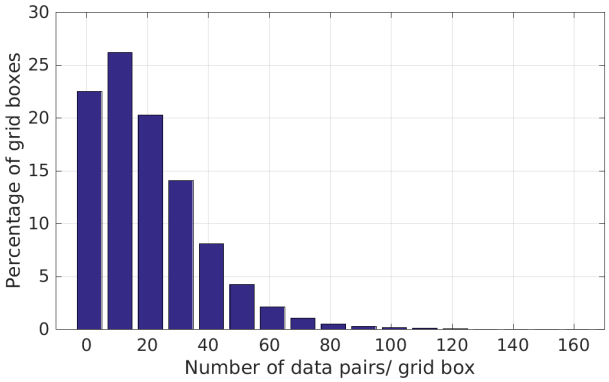

Figure 4.2.: Histogram of total number of data pairs per grid box as in Figure 4.1.

The time-mean salinity difference between ascending and descending arcs L2 SMOS SSS and single Argo salinity values is shown in Figure 4.3. The ascending half orbits show a negative mean bias in the open ocean, especially in the northern hemisphere. Only in the eastern subtropical areas of the Atlantic, Pacific and Indian Oceans, the bias is slightly positive. In contrast, the descending half orbits show mostly positive bias in the subtropical and subpolar regions far from land.

Both half orbits show strongest negative bias as large as 2 in the coastal areas extending several hundreds of km from large land masses, which reflects the effect of land contamination. The descending orbits show narrower bands of negative bias but also a shadow like pattern with positive bias further offshore (western sides of the continents). Noteworthy is, that especially in the areas where SMOS data show poor quality such as land and ice-contamination, the in situ data coverage (Figure 4.1) is also poor.

In several areas the measurements of SMOS are also influenced by RFI, i.e. illegal human made radio emissions at L-Band. The areas particularly affected by RFI are southern Europe, Asia, the Middle East and the coastal zones of China (Figure 4.3). The attention is drawn on patterns of positive bias, a prominent one along about 60 °S to 50 °S in the southern ocean for both half orbits, and some grid boxes in the northwestern Atlantic and the northwestern area of the Pacific. These positive patterns will be investigated in more detail later.

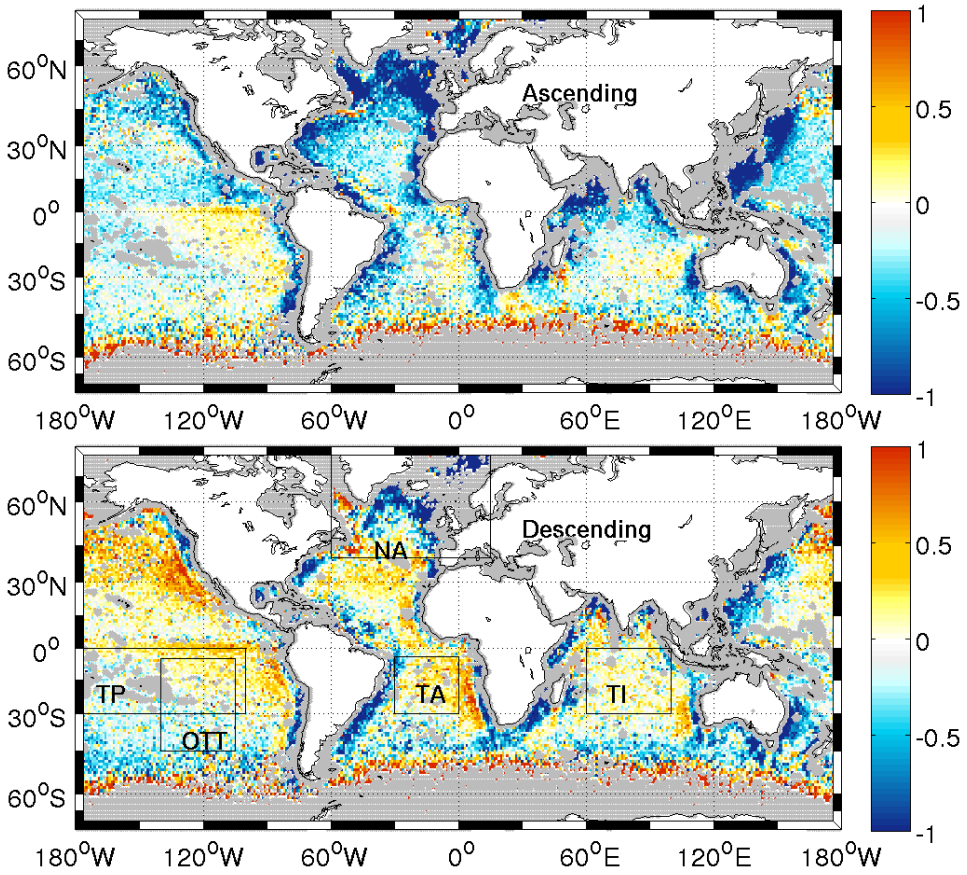

Figure 4.3.: Time-mean difference of salinity between L2 SMOS SSS ascending (upper panel) and descending orbits (lower panel) and top most Argo salinity single values collocated within ± 3 days and 1 °× 1 °during the period February 2010 to December 2014. The lower panel includes the areas for which the differences to in situ data will be illustrated in more detail. Gray areas indicate the regions where no datapairs are found.

Figure 4.4 summarizes the global mean bias averaged over all 5 years for the 3 roughness models (described in chapter 2.1.3). The skewness of the bias distribution in both panels shows cases where the SMOS salinity is lower than the in situ values, which mostly reflects the effect of the land contamination, but also includes the regions, where precipitation leads to natural vertical gradients between the depths of measurement. Differing mean bias between the different roughness models are not evident.

The effectivity of the time dependent bias correction with the OTT procedure (ocean target transformation, compare chapter 2.1.3) is illustrated in Figure 4.5. The development of the bias during the measurement period for the ascending half orbits shows negative values throughout the years, but reveal a weaker and even positive bias in the spring months around April, and especially strong negative bias in December/January and July. A trend in the 5

years of measurements could not be detected, since the regression did not confirm any linear trend. In January 2011, a part of the SMOS antenna showed a malfunctioning during 3 days. During 2014 the data is operational and not reprocessed, therefore the OTT of the preceding 2 weeks is performed and not an OTT centered on the date of the retrieval.

In 2014, the bias values and its variations are higher, especially for the descending half orbits (Figure 4.6). The standard deviation (std) is always at values near 1, no trend could be confirmed by regression either. The descending half orbits reveal lower negative bias in the boreal winter months and suffer at the operating mode from stronger bias than the ascending half orbits. Its std are generally higher than the ones from the ascending half orbits, and also here, no trend can be confirmed by the regression over time.

Figure 4.3 includes the areas in which the temporal evolution of the L2 salinity bias was computed, and Figure 4.7 shows an example for the North Atlantic, which reveals the strongest bias and bias variation of the areas considered.

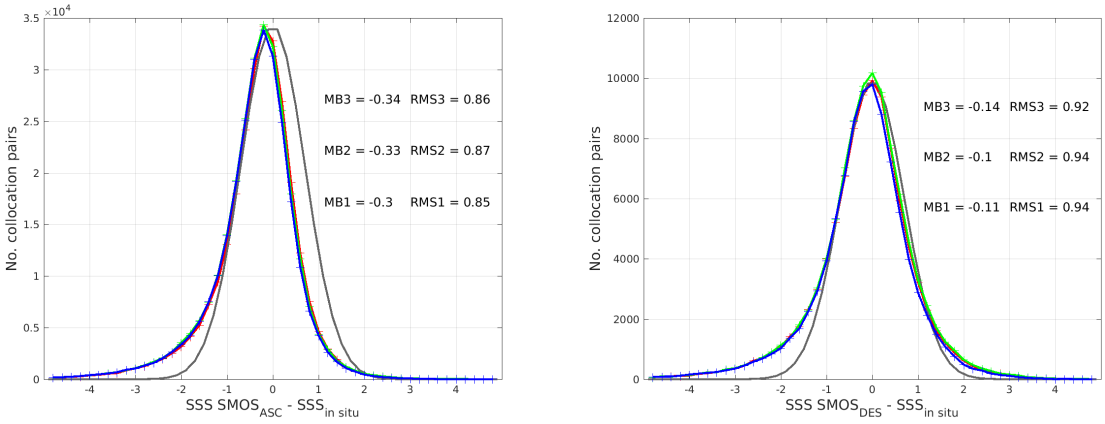

Figure 4.4.: Global mean and time averaged bias and root mean square (RMS) difference in the SMOS salinity for the years 2010 to 2014 and for the ascending (left panel) and the descending (right panel) half orbits. The mean bias (MB) and the RMS differences are indicated for each salinity roughness model. The gray curve is a Gaussian distribution for reference.

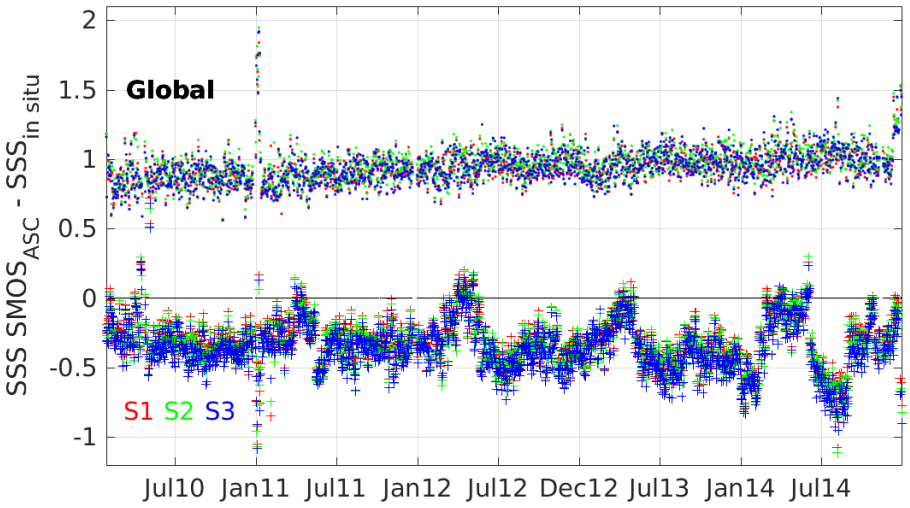

Figure 4.5.: Global mean daily salinity differences (+) and respective standard deviation (dots) between SMOS L2 ascending half orbits to single in situ measurements in the period of February 2010 to end of 2014, collocated in a spatial distance of about 50 km and a temporal interval of 3 days. Differences in the different roughness models are color coded as indicated.

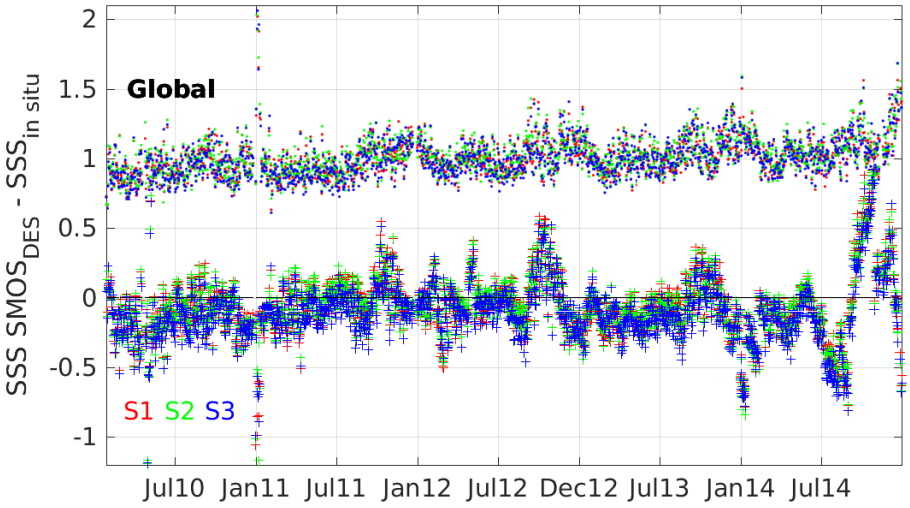

Figure 4.6.: As Figure 4.5, but for descending half orbits.

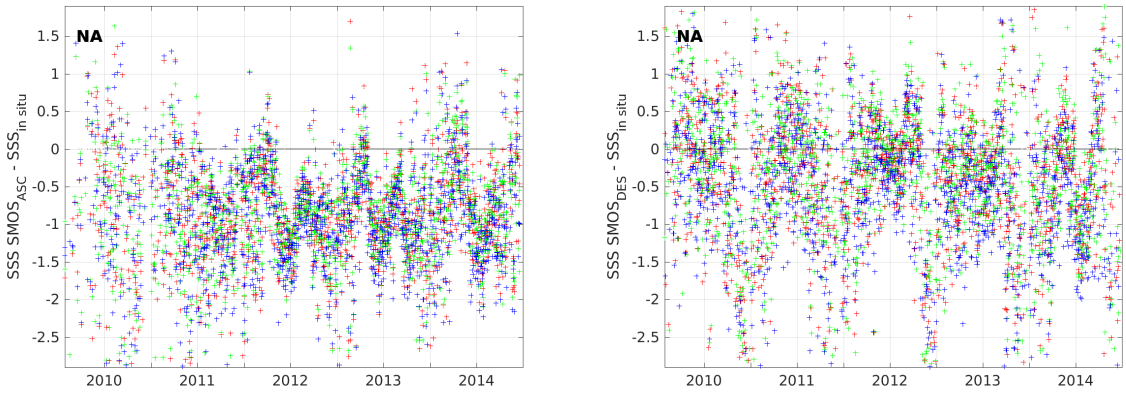

Figure 4.7.: Regionally averaged daily salinity differences (+) between SMOS L2 ascending (left panel) or descending half orbits (right panel) and single in situ measurements over the years 2010 to 2014 for the North Atlantic area (60 °W – 20 °E, 40 °N – 75 °N). Color coding as in Figure 4.5.

The ascending half orbits show a strong negative bias in the North Atlantic and a strong variation, too (Fig. 4.7); positive values are also found, mostly in the second half of the years. The descending half orbits reveal a relatively weak negative bias, however, the variations found are even higher than in the ascending half orbits.

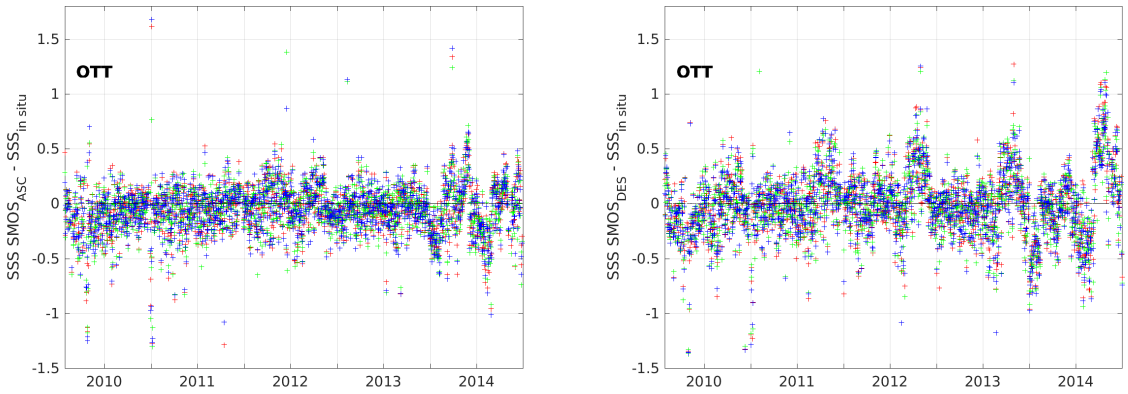

Figure 4.8.: Regionally averaged daily salinity differences (+) between SMOS L2 ascending (left panel) or descending half orbits (right panel) and single in situ measurements over the years 2010 to 2014 for the OTT region (140 °W – 105 °W, 40 °S – 5 °S). Color coding as in Figure 4.5.

The lowest bias is found in the area called 'OTT' in the southeastern Pacific. This area is used for calibration in the reprocessing chain (until the end of 2013) and in the operational

mode in 2014, because it is assumed to be far from any RFI and land contamination. However, the bias found is not zero, and even varies with time, in the descending stronger than in the ascending half orbits. The mean and the std of the differences between satellite and in situ salinity data for the ascending and descending half orbits for all areas and roughness models are given in Table 4.2. No significant differences between the roughness models can be specified. The table shows the time-mean bias and the respective std in the regions indicated in Figure 4.3. The lowest bias and the lowest std are found in the region 'OTT'. Also the tropical regions reveal a very low mean bias, but the std amounts to 0.54 or higher, especially the descending half orbits show a higher std than the ascending ones in all regions. The reason for this difference in variability may be related to the galactic noise whose influence degrades the descending stronger than the ascending orbits.

Region	MB	(Mean Bias)		STD	(standard	deviation)
ASC	S1	S2	S3	S1	S2	S3
OTT	0.023	0.013	0.038	0.461	0.467	0.458
NA	-0.869	-0.843	-0.900	1.113	1.138	1.162
TA	-0.247	-0.240	-0.250	0.625	0.629	0.623
TP	-0.012	-0.021	-0.031	0.545	0.552	0.541
TI	-0.319	-0.361	-0.363	0.712	0.720	0.722
DES	S1	S2	S3	S1	S2	S3
OTT	-0.078	-0.067	-0.056	0.578	0.583	0.564
NA	-0.539	-0.452	-0.630	1.203	1.225	1.231
TA	-0.008	-0.027	-0.038	0.666	0.662	0.647
TP	-0.112	-0.120	-0.143	0.629	0.629	0.610
TI -	0.014	-0.084	-0.081	0.766	0.752	0.751

Table 4.1.: Mean bias and standard deviation of the SMOS salinity compared to in situ salinity during 2010 to 2014, in the regions shown in Figure 4.3 and delimited by the longitudes and latitudes as following: OTT: 45 °S – 5 °S and 140 °W – 105 °W, NA: 40 °N – 75 °N and 60 °W – 20 °E, TA: 30 °W – 0 °W and 30 °S – 4 °S, TI: 60 °E – 100 °E and 30 °S – 0 °S, and TP: 180 °W – 100 °W and 30 °S – 0 °S.

4.2.1. Vertical near surface salinity gradients

Some differences may be explained by the different depths of the salinity measurements: Whereas SMOS measures in the upper centimeter of the ocean surface, the in situ data usually originate in a depth of several meters. The potential vertical gradient between these 2 levels of measurements will be elucidated in the present section.

Differences between salinity measurements at the sea surface and at several meter depth may arise from freshwater forcing due to rain, evaporation and river run-off. Exploring the vertical gradients in the first upper meters in the water column is hampered by the lack of samples above 4 dbar, the Argo profilers are ceased to measure above this depth. The pump flushing the conductivity cell of the Argo profiler is switched off to prevent the intrusion of

biological matters into the cell and prevent it from fouling. The CTD instruments measuring from ship are usually adapted to the seawater temperature at a depth of certain meters, before being lowered. Even if the heaving to 2 m and subsequent lowering is done under calm conditions, the first meters are influenced by the movement of the ship and the CTD instrument and the eventually attached rosette itself, so that the measurements in the upper meters do not capture the actual salinity gradient.

Due to the necessity of having salinity water samples as near to the sea surface as possible, *Anderson and Riser* (2014) published a study about Argo profilers equipped with a secondary unpumped CTD unit, being active in the upper 30 m and at a calibration point in 2000 m depth. It is calibrated against the primary Argo's CTD proven to be stable. The study involves 62 profilers which were deployed mostly in low latitudes. Salinity gradients are small in more than 80 % of the time, and gradients fall off rapidly in the first 4 m; similar results were also found by *Henocq et al.* (2010). Largest gradients were found at wind speed less than 6 m/s. Strong heating and freshwater input such as rain combined with calm weather allow high stability conditions to persist over several hours (see also *Price, James F.*, 1979). In cases of freshwater supply and light winds, diurnal insolation has a stronger heating effect due to stronger stratification and weaker cooling from below (*Anderson and Riser*, 2014). The interaction between the sea state and the rain rate influencing the salinity gradient in the upper meters was subject of the study by *Asher et al.* (2014). They concluded, that the vertical salinity gradient is dependent in first order on the rain rate, and in second order on the wind driven vertical mixing, especially at low rain rate.

Negative SSS anomalies may be mixed vertically further into the water column in regions of increased heavy rainfall and winds associated e.g. with the monsoon and influence of river runoff (*Anderson and Riser*, 2014). In regions, where the gradients reach greater depth can be seen also in the 'normal' Argo profilers not equipped with a secondary CTD. The gradients between the 2 uppermost measurements from the Argo data in 2010 to 2014 were computed. The data were chosen carefully in terms of quality, the shallow data originating at 1 to 6 dbar, the second at 5 to 12 dbar. In Figure 4.9 the locations are plotted where the negative salinity gradients exceed -0.1 m^{-1}. The size of the circle denotes the strength of the gradients, only discernible at single locations. The density of the colored dots reflects qualitatively the frequency of occurrences of a negative salinity gradient within the depth interval of 1 to 12 dbar captured by the Argo profilers, while the color of the dots indicate the month of the occurrence of a negative salinity gradient. In several regions a negative salinity gradient is found (Figure 4.9). The Bay of Bengal is known to be influenced by strong monsoon rainfall in late fall and winter, but also by river run-off in September. The eastern Pacific Fresh Pool (*Alory et al.*, 2012) is formed by strong precipitation at about 5 °N in November/December. The fresh salinity anomaly is advected across the equator near the Galapagos islands and shows up in March/ April at about 5 °S (see chapter 5).

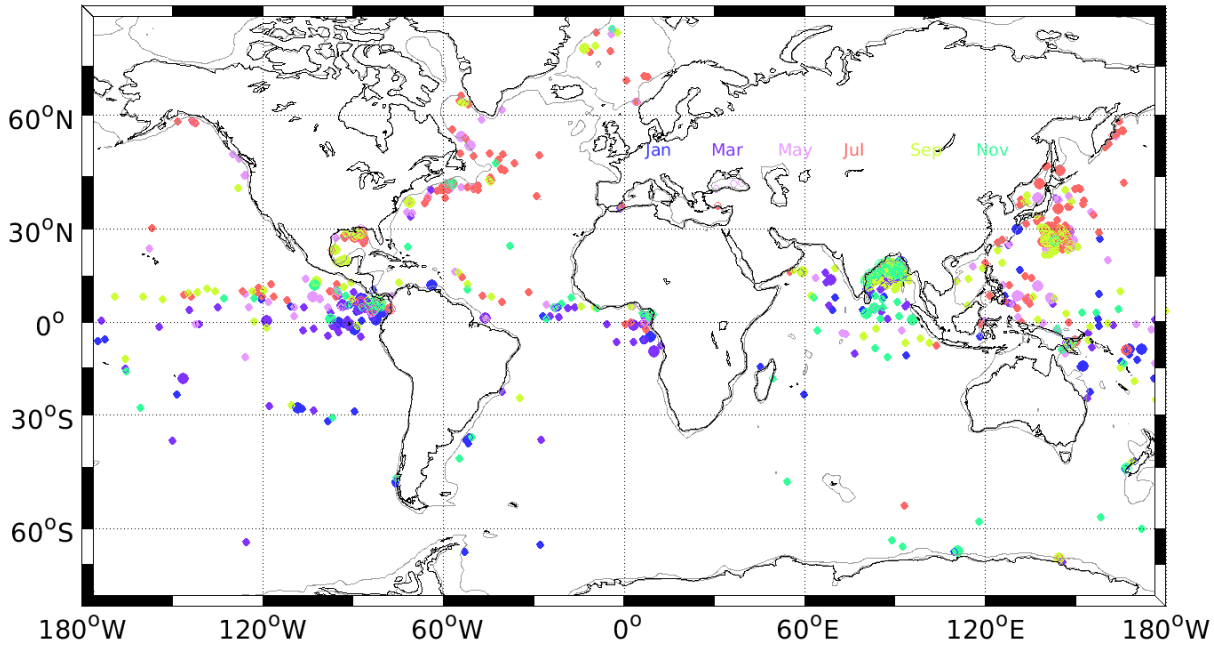

Figure 4.9.: Negative salinity gradients ($\frac{\partial S}{\partial z} < 0$) between 1 m and 12 m depth captured by Argo profilers in 2010 to 2014. Small and larger dots represent gradients <-0.1 m^{-1} and <-0.3 m^{-1}. The colors indicate the months of year in which the gradient was observed. In regions of frequent occurrences of negative salinity gradients, the dots superpose and the last dots drawn determine the color. See text for further explanations. The gray line shows the 1000 m water depth contour.

Negative vertical salinity gradients in the western boundary currents, along the paths of the North Atlantic Current and the Kuroshio are attributed to the strong salinity gradients sharpening in spring and summer, between May and September. The tropical Atlantic has negative salinity gradients at the river discharge of the Congo river, the Rio Plata, however, is not well represented by this illustration, because its water discharge is advected along the shelf, where no Argo profiler is measuring and no data are available. The Amazonas outflow is also underrepresented because the low salinity mixed layer which forms at its discharge region is deeper and thus also the salinity gradient is found deeper than the depth levels selected for the plot. Furthermore the Argo profilers are moved away from this region due to strong surface currents so that the data availability there is also scarce (compare Figure 4.1).

From all Argo profiles having at least 2 data above 12 dbar, only 1.06 % showed negative salinity gradients in the depth interval 1 to 12 dbar. The Argo profiler only by chance captures a transient precipitation event, even if it is a strong one and leading to a persistent layer of low salinity. The results shown in Figure 4.9 also do not account for still deeper vertical gradients, reflecting a deep mixed layer or an eventual barrier layer. Summarizing, and confirming the results of *Anderson and Riser* (2014), the Argo profilers mostly do not show strong negative gradients which may influence the validation of satellite derived salinity measurements by the Argo data. Only in regions of strong precipitation and river run-off the validation may be

hampered by strong vertical salinity gradients.

4.2.2. Functional relationship to geophysical parameters

In a general sense, we expect a bias to represent a systematic difference between different measurements of the same parameter, a difference which can be assessed by knowing the underlying processes or algorithms, so that one can reconstruct a correction function to subtract the reconstructed bias. In order to develop a correction function, the differences between the in situ and the satellite retrieved salinity data will be investigated here and dependencies on geophysical parameters will be searched for.

In this sense, the land contamination and latitudinal bias can be considered systematic errors, as they are related to the reconstruction of the image, i.e. it is an intrinsic deficiency in the measurements, and hence, a property of the instrument itself (*Anterrieu et al.*, 2015). The land contamination results in deficiencies in constructing the brightness temperature images when the transition from land to sea or vice versa is in the field of view (FOV). Whereas the presence of land in the FOV increases the directly measured brightness temperature of the image in a straight forward way, the case for the interferometric radiometer is more complex. The reconstruction of the brightness temperature field involves the correlation of the signals from all antenna pairs and thus the strong signal of land influences the whole FOV. The distortion of the image depends on the angle of the FOV to the coastline or the ice edge. The exact repeat cycle for the same angle encountered at the overflight of the coastline is 149 days, so there is a chance of finding the same pattern of land contamination twice a year, i.e. for 4 years, there are about 10 realizations. Within these orbits seasonal differences in SST and salinity would occur and other disturbing influences such as galactic noise, sunglint and other effects related to the geometric constellation of earth, sun and satellite will vary in the selected 10 half orbits as well. For these reasons, I haven't followed the idea to construct a land contamination correction based on about 10 realizations of a half orbit.

In the following, the space born salinity bias dependence on geophysical parameters will be analyzed.

Dependence on wind

To analyze the salinity bias in respect to a potential functional relationship to wind, SMOS data from the year 2013 with lowest and highest wind speeds were included in the comparison. The differences in salinity were grouped into wind classes of 2 m/s for the three different roughness models. In order to separate the influence of temperature and land contamination, the global data pairs were additionally selected when revealing a temperature $> 4\,^{\circ}\mathrm{C}$ and being measured far from the coasts, i.e. having a minimal distance of at least 600 km to any coast line. A summary of the results for the three roughness models is shown in Figure 4.10.

The salinity differences between satellite and in situ data are highest at wind speeds exceeding 10 m/s. Here, the roughness models S1 and S2 show a strong negative bias, with stronger and linearly decreasing bias in model S1. The empirical roughness model S3 in contrast shows positive bias at high wind speeds for data with and without (not shown) selection of the land contaminated or cold SST data. The mean differences between the roughness models

are similar to each other in the moderate wind speed interval 3-12 m/s, where the differences range between -0.5 and +0.3. While the model S3 seems to better simulate the roughness at wind speeds of 11-14 m/s, its performance at lower wind speeds is similar to the other models, which all show increased bias at lowest wind speed. The ascending half orbits seem to have a constant bias of -0.3 in comparison to the descending half orbits. The plot shows globally averaged values, which reflect also the compensation between negative and positive values in the descending half orbits, whereas the ascending orbits are mostly positive (see also Figure 4.3).

This figure illustrates well that the choice of excluding data outside the wind speed interval 3-12 m/s, as recommended by ESA based on the study of *Boutin et al.* (2013) for any L3 product is justified. The higher std is partly due to lower accuracy of ECMWF forecasts at low and high wind speeds (*Boutin et al.*, 2013).

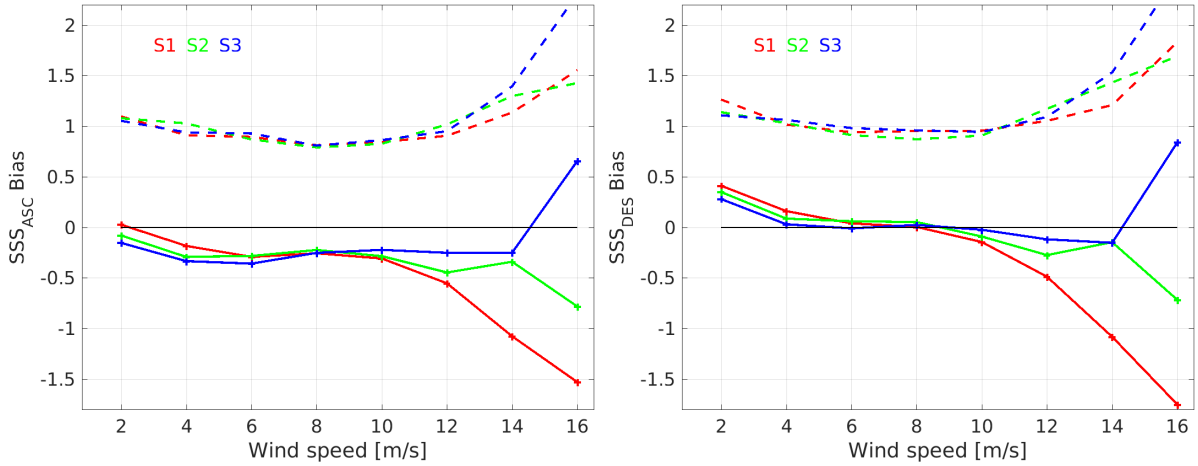

Figure 4.10.: Global salinity differences for all three roughness models, plotted against wind speed. Mean differences (standard deviations) are plotted with straight (dashed) lines for all 3 roughness models (S1 to S3) as indicated by colors for ascending (left) and descending orbits (right). The plot presents situations with SST>4 °C and with a distance from the coast of at least 600 km.

Dependence on distance to the coastline

One of the largest influence on the salinity bias in the vicinity to coasts is the so called land contamination, as explained in section 2.1.2. As can be seen in Figure 4.11 the bias near the coast is negative for both half orbits. Only seawards from about 600 km of the coast, the absolute bias values are less than 0.5. The standard deviation is plotted in Figure 4.11 as dashed lines multiplied by (-1). Its absolute value is at 1.5 which had been shown by the high RMS errors in Figure 4.18 around the coasts. The high variability of the bias is due to the different geometric constellations of the satellite direction relative to the course of the coastline.

The thin lines show the mean bias when excluding data with low temperature (<4 °C). These cold temperature data have a compensating positive effect on the bias for both orbits

and will be elucidated in more detail in the next section.

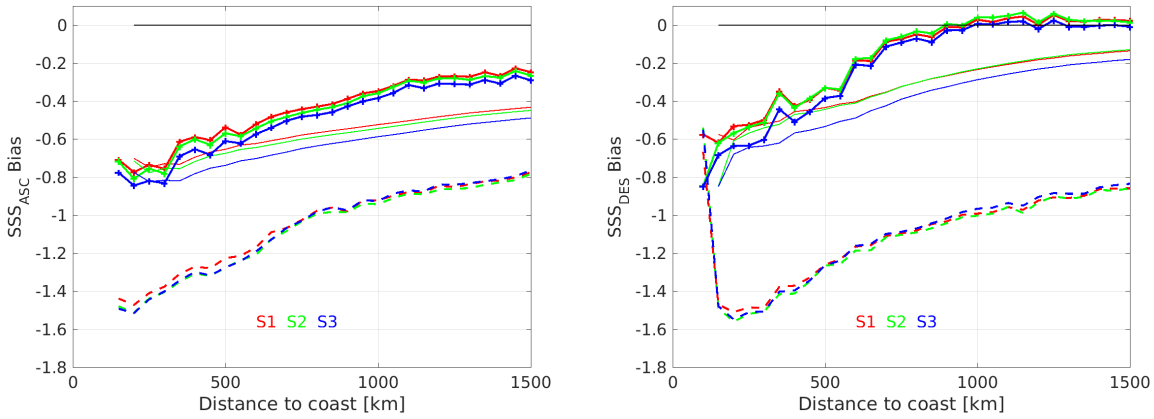

Figure 4.11.: Global salinity differences for all three roughness models, shown as function of their distance to coast. Mean differences (negative signed standard deviations) are plotted with thick (dashed) lines for all 3 roughness models as indicated by colors for ascending (left) and descending orbits (right). The thin lines show the results when excluding data with SST<4 °C.

Dependence on SST

The dependence on temperature, and especially the low sensitivity of the brightness temperature to salinity at low temperatures (0.25 K per at 0 °C *Lagerloef et al.*, 1995) was a matter of concern since the beginning of the SMOS mission development (*Font et al.*, 2010). For producing Figure 4.12, showing the SST dependence of the global SMOS salinity bias, the effects of wind speed dependency and of land contamination were excluded by choosing only data pairs in the moderate wind speed range and with a distance of more than 600 km to the coast. The selection diminishes the number of data pairs, and reduces the averaged bias for both half orbits by about 0.1–0.15. Figure 4.12 confirms that the higher the temperature, the better the salinity retrieval, which can be deduced by the decreasing std of the bias at moderate to high temperatures. In the ascending half orbits, the bias ranges between -0.2 and -0.4 for all models at SST > 10 °C, whereas in the descending orbits the temperature bias is slightly positive between 15 °C to 25 °C. At highest temperatures the retrieval seems to deteriorate again showing a stronger negative bias in both half orbits for all models and a higher std. However, the warmest SST occurrences are found near the western tropical areas and in the vicinity of coasts, i.e. also catches frequented shipping lines, where RFI may influence these data additionally. While measurements at SST > 5 °C show a small bias, and measurements at SST > 15 °C a std of the bias of < 1. The bias turns strongly positive at SST < 4 °C for all roughness models and the std of the salinity differences rise to 1.3. When including data pairs with higher wind speed and closer to the coasts (not shown) the bias decreases again by 0.1 to 0.15. I note, that the temperature dependence at T<10 °C is different for the three roughness models. If this has to do with the roughness models themselves or if it is another

influence is not yet clear. Taking SST in the roughness model into account, which usually is not done, may induce differences in retrieved SSS on the order of 0.5 (see Figure 7 of *Dinnat et al.*, 2003). However, the interpretation of this different response is difficult considering the high uncertainty of the results.

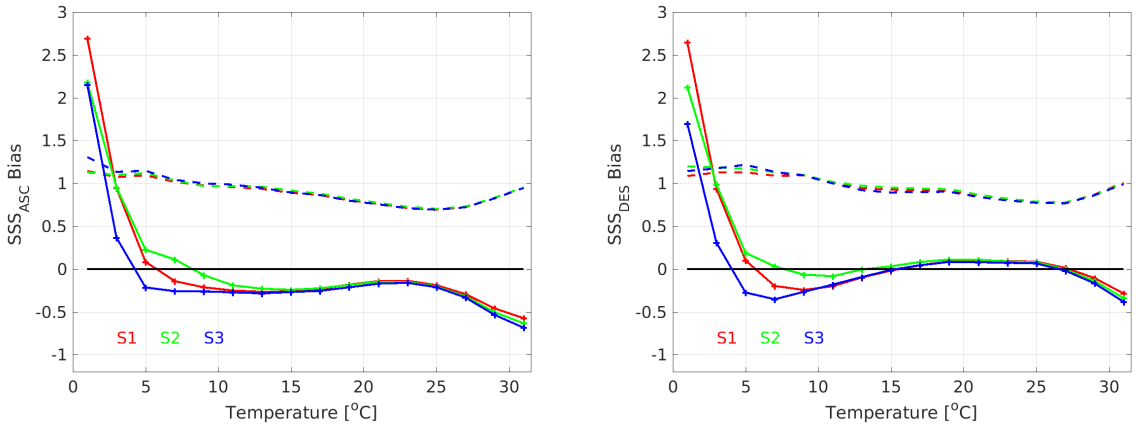

Figure 4.12.: Salinity differences in sea surface temperature classes of 2 °C. Mean differences (standard deviations) are plotted with solid (dashed) lines for all 3 roughness models as indicated by colors for ascending (left) and descending orbits (right). The plots represent data observed at moderate wind speed (4 m/s>wind speed >10 m/s) and with a distance to coast of at least 600 km.

The feature of a positive temperature dependent bias is a contradiction to the results derived from gridded monthly products in *Köhler et al.* (2015) who presented a negative temperature dependent bias and deserves further inspection.

The coldest temperatures (SST < 4 °C) found in the data set of collocations between in situ data and L2 half orbits, occur in the high latitudes as shown in Figure 4.13. Most (80 %) data pairs are located around the Antarctic continent, along the Polar Front at latitudes of about 50 °S to 60 °S. This front is characterized by a strong decrease in SST from about 5 °C to <2 °C (*Dong et al.*, 2006). In the northern hemisphere low SST is found in the northwestern Pacific and Atlantic Oceans, they were captured by the Argo instruments notably within the Labrador Sea and at some locations in the Greenland and Barents Sea. The positive bias in the Figure 4.3 seems to be related to the low temperature as already pointed out above. On the other hand, *Boutin et al.* (2013) assumed that the positive bias in the extreme southern latitudes were related to high wind speeds. This assumption cannot be confirmed here because the occurrences of high wind speeds in the SMOS L2 and in situ data collocations are not included in this latitudinal band.

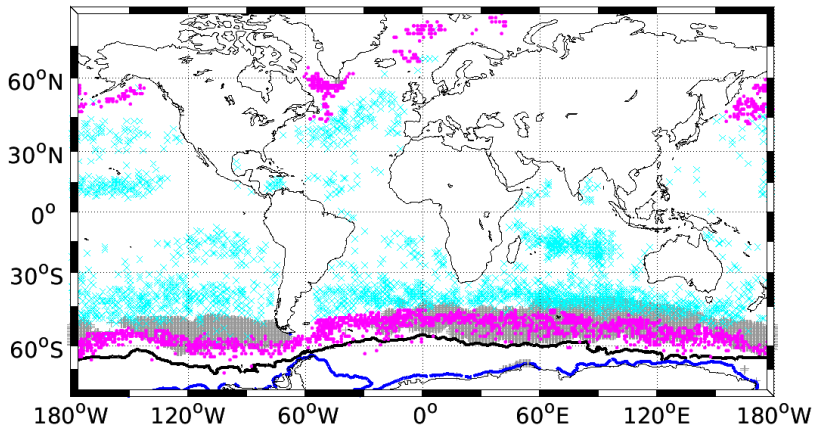

Figure 4.13.: Measurement locations where SST <4 °C (magenta), and where SMOS L2 wind speed > 11 ms (cyan crosses). The ice edge in March (September) is indicated by the blue (black) thick line around the Antarctic . Locations where wind speeds > 11 m/s from the monthly averaged Multi satellite data set (HOAPS) are marked in grey.

Also shown in Figure 4.13 are the locations, where SMOS L2 single values of retrieved wind speeds exceed 11 m/s. For comparison the locations are shown where the gridded multi-satellite wind data set (HOAPS) from a yearly mean indicates high wind speeds. These averaged values show the true high wind speed belt around the Antarctic. The locations of high wind speeds in the SMOS L2 data are mostly equatorwards of the indicated band of the true high wind speeds and low temperatures and is not well represented by the data of collocations. Moreover, high wind speeds should cause a negative bias for the roughness models S1 and S2, as shown in Figure 4.10. A detailed validation of the satellite derived salinity with L2 in situ data is thus hampered by the lack of in situ data in the latitudes of these rough weather conditions and due to the SMOS data quality.

In order to separate again the dependency on SST and wind speed, the data pairs resulting from the roughness model S3 are plotted in Figure 4.14. For this roughness model the SMOS data are not discarded due to quality reasons by the retrieval, and more data at high wind speeds are available than for the other 2 roughness models. Figure 4.14 shows, that the bias is negative at high winds speeds, but turns positive at high wind speeds and low temperature. If this is due to the roughness model alone or if other influences or parametrizations play a role cannot be resolved here.

However, the a priori data for wind speed from ECMWF underrepresent the wind speeds compared to the ones measured by QuickSCAT and later ASCAT scatterometer in the southern latitudes. *Yin et al.* (2013) used SSM/I winds for retrieving salinity within the SMOS forward model, but could not explain the positive salinity bias in the southern ocean due to the use of ECMWF winds. Another explanation, a point raised by *Ballabrera* (2015), is a degradation of the salinity in cases when the SST used by the SMOS salinity retrieval as a priori data (also from the ECMWF forecast) is different from the actual in situ temperature. The temperature differences between the Argo single profiler data and the SMOS SST were used to check, if a

negative SST difference would lead to a negative bias in salinity or vice versa. But no systematic relation could be found.

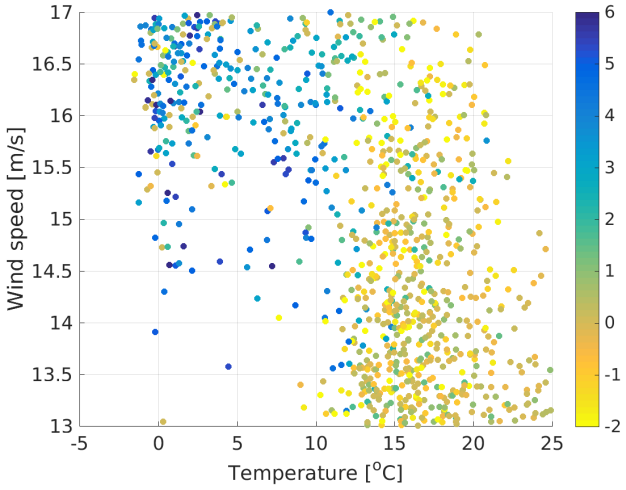

Figure 4.14.: Differences in salinity between L2 SSS S3 (descending half orbits) to in situ data for the year 2013 (color), at their respective SST and wind speed. Here data pairs are excluded having a distance too close to any coast (600 km).

Like the presence of land in the FOV can contaminate the brightness temperature field, the transition to ice has the same disturbing effect. In order to check the possibility of the ice edge contamination, its location is calculated from the SMOS data itself. The increase in brightness temperature of the SMOS data itself, $(T_{Bv} + T_{Bh})/2$ from 90 °to 120 °K, indicates the presence of ice. This gridded data set was made available by *Tian-Kunze et al.* (2014). The T_B contours of 100 °K in Figure 4.13 indicates the averaged position of the ice edge in March and September. Especially in September the ice edge is very near to the cold bias found in the collocations. However, the ice edge contamination of the SMOS data should result in a negative bias and should show a different response for descending and ascending orbits which is not the case.

Summarizing, the positive salinity bias is mostly independent of the wind speed, not caused by the ice edge contamination, no severe galactic noise is found in the retrievals with the positive bias (not shown), nor RFI. So, the results so far lead to the only explanation, that the model of the dielectric constant from *Klein and Swift* (1977) which is used to compute the Fresnel emissivity of the sea surface (see section 2.1.2) might be responsible for the positive bias at cold temperatures.

Dinnat et al. (2014) compared the effects of the different models for the dielectric constant used in SMOS and the one used in Aquarius which was developed by *Meissner and Wentz* (2004) and updated in *Meissner and Wentz* (2012). The effect of the differences between the 2 dielectric constant models reveals a very strong dependency of the brightness temperature on SST below 5 °C (their Figure 2). Computing the salinity from the brightness temperatures measured by Aquarius with the dielectric constant model from *Klein and Swift* (1977) also

lead to a positive bias at very low temperature (SST $< 4\,^{\circ}$C) in comparison to single Argo profile data (*Dinnat et al.*, 2014, their Figure 3). The latter authors used a time limited data set from Aquarius, and revealed a high variability within the low temperature data pairs, however, the results based on collocated data pairs in the present study confirm the idea of *Dinnat et al.* (2014). Whereas at moderate temperatures the dielectric model of *Klein and Swift* (1977) performs better than the model of *Meissner and Wentz* (2012) it shows a degradation of salinity at very low temperatures (*Le Vine et al.*, 2015). A recent study by *Lang et al.* (2016) shows an underestimation of the dielectric constant by *Klein and Swift* (1977) at low temperatures by 1 to 1.5 %, so that a revision of the model seems to be necessary for this temperature range.

The analysis of the bias at this low SST is difficult due to the lower sensitivity of the T_B to SSS (<0.25 K per salinity unit at SST $< 5\,^{\circ}$C) so that a degradation of the retrieval performance is expected. This is also not compensated for by the higher sampling at high latitudes due to the superposition of the half orbits (*Sabia et al.*, 2014). The std of the bias in Figure 4.12 shows that the uncertainty is quite high. Furthermore, the sampling error of the Argo data is assumed to be high because of the strong eddy activity in the Polar Front and subsequent high hydrographic variability.

An advantage of validating L3 products is the reduced noise in the SMOS data and the regular data sets. On the other hand, the problem validating monthly gridded satellite salinity with monthly gridded or objectively mapped data is evident in the study of *Köhler et al.* (2015). That study used the L4 BEC data (*SMOS–BEC Team*, 2014) for satellite derived salinity and the uppermost quality checked data of single Argo profiles for comparison to in situ salinity which were objectively mapped to monthly fields. The data hardly covered the really cold areas of the North Atlantic and had to be extrapolated north of 60 °N. The spatial scales of averaging in the L4 BEC product are not well known, however, the dependencies of the salinity bias on temperature, on latitude and on land contamination are mixed due to the use of averaged and extrapolated fields, an analysis such as done in the present study is hardly possible on the L3 level.

Dependence on Latitude

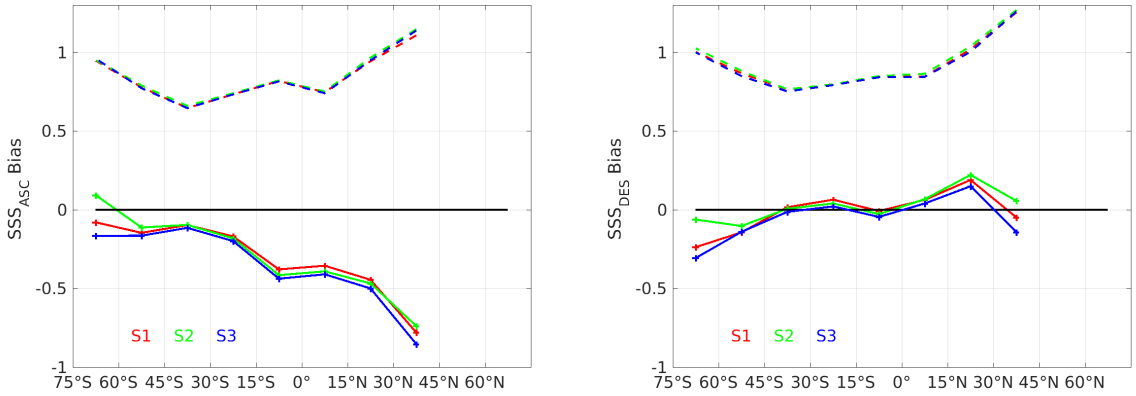

Figure 4.15.: Salinity difference as computed in Figures 4.10 to 4.12. Mean differences (standard deviations, STD) for latitude intervals (15^o) are plotted with straight (dashed) lines for all 3 roughness models as indicated by colors for ascending (left) and descending orbits (right). The plots represent data measured at moderate wind speed, at temperature $> 4\,°C$ and with a distance to the coast of at least 600 km.

Looking at the distributions of the salinity bias along latitude, the positive bias around the extreme southern latitudes seem to cancel out when averaging over time and longitude, a sorting of the differences relative to latitudes presented in Figure 4.15 do not show the positive bias around 50 °S. The land contamination, which is the main effect north of 40 °N, influences the data only partly, because the data are limited to distances $>$ 600 km from the coast. When including data nearer to the coast and with lower temperature the positive bias in the northern latitudes is averaged out and north of 60 °N the negative bias is weakened again by the influence of the temperature induced positive bias (not shown). In the northern Atlantic both half orbits show strong negative disturbances due to land contamination. Moreover, there may be more undetected RFI in the northern hemisphere (Atlantic and East Asia), which also effect the quality of the SMOS SSS. A general latitudinal decrease of the bias with latitude seems to exist for the ascending orbits, and a linear increase of the bias for the descending half orbits. A negative offset is seen for the ascending half orbits on the Figures 4.10, 4.12 and 4.15, also evident in Table 4.2. Further retrieval deficiencies with seasonally varying strength originate from the sunglint, which is the reflection of the solar emission on the sea surface. The sun is a strong emitter at L-Band and the effects are corrected in the salinity retrieval (see chapter 2.1.2). However, the models to calculate its influence are not perfect and the seasonal and latitudinal variation of the sun glint impact are described in *Khazâal et al.* (2016). After these authors, incorporating the surface roughness information into the sunglint correction is essential for an optimal correction; this would also have an improving impact on the retrieval method of the Faraday rotation (*Vergely et al.*, 2014).

4.2.3. Annual component of the L2 SMOS salinity bias

Efforts to discern the differences into dependencies on wind or temperature were shown to be difficult because the random noise is too high for all parameters at the L2 level, though the data were already averaged spatially. A functional relationship is furthermore difficult to develop because the data availability of the collocation pairs is small.

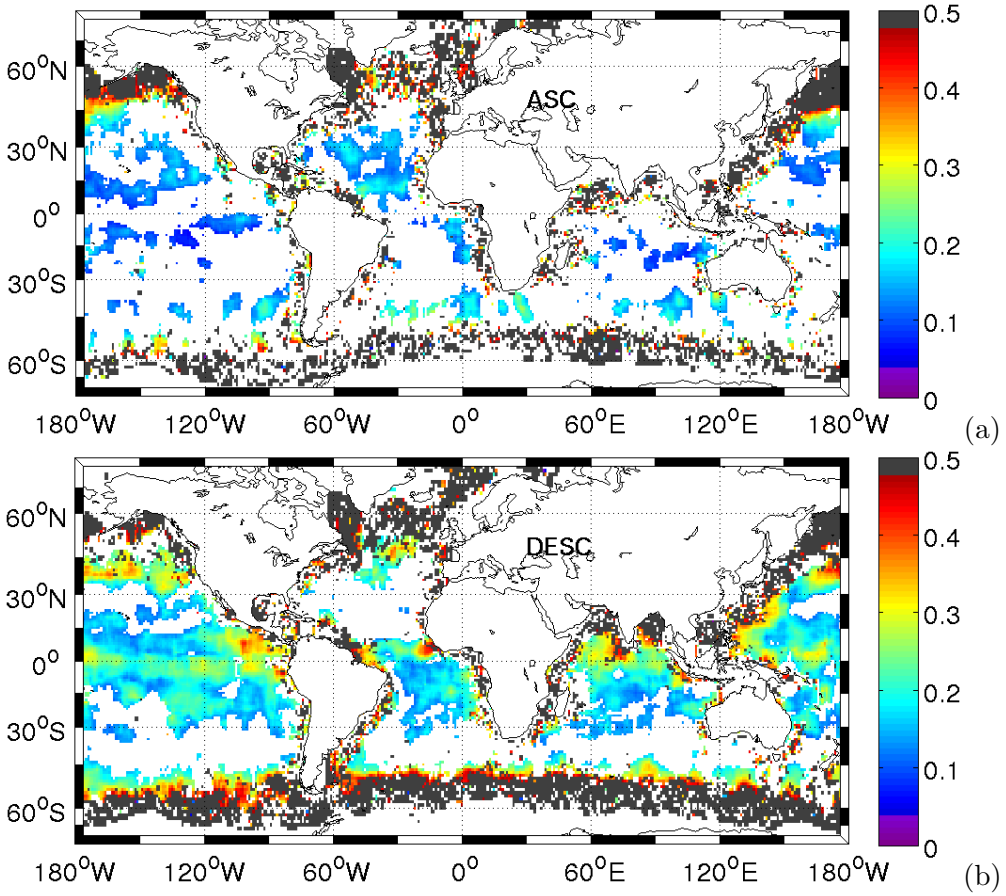

Figure 4.16.: Annual amplitude of the salinity differences between SMOS L2 half orbit and in situ data, for ascending (upper panel) and descending half orbits (lower panel). In white areas there are no data pairs, the results were not significant, or they do not explain more than 10% of the total variance.

In order to derive a systematic approach for the bias correction, the annual amplitude of the differences are computed (Figure 4.16). The motivation for doing this is based on the assumption, that a lot of deficiencies in the salinity retrieval reveal an annual cycle, as e.g. galactic noise with a maximum in September in the southern hemisphere, the sun glint occurring during specific months within the northern or southern hemisphere, or the land contamination (*Tenerelli et al.*, 2008). The latter should only depend on the angle between the land contours and the flight direction of the satellite. Though the exact repetition time for the

track of the satellite is 149 days, there may be some common patterns in the bias distribution repeating during the year. The scene including terrestrial parts in the FOV received by the antenna varies with the solar angle which has an annual cycle.

Figure 4.16 shows the amplitude of an annual cycle fitted to the 5 year time series of the salinity differences between the satellite retrieved data of each half orbit and the in situ data in each grid box of $1\,^{\circ} \times 1\,^{\circ}$. Only significant results are shown where they explain at least 10 % of the total variance. The results are not covering the areas around the coasts completely, because of the sparsity in the Argo data. However, the annual amplitude is high around the coasts, so that I assume, that they reveal an annual cycle. Besides the continental margins and high latitudes, the annual amplitude of the bias is very small in the open ocean, especially for the ascending orbits only some tropical regions reveal an annual variation of the bias. These may be explained by precipitation regions varying annually in position and amount of precipitation. The descending orbits show a mean bias near to zero in the open ocean, but in contrast to the ascending orbits a wider spread annual signal with higher amplitudes in the higher latitudes.

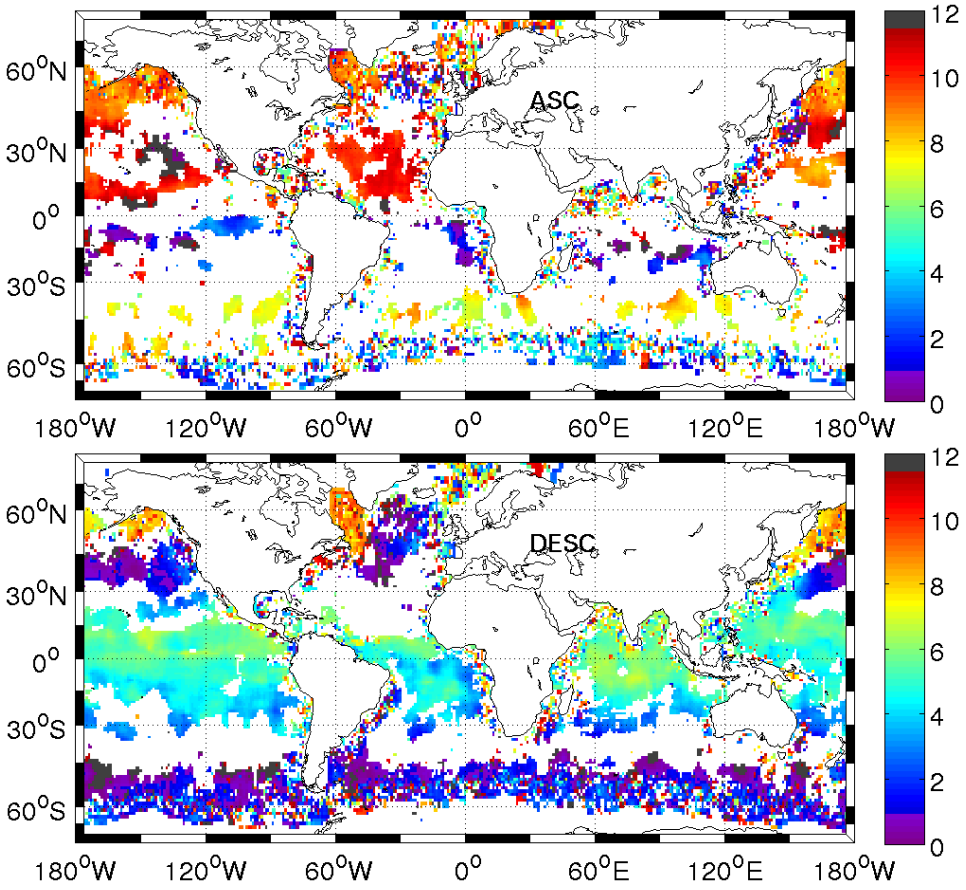

Figure 4.17.: Phase of the annual amplitude shown in Figure 4.16, for ascending (upper panel) and descending half orbits (lower panel). In white areas there are no data pairs, or the results were not significant.

The phase of the annual cycle is shown in Figure 4.17. No oceanographic meaning can be deduced from the amplitude and phase of the fitted annual cycle first because the descending and ascending amplitude and phase are contradicting, and second because a relation to stronger evaporation, or stronger precipitation cannot be found. So in the interior of the ocean, the information from the annual cycle cannot be used. The differences in the ascending and descending half orbits are more likely to be due to imperfect corrections in the processor (e.g. *Tenerelli et al.*, 2008; *Khazâal et al.*, 2016, for galactic glint and sun glint). However, the results show again, that a bias correction must be carried out for the half orbits separately.

4.3. Correction of SMOS L2 salinity

A functional relationship in the differences between satellite and in situ data could not be established. The geophysical parameters such as wind and temperature mix in their effects on the salinity retrieval. An annual cycle of the bias in the quasi L2 data could only be found regionally. Therefore, an empirical correction will be pursued. The correction on the L2 level has the advantage to have the closest collocations in space and time, so that the in situ data suffer less from the sampling error within the collocation interval of 1 week and 1 °in latitude and longitude. Within one month it can reach high values near the coasts when there is a river discharge and may reach 0.2 in the the open ocean, as described in chapter 3. In order to correct for the bias at the L2 level, the following problem has to be overcome: The in situ measurements are sufficiently accurate but very sparse. In order to lean on salinity values as exact as possible with which the SMOS SSS can be corrected for, one has to average the collocations of in situ and satellite measurement in time and space. A first step for constructing a bias correction matrix on the L2 level, is the gridding to a weekly matrix of collocations. One week is the time period for the global coverage of the L2 SMOS data for one type of half orbit.

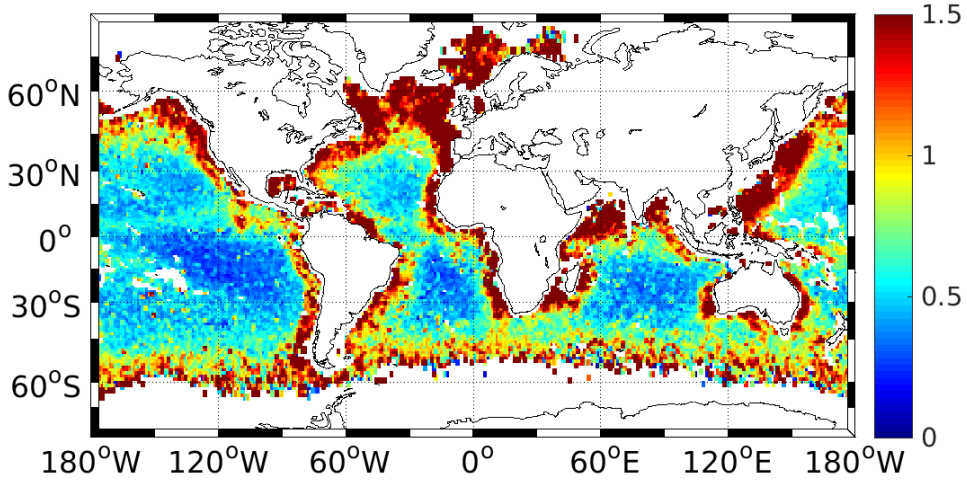

Figure 4.18.: Root mean squared salinity differences between monthly SMOS L2 ascending half orbits and gridded in situ data during the period February 2010 to December 2014.

Root mean squared differences of this weekly bias matrix are shown in Figure 4.18, exemplary for the ascending half orbits in model S1. The distributions for descending half orbits and for other roughness models are very similar. They reveal a high variability of the differences near the coasts, in the North Atlantic, southeast of Asia, and around the Antarctic.

The differences were then averaged for one month centered on the week of the differences and on a $7\,^{\circ}\times\ 7\,^{\circ}$area, weighted by the distance to the central grid point, presuming that the bias resulting from the retrieval has large scales and furthermore to maintain the small-scale variability within the SMOS SSS measurements. Exceptions are areas where the RMS difference amounts to > 1.1, an arbitrarily chosen limit, which encompasses the large bias around the continents and in high latitudes (see Figure 4.18). In these areas the bias is calculated from the monthly mean bias in a box encompassing the box itself and the eight surrounding boxes with a small-range spatial averaging in order not to contaminate the open ocean fields. The applied spatial averaging still contains outliers and a temporal smoothing is applied to the time series of the bias correction for each box. The existence of an annual cycle around the coasts (Figure 4.16) justifies that the bias is set to a mean monthly value from the 5 years available if not enough data in the respective month are available for computing a monthly spatial average.

Finally, the bias corrected salinity at the quasi L2 level is calculated by subtracting the weekly bias matrixes DS_{insitu} for the different half orbits (orb) descending and ascending from the biased SMOS SSS retrieval:

$$SSS_{\,biascorrected,orb} = SSS_{\,biased,orb} - DS_{\,insitu,orb} \tag{4.1}$$

The error $DSerr$ in correcting the L2 values is the theoretical error of the SMOS SSS retrieval in the $1\,^{\circ}\times\ 1\,^{\circ}$fields err_t plus the squared differences between SMOS L2 and the in situ values found in the same grid box within $\pm$ 3 days, thus during 7 days divided by $N(N-1)$, N being the number of valid collocations:

$$DSerr = \sqrt{\frac{\sum DS^2}{N(N-1)} + \frac{\sum err_t^2}{N}} \tag{4.2}$$

The time mean total error of these estimates in the grid boxes is shown in Figure 4.19. The spatial distribution naturally resembles the RMS salinity differences in Figure 4.18.

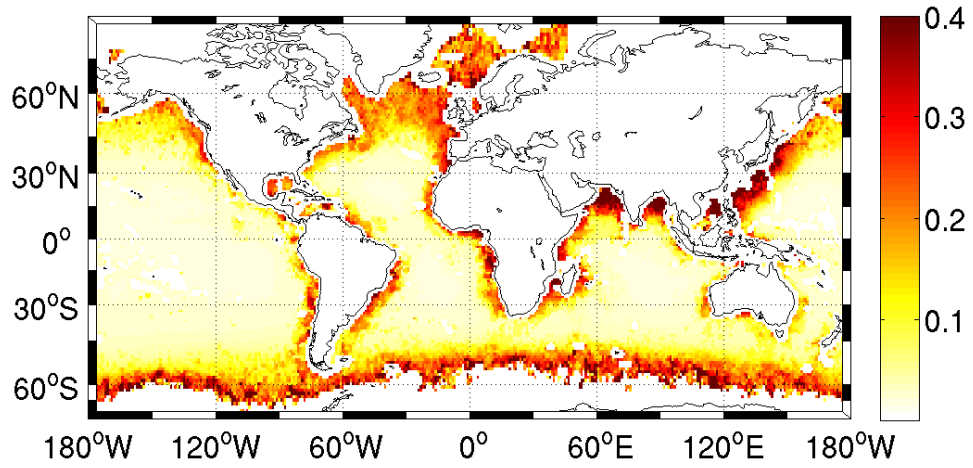

Figure 4.19.: Mean total uncertainty of the bias calculated for the SMOS L2 ascending half orbits (roughness model S1) during the period February 2010 to December 2014.

4.3.1. Validation of the bias-corrected product

The bias correction is carried out on the L2 level, however, for the production of the subsequent monthly averaged L3 salinity fields advantage is taken from the additional error information gained during the L2 bias correction. The inverse error is used to weight the corrected data for the monthly average based on the ascending and the descending half orbits. So, for checking the improvement by the correction process undertaken here, the comparison is done on the L3 level. I compare in the following the SMOS L3 fields with and without bias correction to the EN4OBJ salinity fields. Figures 4.20 and 4.21 show the bias during the seasons.

In Figure 4.20 the different bias of the ascending or descending orbits occasionally compensate. The Figure illustrates again the band of positive bias in the southern ocean varying during the seasons with the position of the thermal Polar Front. In January to March, a positive bias is also evident in the Labrador Sea, the rest of the North Atlantic shows a negative bias in salinity due to land contamination and RFI. The land contamination around the continents is most evident in these bias fields. The largest negative bias is found during October to December, when ascending and descending half orbits both show a negative bias. Some patterns of the negative bias have a natural origin, e.g. bands of rain in the Intertropical Convergence Zone (ITCZ) which reveal a seasonal cycle with highest precipitation rates in the boreal summer months, or the river discharge of the Amazon in the tropical Atlantic which is advected northeastward, evident in April to June.

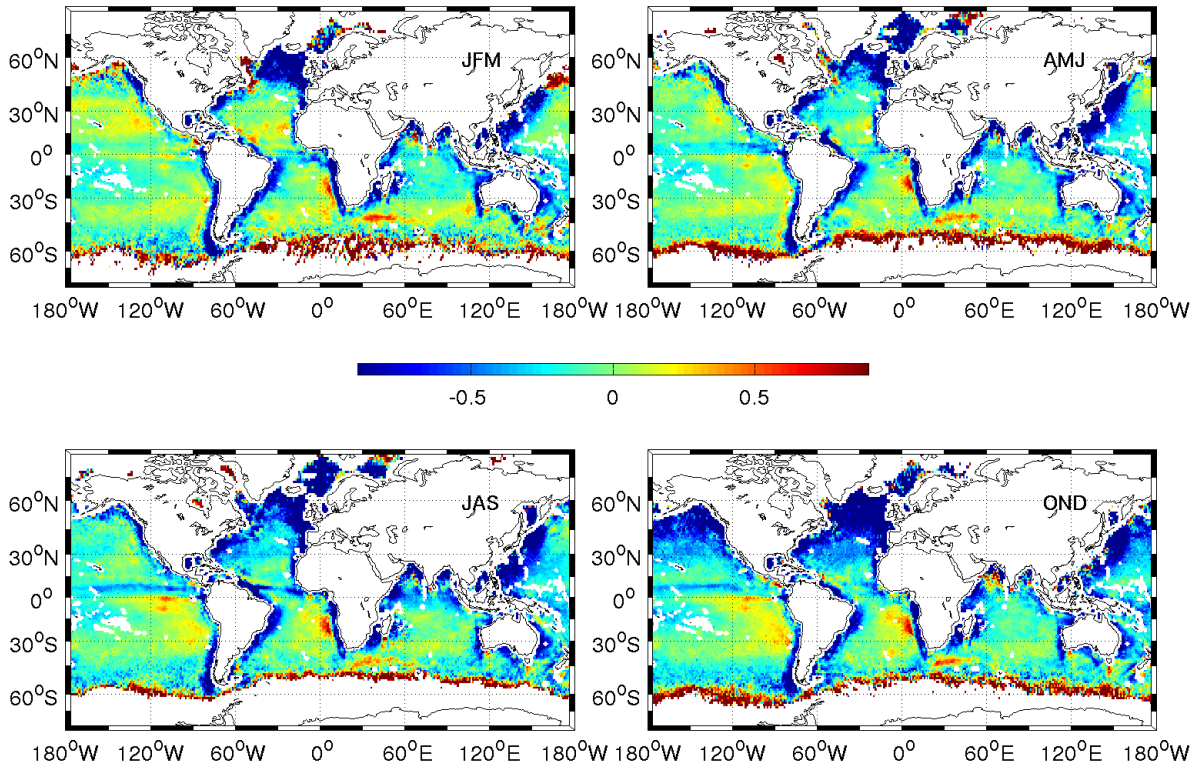

Figure 4.20.: Seasonally averaged salinity differences from uncorrected SMOS minus EN4 objectively mapped monthly fields in January to March (JFM), April to June (AMJ), July to September (JAS) and October to December (OND). The colorbar in the middle of the panels is valid for all panels.

The bias correction (Figure 4.21) is effective in the regions of extreme negative bias, namely around the continents and in the northern latitudes. Extreme difference values are attenuated in the open ocean where the prevailing color is green, i.e. reflects a difference near zero. The correction is not very effective in the southern ocean in correcting the positive bias. The data availability in these areas is poor, the small number of collocation increases the statistical uncertainty and decreases the weighting factor of the corrected salinity values in the monthly average.

Moreover, there are some regions where the correction is even degrading the salinity, e.g. west of the southern tip of South America, west of South Africa and also west of Australia. These are shadows of land contamination in the ascending orbits extending into the open ocean so that the spatial averaging of the bias matrix overcorrects. There are still some zonal bands of negative bias in the tropics, regionally related to the precipitation, and a region of negative

bias along the north of Brazil which reflects the river discharge of the Amazon, i.e. the spatial filtering of 7 °× 7 °is large enough to maintain these patterns of natural salinity differences. A little puzzling is the slightly positive bias (0.2) along 30 °S to 40 °S which is not corrected. This may be also an artifact of the EN4OBJ salinity fields.

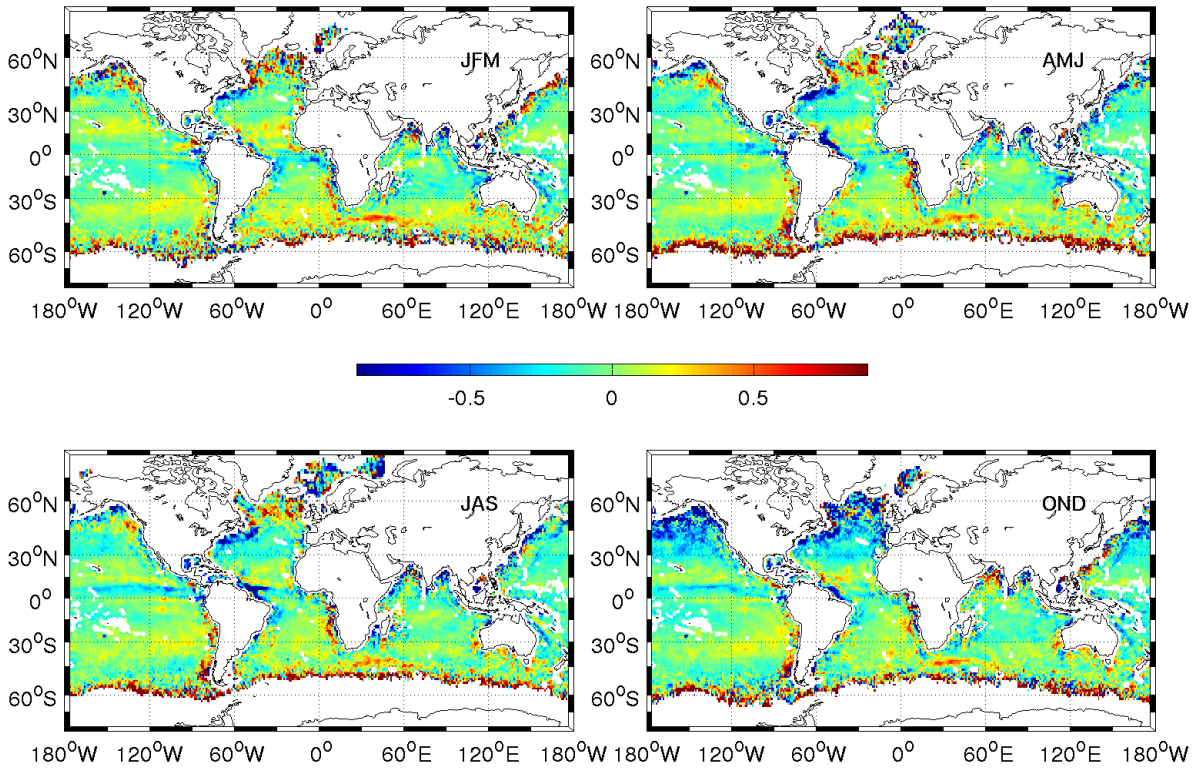

Figure 4.21.: Seasonally averaged salinity differences from bias-corrected SMOS minus EN4 objectively analyzed monthly fields in January to March (JFM), April to June (AMJ), July to September (JAS) and October to December (OND). The colorbar in the middle of the panels is valid for all panels.

Summarizing, Figure 4.22 shows the globally and temporally averaged root mean square differences of the uncorrected and bias corrected SMOS SSS minus the EN4OBJ fields. The global mean bias was effectively reduced from -0.22 to -0.04 on large scale, and the RMS differences were slightly reduced from 0.74 to 0.62. In the latitudinal band between 40 °S to 40 °N the mean bias reduction with this correction method is similar (from -0.21 to -0.06) and the RMS differences reduce from 0.62 to 0.48 . A better filtering is still required, and a better mapping instead of a simple averaging can help to reduce the noise. The bias correction near to

land is based on monthly mean in situ data, however, the sampling error near to coast is large, a fact also considered in the construction of the objectively analyzed fields in the reference data set. Figure 4.23 shows the averaged estimated error of the EN4OBJ maps, which reveal higher errors especially around the coast than in Figure 4.19.

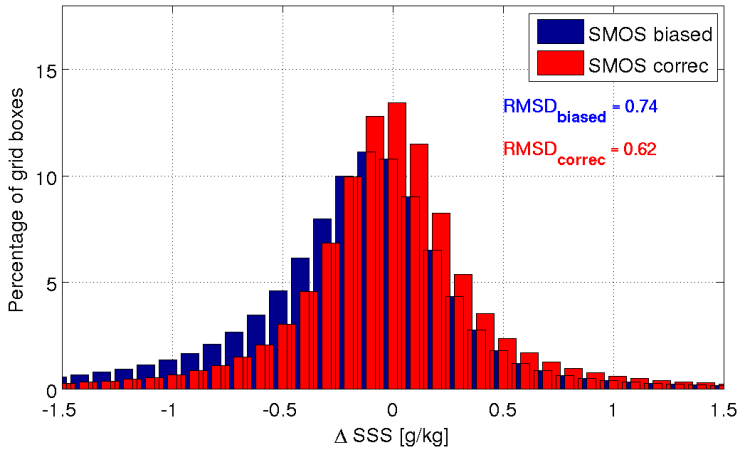

Figure 4.22.: Histograms of global RMS salinity differences between uncorrected (blue) and bias corrected (red) SMOS to EN4 objectively mapped monthly fields in the period 2010 to 2014.

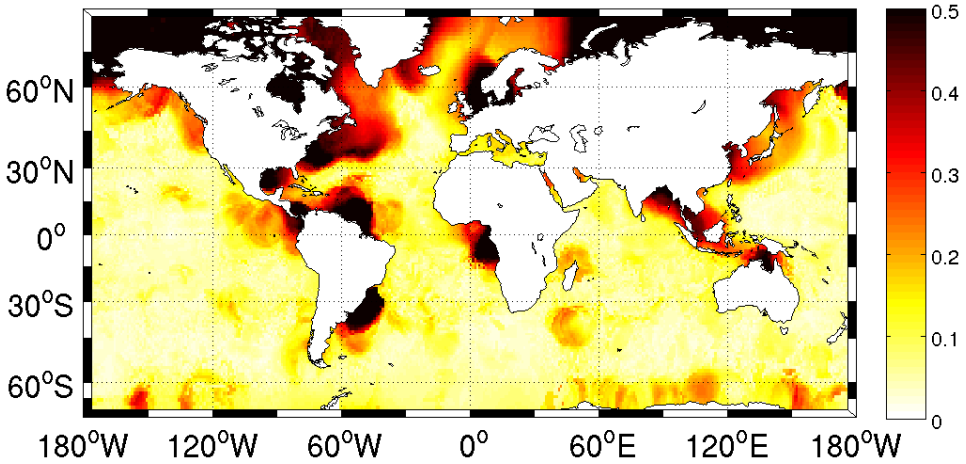

Figure 4.23.: Uncertainty of the monthly objectively analyzed surface salinity fields from EN4 (*Good et al.*, 2013), averaged for 2010 to 2014.

4.3.2. Comparison to drifter salinity observation

The most thorough validation of satellite derived salinity is performed by comparing these data to the salinity measured directly at the sea surface. However, measuring the salinity at

the ocean's surface is a challenging task, as bio-fouling, pollutants and wave induced bubbles influence the measurement within a conductivity cell. Moreover, the conductivity cell near the surface is subject to strong particle motions during heavy sea state, so that the flushing of the conductivity cell is faster than presumed in calm weather conditions. This distorts the alignment of conductivity with temperature in order to calculate the accurate salinity. Usually, the in situ measuring devices on ships - underway and on station - and from the Argo buoys are prevented from measuring in the upper few meters due to these complications. New devices have been developed for high resolution measurement near to or at the surface following the movements by the waves, but not yet implemented in the global network, and they still do not measure directly at the surface but at a few centimeters depth (*Anderson and Riser*, 2014).

The SVP (Surface Velocity Project, see chapter 2.2) surface drifters' salinity used in the present study is used for SMOS validation only in the southern tropical Pacific. During the time period of active surface drifters in the North Atlantic, the SMOS data had to be discarded due to RFI. A strong RFI source was active west of Greenland and affected the SMOS measurements in the northern hemisphere down to 40 °N. So no validation of SMOS data with the SVP drifters' salinity can be carried out in the North Atlantic. However, the data from the 10 SVP drifters launched in the southern tropical Pacific in March 2010 as described in chapter 2.2 are available for the validation in the respective area. The data were gridded to daily mean values with a 1 °× 1 °resolution. The standard deviation within one month of the gridded drifters' data set was used to estimate the salinity variability in the area. As the drifters provide Lagrangian data, the creation of an Eulerian data field is not trivial. I approximate the Eulerian daily fields by averaging the data during the respective day on a grid of 1 °resolution. This method will over-represent slow-moving drifters in the statistics and underestimate the ones drifting rapidly through the grid cell (e.g. *Jakobsen et al.*, 2003). Moreover, the standard deviation in the gridded data set depends also on the number of data per month, which is small (< 10) in 55 % of the grid boxes. Most of the grid boxes (89 %) show a std of salinity of < 0.1 during one month. This is somehow contradictory to the results presented above in the validation of the drifter salinity data by TSG and Argo data. The TSG section data as well as the drifter data during the collocation period showed a RMS difference of 0.13, the collocation with Argo data a RMS difference of 0.15. The underestimation of the standard deviation within one month is due to the Lagrangian characteristics of the drifters' data.

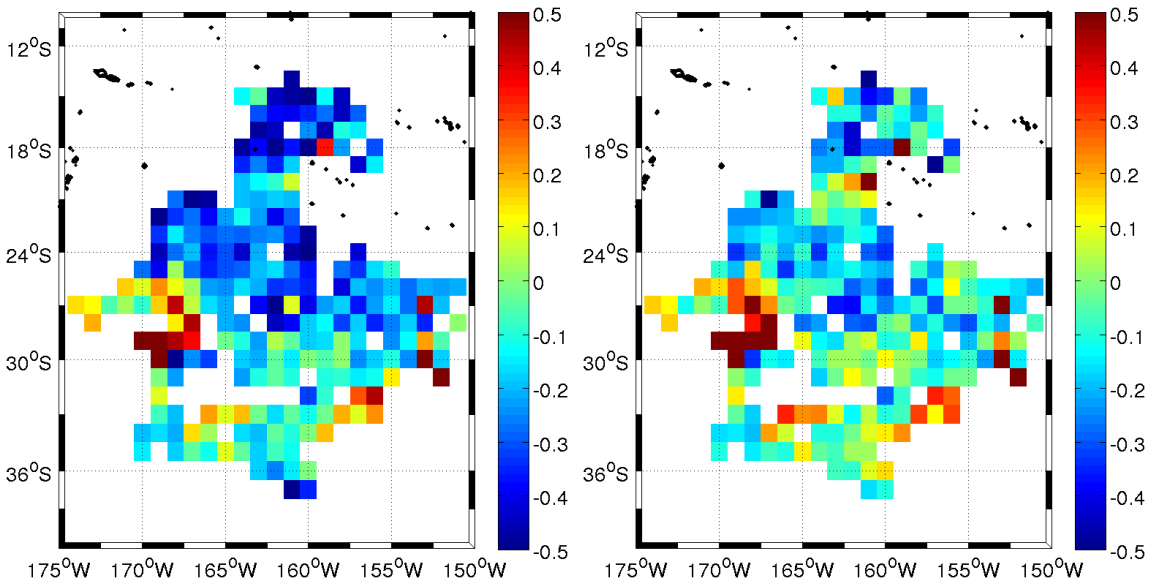

Figure 4.24.: Mean salinity differences between monthly SMOS L3 and gridded drifters' data during the period March 2010 to December 2011, for the uncorrected SMOS SSS fields (left) and the bias-corrected fields (right). Note the black dots in the figure representing islands.

The mean RMS difference between the single SMOS L2 half orbits and the drifters' daily mean salinity amounts to 0.78 (not shown). The noise of these differences is very high, due to the uncertainties in the SMOS salinity retrieval. The retrieval is hampered by the land contamination in this region because of the numerous islands in the field of view. Therefore, statistically more confident SMOS salinity were taken in order to investigate the regional outcome of the bias-corrected product.

For this purpose, the gridded drifters' salinities were compared to the monthly SMOS SSS fields, which were linearly interpolated to the respective day of the drifters' data (Figure 4.24). The mean differences show negative values in the area where the land contamination due to the islands influence the salinity retrieval of SMOS. This pattern hardly vanishes with the bias-corrected version of the SMOS salinity (right panel of Figure 4.24), since the correction is done empirically with the in situ data available. The Argo data in this area are sparse, and therefore the correction is not fully satisfactory. However, the mean bias is shifted towards zero by the correction (Figure 4.25).

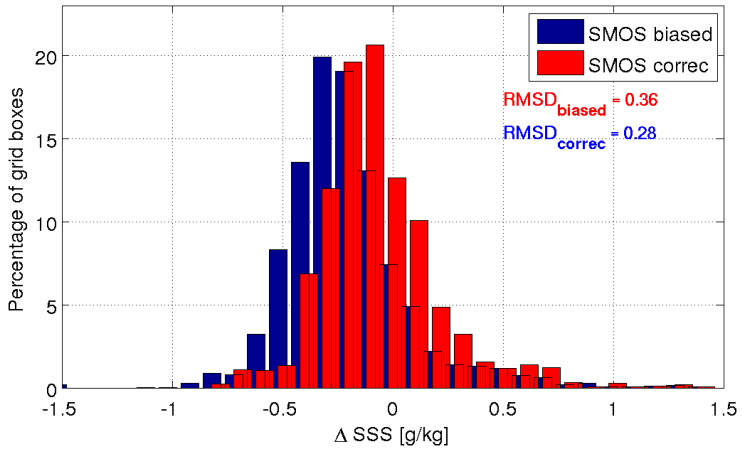

Figure 4.25.: Histogram of the salinity differences between monthly biased L3 SMOS fields (blue) and the corrected fields (red) and gridded drifters' data during the period March 2010 to December 2011.

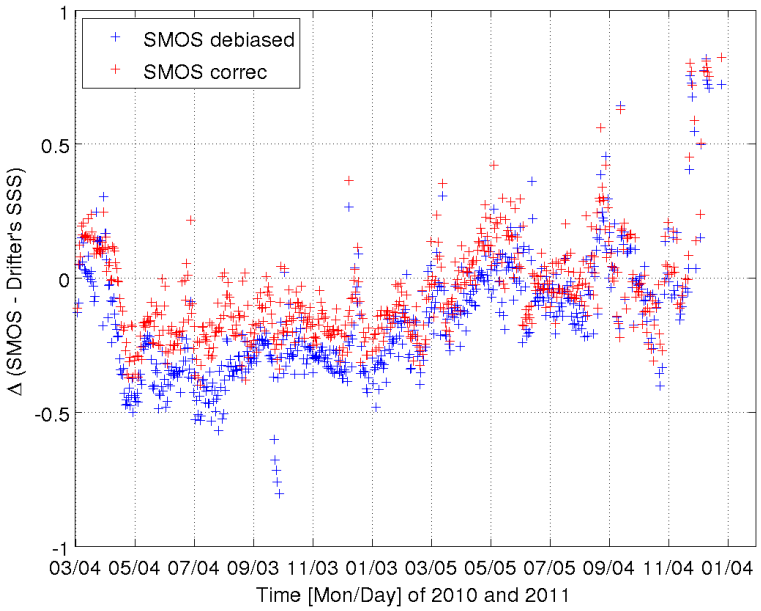

Figure 4.26.: Salinity differences between uncorrected (blue) and bias corrected (red) SMOS salinity and the SVP drifters' salinity during the measurement period 2010 to 2011.

On the average, the SMOS salinity could be adjusted what refers to the mean bias. Not all areas suffering from land contamination could be corrected, and sometimes the correction, when based only on very few Argo data even deteriorates the salinity field. In areas far from the islands' influence the SMOS bias-corrected fields show mean differences < 0.1. A regression

of the differences with time (Figure 4.26) reveals a small positive trend. However, this may be related to SST or latitude as well since most drifters drift southward during the measurement period. A higher variability at the end of 2011 may be due to the drifters' measurement becoming more uncertain due to biofouling in the conductivity cells. This cannot be proven by other independent in situ measurements (compare section 2.2.3) because the collocation pairs are sparse and moreover showed a RMS difference between the measurements of different origin of 0.15.

4.3.3. Comparison to thermosalinograph data

Another in situ data set, mostly independent from the in situ data used for the bias correction of the SMOS L2 salinity data, are derived from the thermosalinographs. These data are included in the in situ data set used for the correction, however, there they were gridded on $1\,^{\circ}\times1\,^{\circ}$ resolution and averaged with other data present on that day in the respective grid box. Here, the validation of the monthly bias-corrected SMOS maps is carried out exclusively with the thermosalinograph data. These were averaged to daily values before gridding them to the $1\,^{\circ}\times1\,^{\circ}$ resolution. The daily differences were calculated from SMOS data which were linearly interpolated between two monthly fields onto the day of the thermosalinograph data, and then averaged for the 4 years of co-existence.

The differences of the uncorrected SMOS salinity product to the thermosalinograph data show again the negative bias around the continents and in the North Atlantic (Figure 4.27). At the eastern rim of the North Atlantic and in the Labrador Sea, also positive bias are present, which can be due to the cold SST, an assumption which is here not proven. The maximum values are saturated in the figure, the averaged values can reach >3. The bias-corrected monthly SMOS salinity fields still show differences to the daily thermosalinograph data, however, the strong negative bias around the continents are considerably reduced. Remaining differences are regionally due to the sampling error. Reminding that the SMOS SSS data are monthly data, and the thermosalinograph data are daily ones, the sampling error during one month has to be considered. Though the thermosalinograph sections are numerous, the data availability for computing the standard deviation within one month on a $1\,^{\circ}\times1\,^{\circ}$ grid is sparse. Values of high monthly std (not illustrated) are found near the river discharge of the Amazon (std > 0.5), in the northwestern North Atlantic (std > 0.2), along the eastern section through the South Atlantic (std ∼0.2), and in the global equatorial band (std ∼0.2). Other regions of remaining differences in the North Atlantic north of $50\,^{\circ}$N and around the Asian continent are due to insufficient correction of the land contamination, due to sparse in situ data or to high noise due to RFI.

The temporally and globally averaged differences are shown in the histogram of Figure 4.28. The RMS and mean differences could be reduced considerably through the bias correction. The RMS differences do not reach the smaller value achieved with the drifter salinity data, however, the simple method applied and the global data including the poorly mitigated land contamination increase the RMS difference in comparison to a regional estimate.

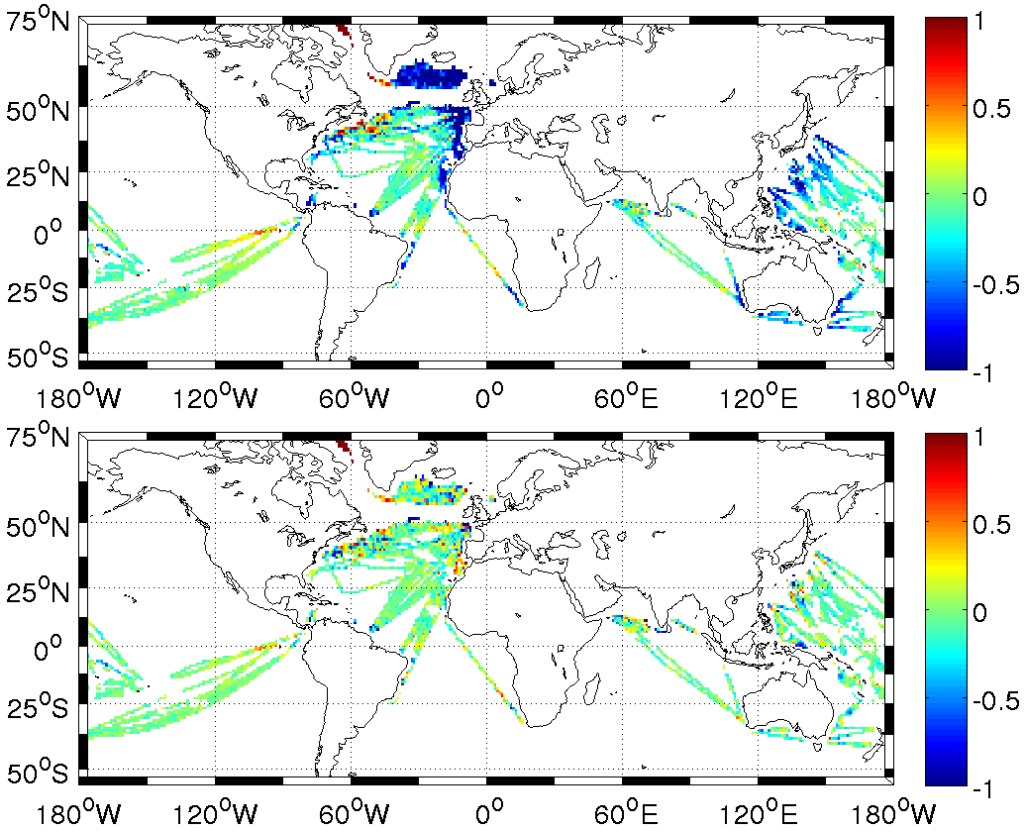

Figure 4.27.: Mean salinity differences between monthly SMOS L3 and global thermosalinograph data, for the uncorrected SMOS SSS fields (upper panel) and the bias-corrected fields (lower panel).

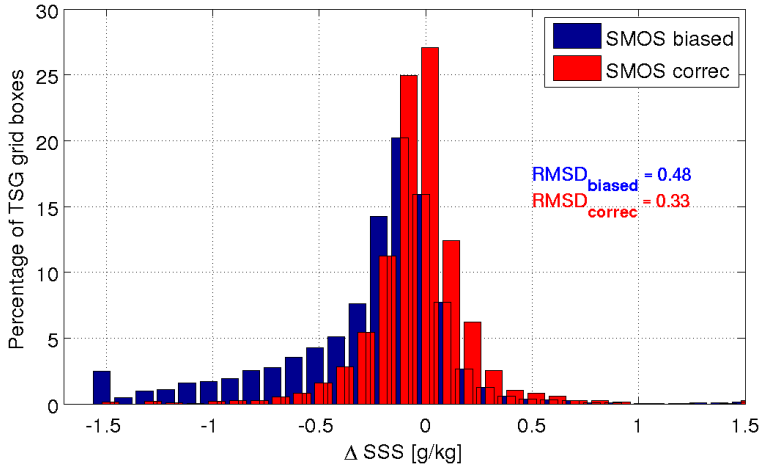

Figure 4.28.: Histogram of salinity differences between uncorrected (blue) and bias corrected (red) SMOS L3 salinity to the global thermosalinograph data with RMS differences indicated in the same colors.

4.4. Summary

The bias of the SMOS ocean salinity data at the L2 level was investigated here in order to characterize the bias independently from averaging in time or space. The error is assumed to be based on some systematic bias, and it could be confirmed here, that the gridded data reveal a dependence on latitude, temperature and wind speed. The temperature dependence is most probably related to the model of the dielectric constant applied and the latitudinal dependence is related to the not properly known total electron content in the atmosphere and the Faraday rotation, both effects influencing the field of brightness temperature. The wind dependent bias is introduced when calculating the salinity and is mostly relevant at high wind speed. All three effects considered here are mixed in the process of calculating the salinity, therefore it is difficult to calculate a bias correction dependent on these parameters. Moreover, the SMOS L2 data from the reprocessed version 5.50 were already bias corrected by the OTT, i.e. they were adopted to a brightness temperature field in a geographic area in the eastern South Pacific, which is assumed to be less contaminated by land in the field of view and by human made emissions, so that the effect of the antenna pattern influencing the brightness temperature field could be corrected for. Nevertheless, several inaccuracies remain in the L2 data. Though the sources of these errors in the construction of the brightness temperature fields as well as in the salinity retrieval are mostly known, it is quite complicated to correct them, since adequate models are still missing or are being developed. The investigation in this respect is still ongoing, and improvement is expected for the next reprocessing versions.

While a lot of studies correct the data at the L3 data level, i.e. after having applied an objective analysis and filtering of the data, using gridded or objectively analyzed in situ data, I applied here an empirical bias correction on the L2 level. On one hand, the bias characterization is as close as possible to the actual in situ data, on the other hand, the bias correction is done here with statistically uncertain data. Due to the large amount of data and the averaging of the calculated bias in space and time, the uncertainty in the correction could be reduced.

Figure 4.29 summarizes the results of the bias correction from the present study and from other studies. This type of illustration efficiently compares different data sets with each other: the standard deviation within each of the data sets, and the centered root mean square differences as well as the coefficient of correlation to the reference data are given in one plot. The different data sets were adapted to the same spatial data coverage since they differ in the latitudinal extent or other limitations in spatial coverage. For the global data comparison (left panel) I constructed a yearly repeating monthly data set from the climatology as the reference data. In the right panel, I used the in situ data set (the EN4 objectively mapped) as a reference and the different satellite data sets in their bias corrected versions.

The standard deviation of all data sets considered are slightly higher than the one from the climatological monthly fields. This is simply due to the constructed climatological time series, which is a sequence of 5 equal annual time series. The bias corrected external salinity fields from CATDS and Aquarius as well as from the EN4OBJ fields show a RMSD of about 0.25 due to the natural interannual variability, whereas the uncorrected and only gridded SMOS fields averaged in the present study show RMSD of more than 0.5. The correlation coefficient for the HH-SMOS and HH-SMOS$_{correc}$ data sets lies around 0.8, and both values come closer

to the climatological data set, when considering the bias corrected fields.

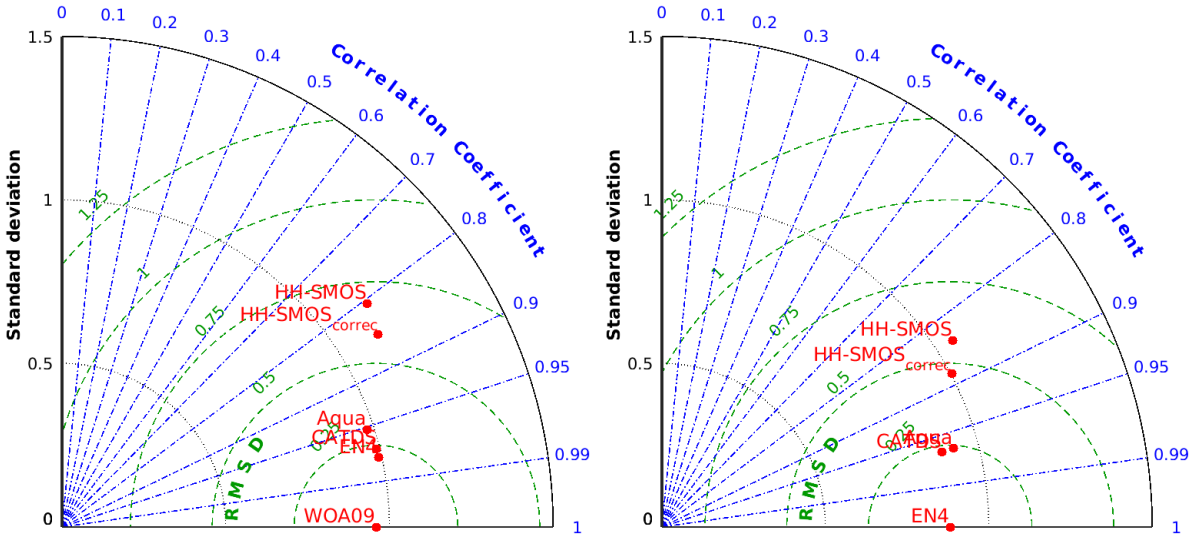

Figure 4.29.: Taylor diagrams for different data sets: The WOA 2009 climatology is the reference data in the left panel, HH-SMOS and HH-SMOS$_{correc}$ are the monthly averaged data calculated in the present study, without and with bias correction; EN4 are the objectively analyzed monthly salinity fields from the in situ data during 2010 to 2014 (*Good et al.*, 2013) are used as the reference data in the right panel; 'CATDS' are the bias corrected fields from the French data set; 'Aqua' are the bias corrected salinity fields from the Aquarius satellite mission. In the right panel only data between 40 °S and 40 °N are considered. RMSD (green dashed lines) is the root mean squared difference to the reference data; the standard deviation within the respective salinity data set is shown on the left hand scale and by the dotted black lines, and the coefficient of correlation with the reference data is shown by the blue dashed lines.

The reason for the other data sets are highly correlated to the climatological values, is that they are not totally independent: The EN4 OBJ data themselves are part of the climatological data, for the CATDS data set climatological data is used for its bias correction, moreover exclude the most critical regions at the northern and southern boundaries; the HYCOM model assimilates the climatological data and is then used for the Aquarius bias correction. In the right panel the data fields were reduced to the latitudinal extent ranging from 40 °S and 40 °N in order to exclude the most critical regions in the SMOS data, and as a reference the EN4OBJ fields are taken. Here, the HH-SMOS data set improves from a RMSD of 0.56 to 0.45, and the correlation coefficient reduces from 0.87 to 0.82. The std and RMSD is higher than in the other data sets, due to the land contamination being poorly mitigated in the HH-SMOS data set, and due to the averaging on 1 °×1 °compared to smoothing on larger scales by the objective analysis.

The bias correction was carried out for all three roughness models. They did not show

a relevant difference in its mean bias or RMS differences to the in situ data (see Table 4.4). However, the comparison between the statistics revealed the model S3 performing best, so that this empirical roughness model was chosen to be incorporated in the published bias-corrected SMOS salinity data set at *http://icdc.zmaw.de/daten/ocean/smos-sss.html*.

Roughness model	S1	S2	S3
Remaining bias	0.081	0.082	0.078
RMS difference	0.68	0.68	0.57
Total error	0.17	0.18	0.18

Table 4.2.: Mean global remaining bias of bias-corrected German SMOS SSS and its RMS difference to in situ salinity (EN4) during 2010 to 2014. The total error (theoretical + bias error) is the globally averaged error of the bias-corrected monthly SMOS SSS data.

Previous efforts to correct the bias was done on the L3 level, i.e. with maps which have been calculated from the biased L2 data, consisting of different bias for the ascending and descending half orbits, which eventually are canceling out. Thereby, a sea surface salinity climatology is used for the basis of correction, the Argo salinity fields themselves. Far from the coast, the quality assessment of the L3 SMOS SSS products averaged on 100 km×100 km and 10 days revealed an accuracy of 0.3–0.4 in the tropical-subtropical region and 0.5 in more poleward regions(CATDS in *Boutin et al.*, 2013; *Reul et al.*, 2012). Monthly L3 SMOS SSS products with a large scale bias correction are consistent with in situ measurements within about 0.20 and 0.14 in the subtropical South Pacific and subtropical North Atlantic, respectively (*Hasson et al.*, 2013a; *Hernandez et al.*, 2014). When reducing the considered area to the latitudinal band of 40 °S to 40 °N, furthermore excluding data pairs closer than 1000 km to land, the HH-SMOS L3 product also resumes to an accuracy of 0.23.

In the most recent published SMOS bias mitigation effort, (*Kolodziejczyk et al.*, 2016) assumes, that the strongest bias due to land contamination is a constant one. The latter authors applied a least square approach to the in situ and space born salinity differences and succeeded in correcting the bias near the coast on the L2 level. Nevertheless, the authors report a global error for the SMOS SSS fields of 0.4–0.5.

5. Freshwater Variability underneath the Pacific double ITCZ

5.1. Introduction

The two satellite missions SMOS and Aquarius provide sea surface salinity (SSS) observations through L-band radiometry with a spatial resolution between 50 km (SMOS) to 150 km (Aquarius), offering an unprecedented global view of surface salinity variations (e.g. *Hasson et al.*, 2014; *Xie et al.*, 2014; *Reagan et al.*, 2014).

Based on those new satellite data sets, several studies have been initiated aiming to identify spatial and temporal variability in space-born salinity measurements and underlying processes. Many of those studies deal with strong salinity signals, notably those located in tropical regions, where river input or surface freshwater fluxes induce strong changes in SSS and therefore strong patterns in regional SSS maps (*Alory et al.*, 2012; *Lee et al.*, 2012; *Hasson et al.*, 2013a). In contrast, *Köhler et al.* (2015) investigated the quality of SMOS and Aquarius data over cold water in the North Atlantic to assess their data quality under a worst case scenario.

Several of those previous analyses specifically addressed the question as how precipitation influences the near-surface salinity budget. An analysis of the mixed layer salinity (S_{ml}) budget by *Yu* (2011) revealed that in regions where the variability of the S_{ml} is mainly due to the freshwater forcing, other processes such as advection and mixing are also important. Both processes might play a strong role in the freshwater balance and their contributions to the salinity budget vary in space and time (*Vinogradova and Ponte*, 2013a). The latter authors did not find a linear relationship between freshwater forcing and salinity changes, globally, but found a high regional correlation between precipitation and salinity changes. Consistent with this finding, SSS variability in the tropical Pacific is strongly influenced by interannual variability of precipitation associated with modes of El Niño and La Niña (*Gouriou and Delcroix*, 2002) as well as with the seasonal migration of precipitation regimes. However, as was shown by *Hasson et al.* (2013a), advection of salinity can also be an important factor for SSS variability.

The aim of the present investigation is to revisit the question of co-variability of the precipitation and sea surface salinity in the tropical Pacific using satellite derived salinity and recent in situ salinity observations obtained during the last decade (2005–2013) and to identify important contributions to the surface freshwater budget in this region. The focus of the present study is on the eastern tropical Pacific where, besides strong precipitation associated with the Intertropical Convergence Zone (ITCZ), the moisture import across Central America from the Atlantic into the eastern Pacific establishes another important seasonally varying freshwater source (*Alory et al.*, 2012). Also present in the study region is the additional, but less known, belt of weaker precipitation south of the equator associated with atmospheric

convection during boreal spring of non-El Niño years between 10 °S and 5 °S (*Masunaga and L'Ecuyer*, 2010). Since the mixed layer depth is shallow in this region and the pycnocline is strong, even weak precipitation should leave a clear imprint in SSS fields. The study region is therefore particularly suited for investigating whether SSS signals may serve as a "rain gauge". To address this question, I will investigate the mechanisms establishing the low salinity pattern underneath the southern ITCZ between March and June by quantifying all relevant components of the mixed layer freshwater budget.

5.2. Salinity budget

The evolution of the salinity in the mixed layer (S_{ml}) of a box can be derived from the conservation equation similar to *Yu* (2011, 2014) or *Mignot and Frankignoul* (2003) according to

$$H_{ml}\frac{\partial S_{ml}}{\partial t} = S_{ml}(E-P) - U\nabla_h \cdot S_{ml} + Entr + mixing. \tag{5.1}$$

I neglect mixing here, and the horizontal salinity divergence within the box is derived by computing the freshwater transports across the lateral boundaries, thus the equation simplifies to:

$$\frac{\partial S_{ml}}{\partial t} = -\left(\nabla_h \cdot FWT_{x,y} - (E-P)\right)\frac{S_{ml}}{H_{ml}} + Entr. \tag{5.2}$$

As can be seen, horizontal freshwater transports are linked to salinity changes by the ratio of the S_{ml} to the depth of the mixed layer, $\frac{S_{ml}}{H_{ml}}$. The horizontal freshwater transports (FWT) in zonal and meridional direction,

$$\begin{aligned} FWT_x &= \frac{1}{A}\left(\int_{y_1}^{y_2} uS_a\, dy\, \Delta z\right) \\ FWT_y &= \frac{1}{A}\left(\int_{x_1}^{x_2} vS_a\, dx \Delta z\right) \end{aligned}$$

are calculated across the boundaries of the box using the negative salinity anomaly $S_a = 1 - \frac{S}{S_{ref}}$ with S being salinity averaged within the mixed layer at each point of the respective section, and the reference salinity, S_{ref}, being the average salinity in the considered box down to the mixed layer depth. FWTs are summed along the meridional or zonal box boundaries, respectively, and are normalized by the area (A) of the box, thus yielding the freshwater inflow per m^2 of the box. $\Delta z = 30m$ is the depth for which the horizontal current components, u and v, are assumed to be representative, and x_i, y_i are the geographical box boundaries. Multiplying FWT_x and FWT_y by the box averaged S_{ml}/H_{ml} yields the contribution of the FWT to salinity changes (in psu per month) in the considered box.

Finally the entrainment through a deepening mixed layer depth H_{ml} is estimated as $Entr = (W - \frac{\Delta H_{ml}}{\Delta t})\frac{\Delta S}{H_{ml}}$. Here ΔS is the difference between the salinity of the isopycnal mixed layer and the salinity at the mixed layer depth, $\frac{\Delta H_{ml}}{\Delta t}$ is the change of the mixed layer depth over one month, and W is calculated from the divergence of the horizontal volume transports down to 30 m in order to be consistent with the horizontal fresh water transports. This is calculated for each grid point of the box and then averaged. We note that entrainment takes

place only if $Entr > 0$.

Mixed layer depth

Following *de Boyer Montegut et al.* (2007), the mixed layer depth was calculated from the Argo single profiles in the tropical Pacific by calculating the isothermal or isopycnal mixed layer depths using the criterion $\Delta T < 0.02K$ or $\Delta\sigma < 0.03kg/m^3$, respectively. The first one was used only for deriving the barrier mixed layer. Temperature and salinity data of the upper 12 m depth range were averaged subsequently to characterize the surface layer; and the S_{ml}, mixed layer temperature and isopycnal mixed layer depth (H_{ml}) were mapped subsequently as monthly means onto a 1 ° x 1 ° grid using an influence radius of 2 °, a cutoff radius of 4 °, and a moving weighted time window of 3 months.

5.3. Tropical Pacific Surface Salinity Distribution

5.3.1. Time-mean Sea Surface Salinity

The boreal spring SSS field of the tropical Pacific is displayed in Fig. 5.1 as it was retrieved by SMOS (upper pane), Aquarius (middle panel), and as it is available from the Argo EN4 analysis at 5 m depth (lower panel). During this time of the year the salinity of the tropical Pacific shows distinct spatial pattern of fresh surface waters located along a zonal band of low salinity underneath the north equatorial ITCZ and especially in the north equatorial eastern region, where seasonal strong precipitation and the high speed gap winds interact with a complicated upwelling regime to lead to the east Pacific Fresh Pool (EPFP) there (*Alory et al.*, 2012). In contrast, high-salinity surface waters are located south of the equator in the eastern part of the basin and also north of about 18 °N. Those high salinity values are found in previous studies, including the recent study by *Hasson et al.* (2013a), where E-P is positive. The South Pacific subtropical salinity maximum does not vary much in amplitude or in latitudinal position, but shifts longitudinally by up to 10 ° on seasonal to interannual time scale (*Hasson et al.*, 2013a). All SSS distributions show a relative salinity maximum along the equator in the central Pacific, probably related to upwelling as explained in *Maes et al.* (2014).

Of specific interest for the present study is the area of low salinity located in the southeastern tropical Pacific roughly along 5 °S in the longitudinal range of 140 °W to 87 °W, marked by a rectangular in the upper panel of Fig. 5.1. This region is located underneath the southern, or double, ITCZ (*Masunaga and L'Ecuyer*, 2010, 2011) (henceforth referred to as dITCZ) which is associated with a weaker convergence zone that forms only in the months February to April. The sea surface temperature (SST) in this region is low during most of the year due to advection of upwelled water off the South American coast by the South Equatorial Current (SEC). In boreal winter, however, the southern trade winds as well as the wind driven upwelling weaken, shortwave radiation heats up the southern tropical Pacific and warmer water is advected northward by the SEC. The appearance of this relatively warm band precedes deep atmospheric convection and succeeding rainfall lagged by 2 months (*Masunaga and L'Ecuyer*, 2010).

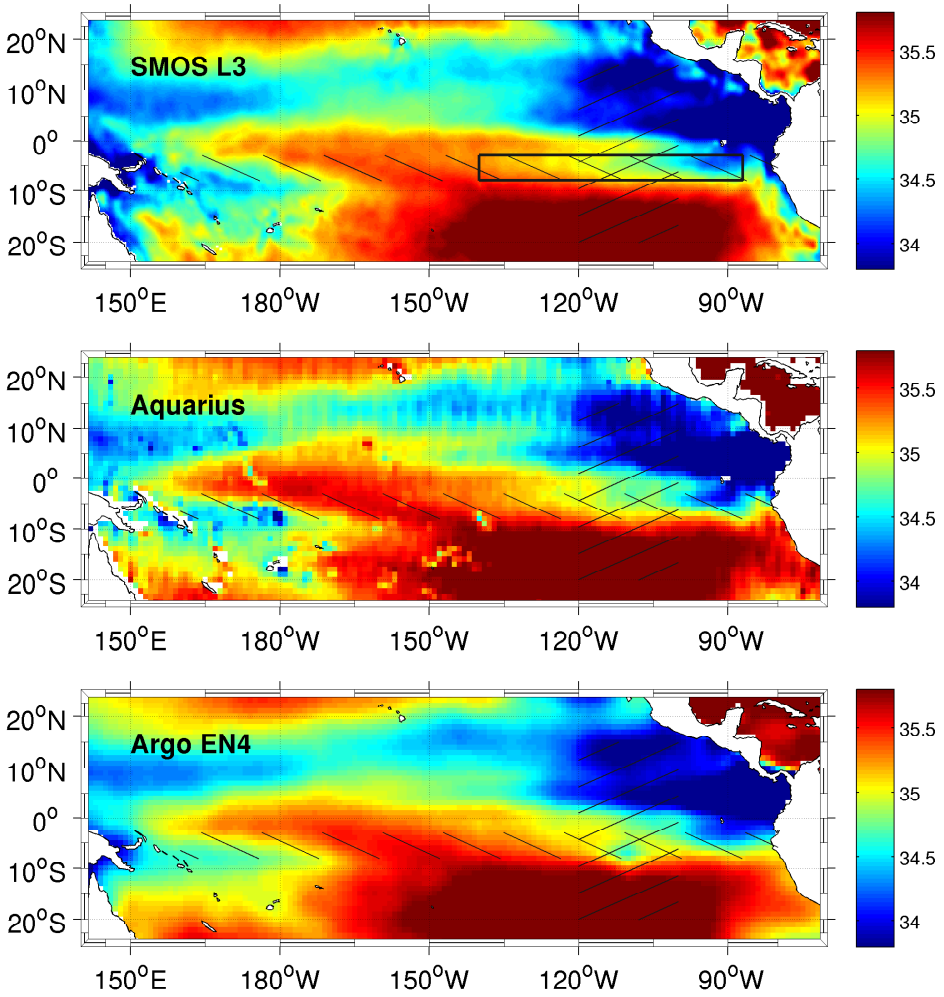

Figure 5.1.: Averaged sea surface salinity field in boreal winter/spring months (February to April) from SMOS BEC L3 data (upper panel), Aquarius CAP V3 data (middle panel), and Argo EN4 data (lower panel) in 2010 to 2013. From the hatched region averaged sections will be presented, in the rectangular (upper panel) the salinity budget will be calculated.

The spatial patterns of all three SSS estimates largely agree with each other. However, compared to SMOS, the Aquarius field appears more noisy because it is based on only two spring seasons, i.e. the spatio-temporal sampling is reduced for Aquarius relative to SMOS. Both satellite products show the low salinity along about 5 °S in the eastern Pacific which had been found recently also by *Kao and Lagerloef* (2015). In contrast, the Argo EN4 field reveals a much smoother salinity distribution in which the distinct salinity minimum at 5 °S is absent, presumably because of lower data availability and the spatial smoothing applied to the analysis. Nevertheless, a detailed inspection of Argo profiles confirms the existence of this

salinity minimum in individual profiles around 5 °S reaching from the surface down to about 30 m depth (Fig. 5.2). The salinity minimum associated with very light water is developed best during April; it is absent during August (lower panel of Fig. 5.2). The density is low not only because of low salinity but also because of associated high temperature (not shown).

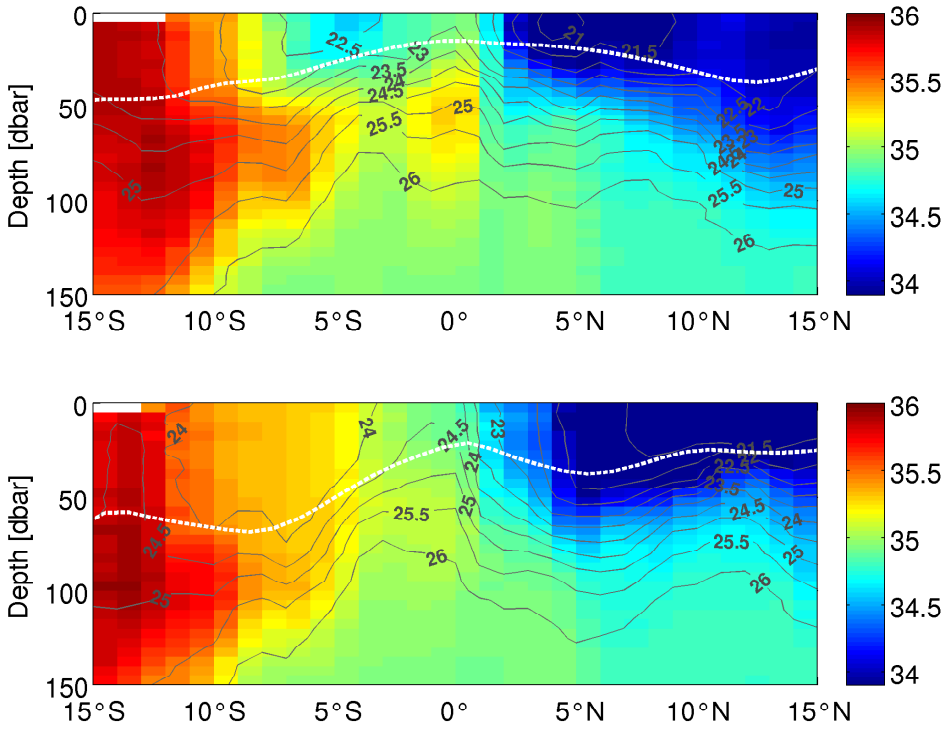

Figure 5.2.: Salinity (color shading) and potential density (σ_θ in g/m^3, contours) distribution along 120 °W to 95 °W from Argo profiler data averaged in all months of April (upper panel) and in all months of August (lower panel) during 2010 to 2013. White dashed line indicates the depth of the isopycnal mixed layer in the respective month.

In an attempt to quantify the quality of the SMOS and Aquarius SSS retrievals in the study region, Fig. 5.3 shows in the left panel the differences between individual near-surface Argo salinity measurements and SMOS and Aquarius retrievals, respectively, collocated within each grid box of 1 °×1 ° longitude and latitude and the respective month. In the right panel, similar differences are shown, but using the Argo EN4 analysis. The figure nicely demonstrates that the SMOS and Aquarius data are consistent with the in situ data up to +/−0.2 root mean square (RMS) and even better relative to the EN4 field. The RMS difference increases to 0.3 to 0.4 for both products north of 4 °S, presumably related to the influence of precipitation on SSS.

The difference shown must not be interpreted as errors of the satellite products only, since they reflect also problems in Argo data or actual near-surface processes that can lead to

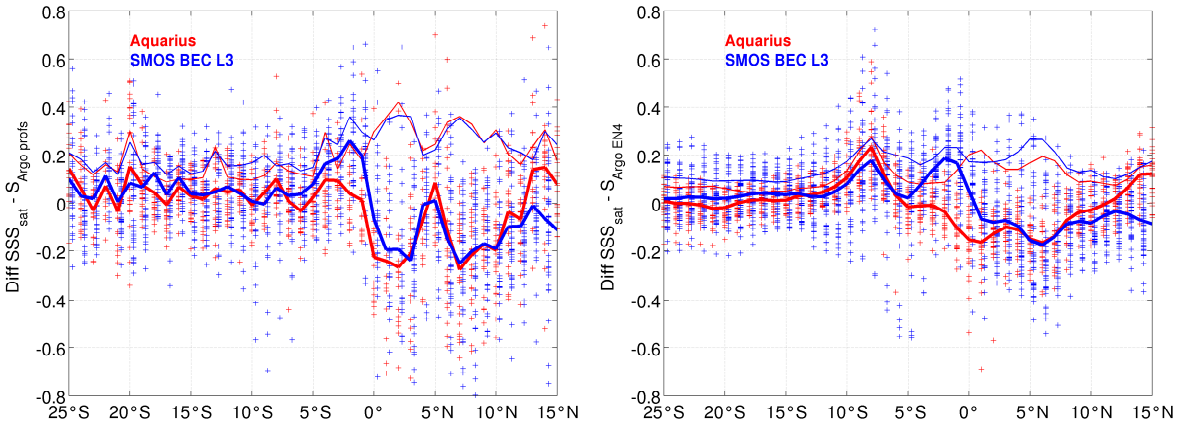

Figure 5.3.: Salinity differences between data from Aquarius (red) and SMOS BEC L3 (blue, as indicated in the legend) gathered in the longitudinal range 120 °W to 95 °W to the single uppermost salinity measurements of Argo profiler (left panel), and to the objectively analyzed near surface Argo EN4 fields (right panel) in the years 2010 to 2013. Thick lines are mean values and thin curves are the root mean square differences of all data pairs in the 1 ° latitudinal sections, crosses show the single values.

differences in SSS and the uppermost Argo data. The mean difference (thick line in Fig. 5.3) of both satellite products to in situ values is < 0.1 south of 5 °S. Negative values between 1 °S and 10 °N may reflect natural vertical salinity gradients which form by advection of low salinity surface water from the east, interrupted around 5 °N by the North Equatorial Countercurrent (NECC) advecting higher saline water (*Kessler*, 2006), and the presence of precipitation within the northern ITCZ. North of 15 °N both satellite products show higher RMS differences to Argo salinity which is presumably related to land contamination (not shown). The mean differences to the single profiler data are higher than to the EN4 data, reflecting that Argo data and satellite footprint represent quite different samples of SSS, the former being more subject to small-scale variability. Finally, the positive mean difference of 0.2 relative to the objectively mapped Argo EN4 fields could likely be related to sea surface effects such as the modulation of sea surface roughness by current wave interaction and the air-sea instability. Respective SMOS SSS biases found by (*Yin et al.*, 2014) decrease locally when using SSMI wind speed instead of ECMWF (used in the present version) in the salinity retrieval. However, the salinity bias obtained is much less than the bias of 0.46–0.49 found by *Yin et al.* (2014) during August 2010 and September 2011 using ascending orbits only, probably because the SMOS SSS product as well as the Argo data set are not the same versions as used by *Yin et al.* (2014). It is nevertheless noticeable that the bias found is very consistent with the hypothesis of *Yin et al.* (2014) that the radiometer sensed roughness in that region is not only related to atmospheric wind speed, but also to ocean processes; accordingly, SMOS SSS is decreased by about 0.2 when SSM/I wind speed is used as a priori in the SMOS SSS retrieval, instead of ECMWF wind speed.

5.3.2. Temporal SSS variability

The standard deviation (std) of SSS fields, shown in Fig. 5.4, reveals enhanced SSS variability in the tropical Pacific where precipitation shows a strong seasonal cycle (*Alory et al.*, 2012). Highest salinity variability is confined to the eastern tropical Pacific area north of the equator; it extends westward into the northern ITCZ, reflecting its latitudinal shifting and associated influence of precipitation. A further extension is found at 2 °N to 4 °N, north of the Galapagos islands.

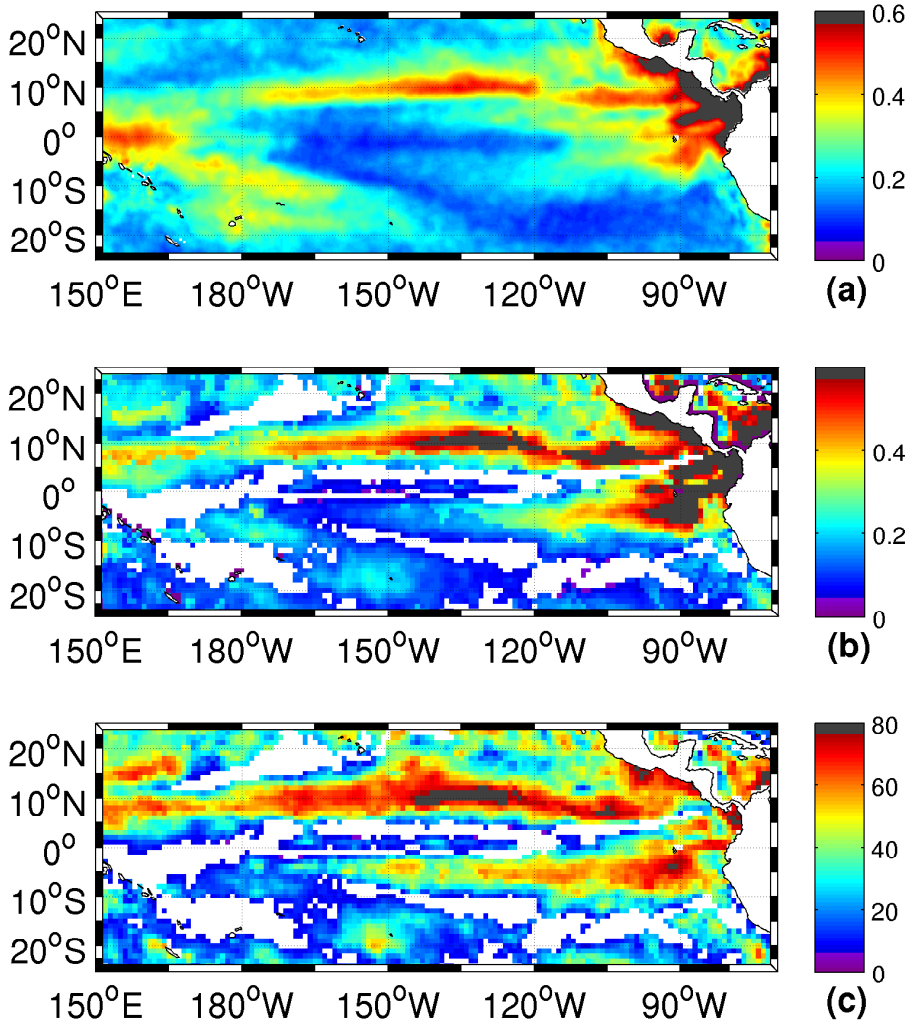

Figure 5.4.: Variability of SSS from 4 years (2010–2013) of SMOS (BEC L3): (a) Total SSS standard deviation; (b) amplitude of the annual and semiannual harmonics of SSS; (c) ratio of the seasonal to the total SSS variance in percent. White areas in panels (b) and (c) denote non-significant results for the amplitude.

There is also a clear gap in the enhanced variability underneath the ITCZ east of 120 °W. Enhanced SSS variability in the western warm pool of the Pacific and stretching from there south-eastward at least partly can reflect the impact of the atmospheric freshwater forcing there.

To quantify the extent to which tropical Pacific SSS variability resides on the seasonal time scale, the first and second annual harmonics were computed from the time series of the SSS data at each point of the tropical/subtropical Pacific. The amplitude of the seasonal cycle is plotted in the middle panel of Fig. 5.4. Overall, there is enhanced variability due to the seasonal cycle in most regions where the total SSS variability is high. This is especially obvious from the lower panel of Fig. 5.4 showing the percentage of the total SSS variance explained by the seasonal cycle. In the area underneath the ITCZ as well as in the eastern part of the subtropical Pacific more than 70% of the total variability reside on the annual and semi-annual frequency. Another region of enhanced seasonal variability percentage is associated with the dITCZ along about 5 °S, eastward of 120 °W, where SMOS shows a seasonal SSS amplitude up to 0.6 and where the seasonal variability amounts to 60%–80% of the total variability.

In contrast to the eastern Pacific, the southwest Pacific shows a much lower contribution of the seasonal to the total SSS variability. While the total variability is high there, it is largely caused by interannual variability, associated with climate modes (*Delcroix et al.*, 2005; *Hasson et al.*, 2014). Since the tropical Pacific is dominated by climate modes such as ENSO, surface salinity patterns can be expected to vary between years, not just in the western part. This is demonstrated in Fig. 5.5 showing the monthly anomalies of the SMOS and Argo EN4 salinity fields computed as the differences to the 4 year mean and averaged for February to April. In the spring phase the northern ITCZ is now associated to relatively high salinities because precipitation is relatively low during boreal spring. The southward shifting of the ITCZ in spring which is reflected in the fresh anomalies along 5 °N to 8 °N seems to vary during the years. The salinity minimum in the east Pacific north of the equator associated to the EPFP (*Alory et al.*, 2012) is evident in all years, in less intensity in 2013.

Another minimum zone lies along about 5 °S. Salinity along 3 °S is quite variable during the years 2010 to 2013 so that the mean salinity field in Fig. 5.1 does not show the distinct salinity minimum along 5 °S as clearly as the salinity anomaly fields in the individual years show. During 2010 (uppermost panels), the low salinity band lies north of the box (indicated in Fig. 5.1), however, during the remaining years, the box encompasses the low salinity region quite well between about 3 °S and 8 °S. It extends from the coast of South America in the eastern Pacific westward roughly to about 140 °W (details vary between years). East of the Galapagos islands, there seems to exist a connection between the low salinity patches of the Fresh Pool and the one at 5 °S, which may indicate advection of low salinity water from the north of the equator. The Argo fields show very similar structures, though very much smoothed, and in 2013 the low salinity band can hardly be revealed.

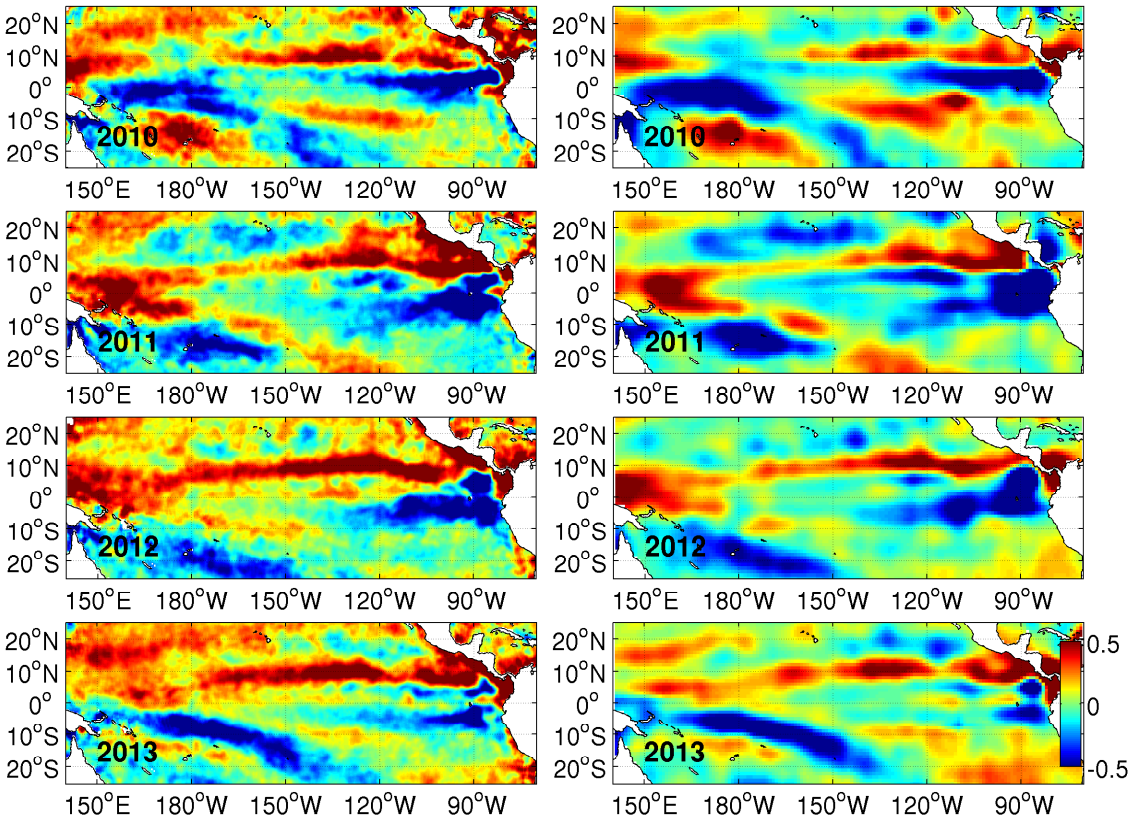

Figure 5.5.: Salinity anomalies (monthly deviations from the 4 years mean averaged from February to April) from SMOS (left panels) and from uppermost Argo EN4 fields (right panels) in the 4 years 2010 (uppermost panels) to 2013 (lowest panels).

Fig. 5.6 shows the zonally averaged differences of the SMOS and Aquarius data with respect to single Argo values as well as to the Argo EN4 fields during 2010 to 2013, analyzed between 120 °W and 95 °W (see Fig. 5.1a for position of the section). The figure clearly reveals that the differences of up to 0.4 in magnitude between the individual data sets are time dependent and may be related to problems of the retrieval algorithm. However, the figure also reflects the availability of Argo data in space and time, revealing the presence of fewer data just south of the equator. Sampling errors by Argo would be the consequence which could explain the differences to earlier results reported by *Yin et al.* (2014). In the right panels a positive bias at 8 °S during 2012 is noticed again which is assumed to be due to the uncertainty of the interpolated fields, because it is not evident in the single values.

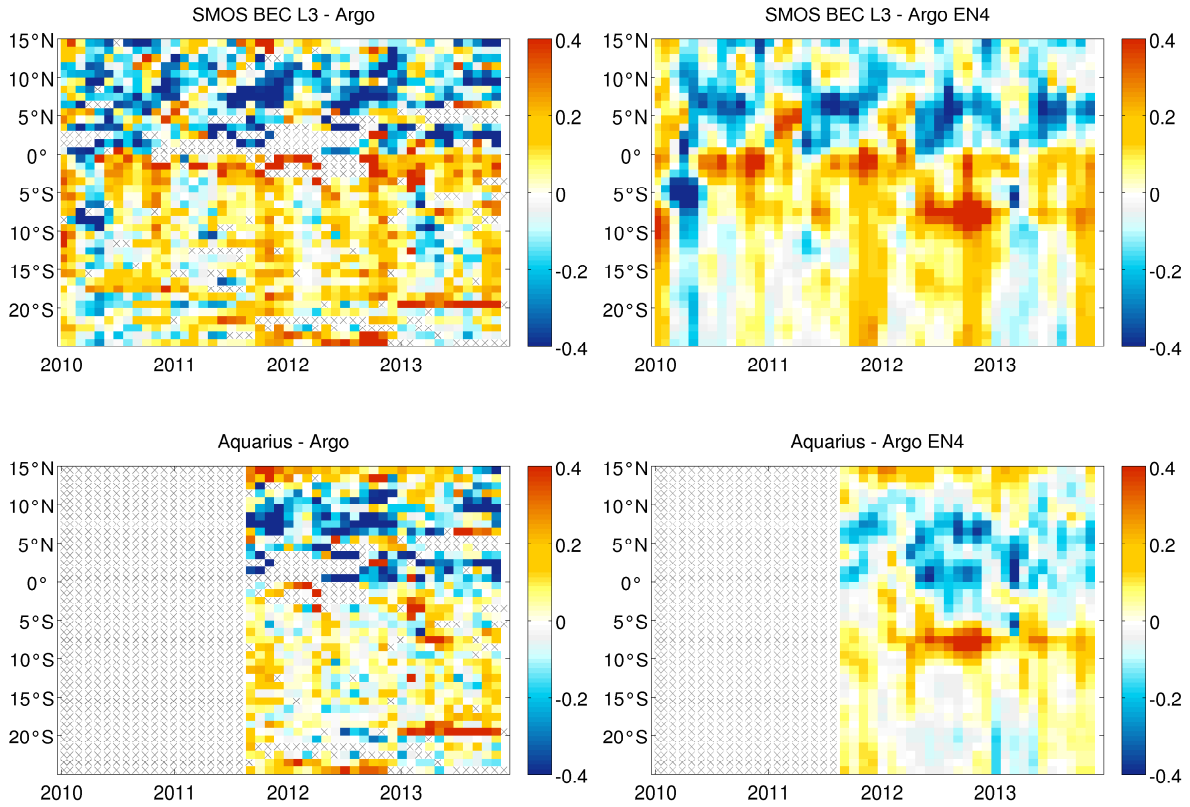

Figure 5.6.: Time evolution of the difference of satellite retrieved salinity from SMOS BEC L3 (upper panels) and Aquarius CAP V3.0 (lower panels) averaged in the longitudinal range 120 °W to 95 °W to the single uppermost salinity measurements of Argo profiler (left panels), and to the near surface Argo EN4 fields (right panels) during the years 2010 to 2013. Grey crosses indicate no data pair availability.

5.4. Relation between SSS changes and local precipitation

Negative surface salinity anomalies can be caused by several processes, including heavy precipitation events as was documented most recently by *Boutin et al.* (2014). Whether such a relation holds over larger parts of the low-latitude Pacific is tested in Fig. 5.7 showing the local correlation between SMOS SSS anomalies and precipitation time series. Prior to computing the correlation coefficients on a geographical grid, underlying monthly mean precipitation fields of the version 2.2 of the Combined Precipitation Data Set, provided by the Global Precipitation Climatology Project on a 2.5 °×2.5 ° geographic grid (http://www.esrl.noaa.gov/psd/data/gridded) were interpolated onto a 1 °×1 ° geographic grid using bi-linear interpolation. The uncertainty of the original precipitation fields is specified by the project to be 15 % of the amplitude (*Adler et al.*, 2003). Since only monthly mean fields

of the salinity and precipitation variables are available, it is not possible to infer any time lags in the response of salinity to the precipitation events at timescales less than a month.

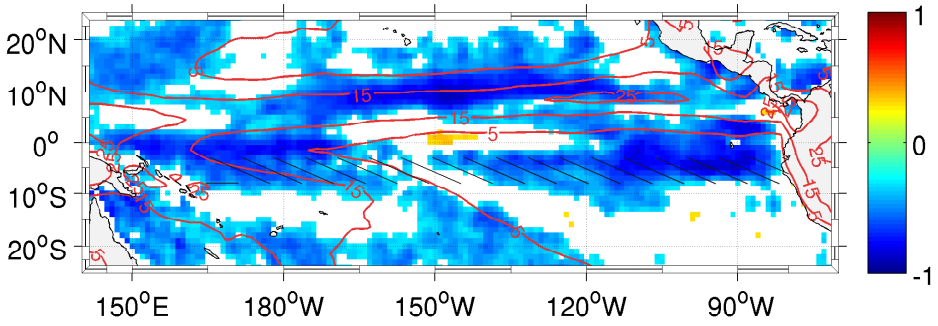

Figure 5.7.: Correlation coefficient between GPCP precipitation and SMOS SSS anomaly time series from January 2010 to December 2013 (white areas indicate non-significant results). Red contours show the average amount of precipitation per month [cm/month] during the 4 years.

Figure 5.7 reveals negative correlation values (<-0.5), indicating enhanced impacts of surface freshwater forcing, in the latitudinal band along 5 °S which is shifted away from high precipitation regions. An enhanced correlation between salinity changes and freshwater forcing (E-P) in the band along 5 °S can also be seen in results shown by *Yu* (2011) (her Fig. 7f and Figs. 9 and 10); however this finding was not mentioned in her work. Low salinity due to precipitation along the belt at 5 °S has also been reported previously by *Delcroix and Hénin* (1991) analyzing a frequently sampled voluntary operating ships (VOS) section crossing the latitude 5 °S at about 120 °W. This region is characterized by relatively large salinity variations on seasonal time scales (see also Figs. 5.4 and 5.5). It is somewhat counter intuitive that underneath enhanced precipitation bands correlation values are reduced. In case of the southwest Pacific, I think that this is caused there by the fact that the freshwater input through the surface enters into an extended surface mixed layer, thereby resulting in only relatively small salinity changes.

Findings about low SSS values in the poorly studied eastern tropical Pacific were also reported recently by *Kao and Lagerloef* (2015) and *Yu* (2014) based on Aquarius data and *Maes et al.* (2014) based on SMOS data. In his review paper, *Kessler* (2006) reported that the strength and the variability of the currents east and south of the Galapagos islands are largely unknown. Relevant for the existence of these low surface salinity waters are also the northerly gap winds transporting moisture from the Atlantic ocean across the Panama isthmus at 5 °N, forcing water from the fresh pool equatorwards into the study region.

The temporal variability in this low salinity area is analyzed in Fig. 5.8 along a zonal section across the zonal extent of the Pacific showing precipitation fields together with Argo-inferred S_{ml} and SMOS SSS, all averaged meridionally between 3 °S and 8 °S (hatched area in Fig. 5.1). As can be seen from the Fig. 5.8a, each boreal spring time the band of enhanced precipitation is evident in the eastern half of the section. The band of precipitation is not

extending from the east as far west as the patches of low salinity (Fig. 5.8b and c), indicating that advection by the south equatorial branch of the westward SEC is more effective than mixing in this region. The reader may note, the years 2005 and 2010 show very low precipitation rates. The low salinity pattern in 2010 (Fig. 5.5) indicates precipitation between 3 °S to several °N, confirming results from *Lietzke et al.* (2001) who found a correlation between the amount of precipitation under the dITCZ and the SST anomalies within the Niño3 region. Corresponding to the low salinity, the density also shows minimum values during boreal spring (Fig. 5.8). The 4 year evolution of the SMOS SSS along the section (Fig. 5.8c) is very similar to the one of S_{ml} from Argo data. While the section based on individual Argo profiles still shows data gaps which turns the tracing of the low salinity pattern difficult, one can see again the additional information from the satellite salinity fields. Also in the SSS distribution, the eastern part shows a seasonally consistent low salinity band extending from the east to 120 °W in 2010, and to about 140 °W to 160 °W in the other years with SSS < 35.2. In 2010 the salinity minimum band has formed despite very low precipitation amplitudes.

The salinity values in the east of the section compare well between Argo and SMOS data, whereas in the west, SMOS SSS observations are lower than what is reported by Argo in the mixed layer. *Hasson et al.* (2014) also noticed worse agreements with thermosalinograph data in the western Pacific Ocean than in the eastern Pacific Ocean likely due to RFI coming from islands. The very low salinity in the SMOS SSS near the coast at 80 °W is however due to the land contamination in the satellite salinity retrieval.

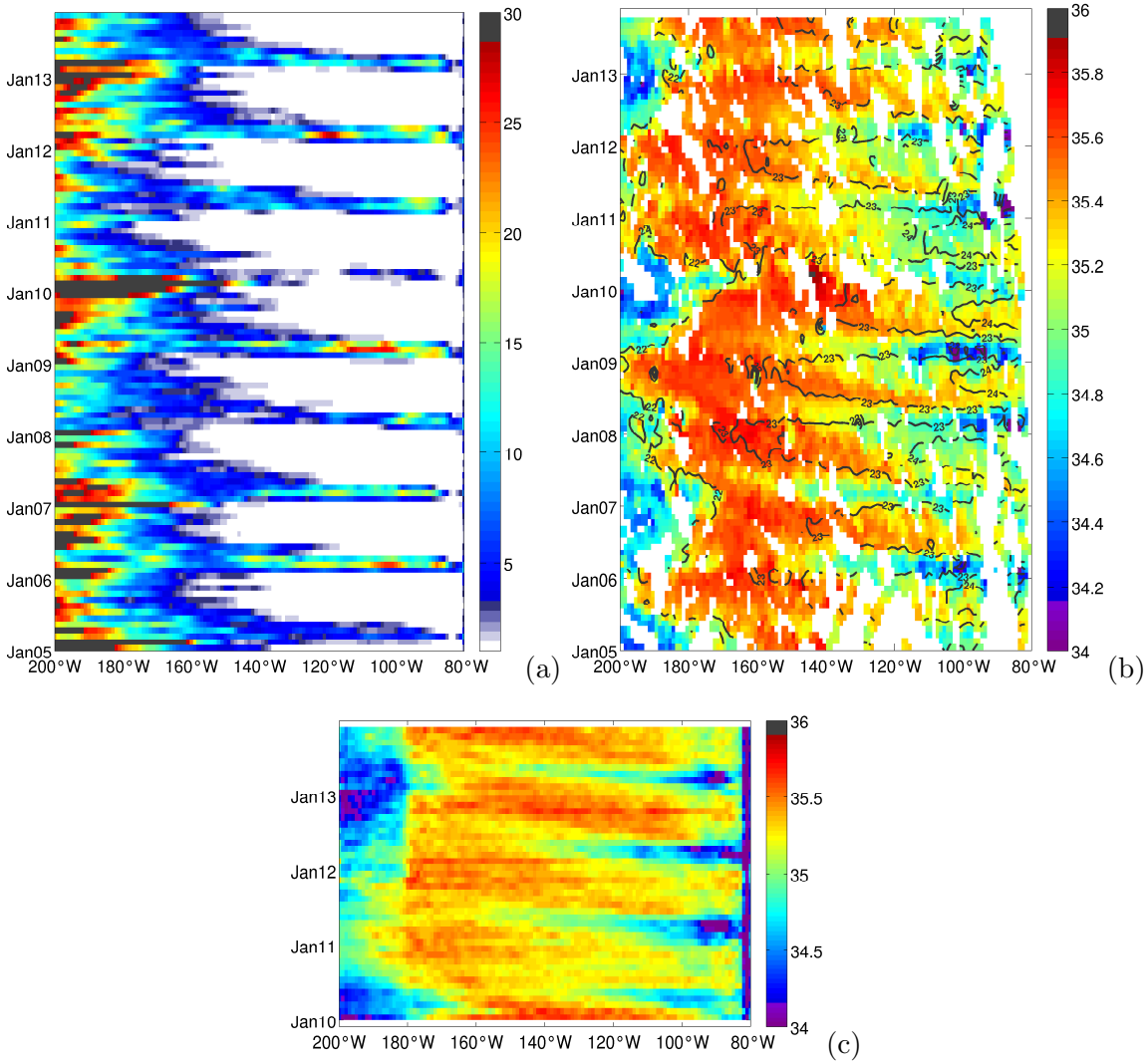

Figure 5.8.: Hovmoeller diagram of (a) precipitation (GPCP) [cm/month], white gaps indicate no rain; (b) Argo salinity (single profiles, shaded) with potential density (σ_θ =22, 23 and 24 g/m^3) overlaid, white gaps indicate no data; and (c) SMOS BEC L3 SSS, averaged between 3 °S to 8 °S for each month available (hatched area in Fig. 5.1).

The time evolution of the freshwater pattern at 5 °S is illustrated in Fig. 5.9 showing a meridional section of Argo S_{ml} averaged between 120 °W and 95 °W (hatched area in Fig. 5.1). Superimposed to the figure are contours of the mixed layer potential density which suggest that each year light and low salinity waters intrude the southern equatorial Pacific from the north, thereby decreasing the salinity together with the density between 3 °S and 8 °S. The intensity and the extension of the low salinity patch vary from year to year. As before, 2005 and 2010 show weaker salinity minima than other years related to the much reduced east Pacific dITCZ

during El Niño events (*Zhang*, 2001). The low salinity at the equator and further south around January again hints to a possible connection to the EPFP.

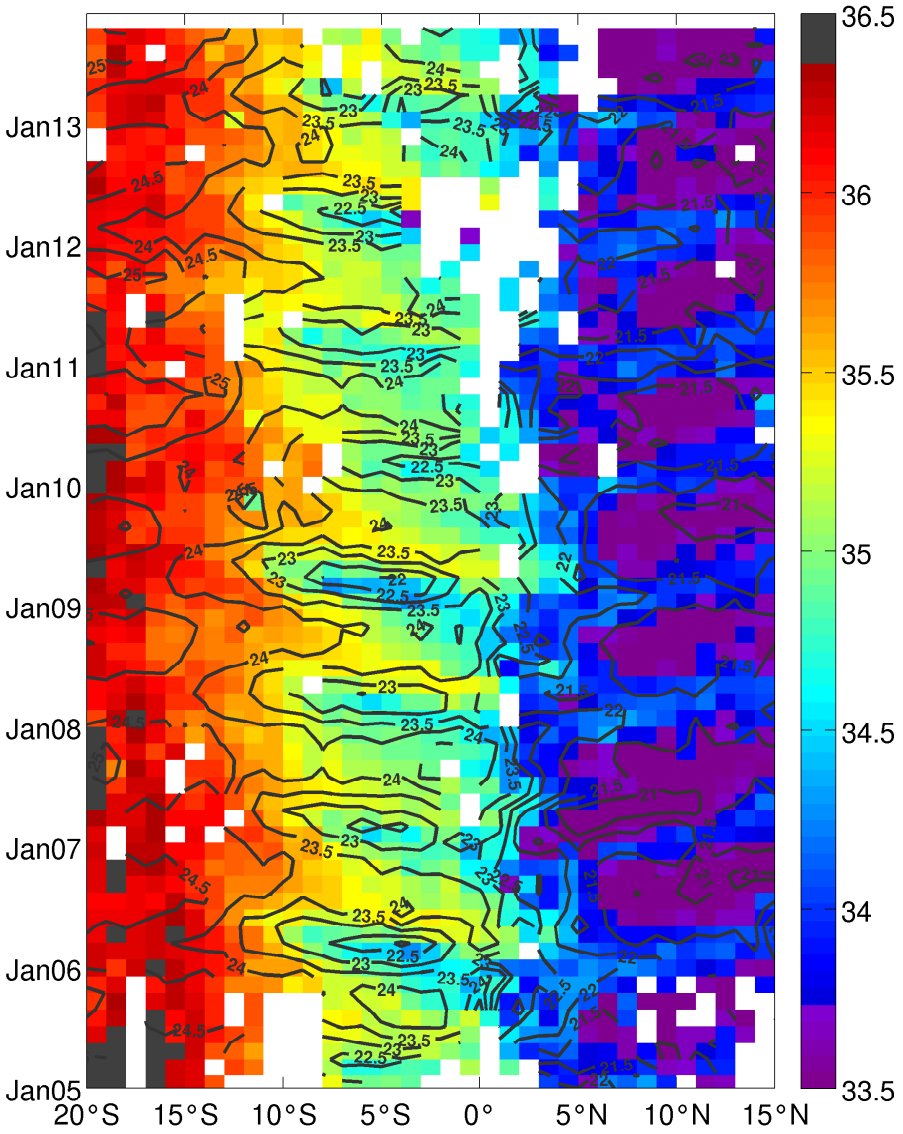

Figure 5.9.: Hovmoeller diagram of uppermost Argo salinity (from single profiles, shaded) averaged between 120 °W to 95 °W (hatched area in Fig. 5.1) during 2005 to 2013. White gaps indicate no data availability. Contours of potential density of the mixed layer (σ_θ in g/m^3) are overlaid.

5.5. Eastern tropical Pacific Salinity Budget

To examine which processes contribute in detail to the evolution of the near surface salinity in the south equatorial band, the mixed layer freshwater budget was established for the box depicted in Fig. 5.1a. The respective box-averaged time series of the salinity in the surface mixed layer analyzed from Argo profiles is shown in Fig. 5.10.

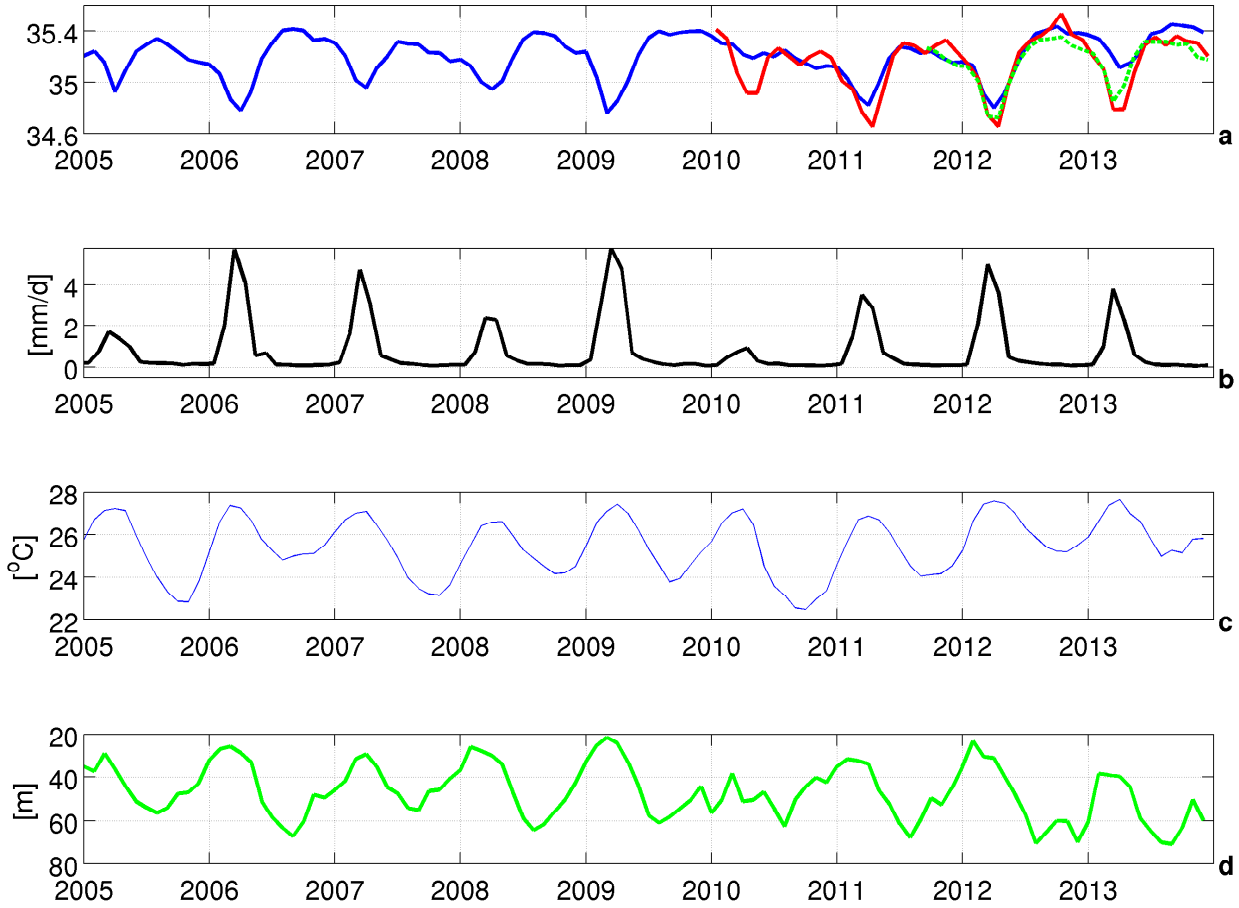

Figure 5.10.: Averaged quantities in the box delimited by 3 °S to 8 °S and 140 °W to 87 °W (box depicted in Fig. 5.1): (a) Sea surface salinity in the mixed layer from Argo measurements (blue), from SMOS BEC L3 data product (red) and from Aquarius (green, dotted); (b) monthly precipitation from GPCP data; (c) monthly averaged temperature of the mixed layer; (d) monthly averaged depth of the isopycnal layer calculated from Argo profiles.

As part of this analysis, the mixed layer depth was determined from each individual Argo profile available in the area under investigation and averaged subsequently over the domain of the box together with the salinity and temperature observations within the mixed layer. Also

shown in the figure is a time series of box-integrated monthly accumulated GPCP precipitation data.

As can be seen from the figure, the S_{ml} show a pronounced annual cycle, with minimum salinity values occurring during spring; exceptions can be found during the years 2005, 2010 and to some extent during 2007, when the minimum is less pronounced. All these weaker minima occur during years coinciding with El Niño events and could represent the associated interannual variability also seen in Fig. 5.5. Typically, normal low spring salinity months coincide with, or follow briefly after a high-precipitation month, usually occurring in February. During the months January to March the mixed layer is with about 30 m very shallow, leading to high mixed layer temperature of approximately 27 °C during the same period (Fig. 5.10c). Simultaneously a sharp seasonal thermocline has formed as well as a thin barrier layer (both not shown). An exception can be seen during 2010, when the spring mixed layer depth exceeds 40 m, supporting the hypothesis of *Masunaga and L'Ecuyer* (2010) that interannual variability may be partially related to modulations of the depth of the mixed layer. The temperature in late 2005, 2007 and 2010 is minimum in this time series, at least in 2010 probably related to the La Niña phase during that year (*Hasson et al.*, 2014).

SMOS SSS (in red) as well as Aquarius SSS (green) follow very closely the S_{ml}. However, slightly stronger extrema especially in 2013 and spring salinity minima appear more pronounced in the satellite retrievals, which also suggest an earlier appearance of the minimum by roughly one month. While precipitation appears reduced in 2010 and to some extent also in 2013, the surface SSS retrievals show still a significant salinity minimum; however, averaged over the mixed layer this appears much reduced during these events that show anomalously shallow mixed layer (Fig. 5.10d) and also a stronger mixed layer temperature evolution (Fig. 5.10c) later in the year.

To derive the processes contributing to the salinity fluctuations in the box a salinity budget is established for the box as detailed in the method section for the years 2005 to 2013, calculating the contributions of the fresh water transports across the lateral boundaries, the fresh water forcing at the surface and the entrainment from below through the bottom of the mixed layer. Finally, to estimate the seasonal cycle of the salinity budget, a monthly climatology was formed for each component from the 9 year-long time series (Fig. 5.11).

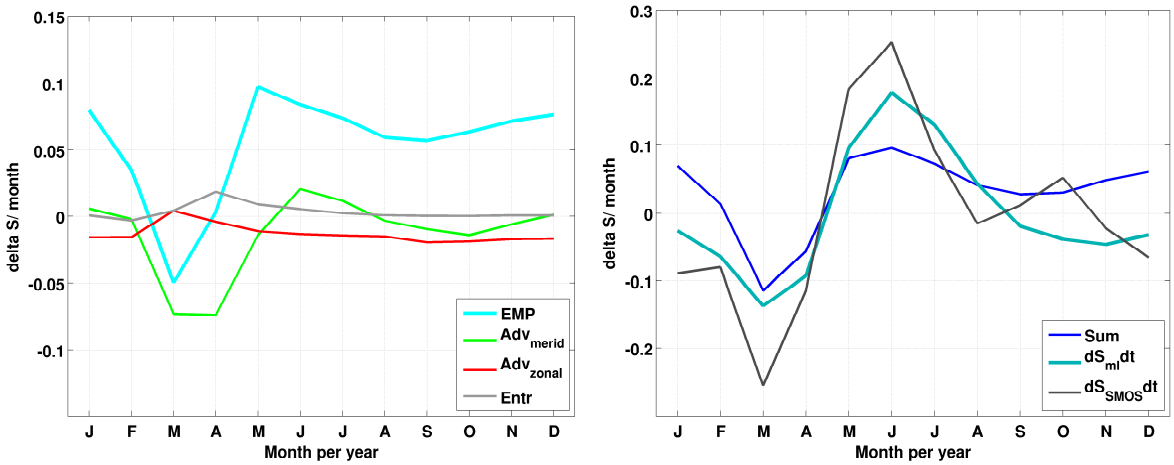

Figure 5.11.: Components of the freshwater budget in the box delimited by 3 °S to 8 °S and 140 °W to 87 °W. Left panel: evaporation-precipitation (EMP, cyan); meridional advection (green); zonal advection (red); entrainment (grey). Right panel: sum of the components (blue); observed salinity tendency from mixed layer salinity (petrol); and from SMOS BEC L3 (black). All values depict salinity change per month [g $kg^{-1}$$month^{-1}$].

The figure shows that the atmospheric freshwater forcing (cyan) causes a maximum decrease of salinity in March when precipitation exceeds evaporation. The forcing is positive throughout the rest of the year, when precipitation is zero while evaporation is constantly high. The meridional advection term (green line) also shows a considerable contribution to the decrease in salinity during February to May. It is caused by the southward freshwater advection across the northern box boundary and is to a minor extent supported by a negative contribution of the zonal advection (red line). Both components, meridional advection and atmospheric forcing, contribute by a similar amount to the decrease in salinity. The S_{ml} decreases already in February and shows minimum values in March and April (petrol curve). The salinity trend derived from SMOS (black curve) is similar to the one in the mixed layer derived from Argo data, though with stronger expressed minimum and maximum values. After June the salinity change due to the meridional advection is nearly zero for the rest of the year, the salinity trend is mainly determined by the excess of evaporation. The zonal freshwater advection always provides a negative contribution, but is very small during the whole year. The export of low salinity water across the western boundary of the box (not shown in detail) happens in July to August, but is playing a minor role in the freshwater budget. The vertical entrainment is only relevant for the freshwater budget in March to May, when it contributes to dilute the freshwater signal. During the rest of the year the contribution of the entrainment is very small. The budget is not totally closed and the curve for the salinity change (in petrol) cannot be completely explained by the sum of the considered terms (blue curve). Especially, the maximum in the salinity trend in June and July from SMOS as well as from the S_{ml} cannot be totally explained by monthly mean meridional freshwater transport, entrainment and

by evaporation. I assume that the imbalance is caused by establishing the budget using the OSCAR velocities which are representative for the mean velocity in the mixed layer, thereby neglecting processes such as eddy mixing and nonlinear terms. In addition horizontal shear is potentially strong between the westward south equatorial branch of the SEC and the eastward equatorial undercurrent surfacing during boreal spring. Moreover, vertical shear is expected to be strong below the mixed layer. Nevertheless and in the face of the above mentioned issues, I find the correspondence between the two curves, the salinity trend and the sum of all processes, quite satisfactory.

Fig. 5.12 shows the freshwater transport across the northern box boundary during the years 2005 to 2013.

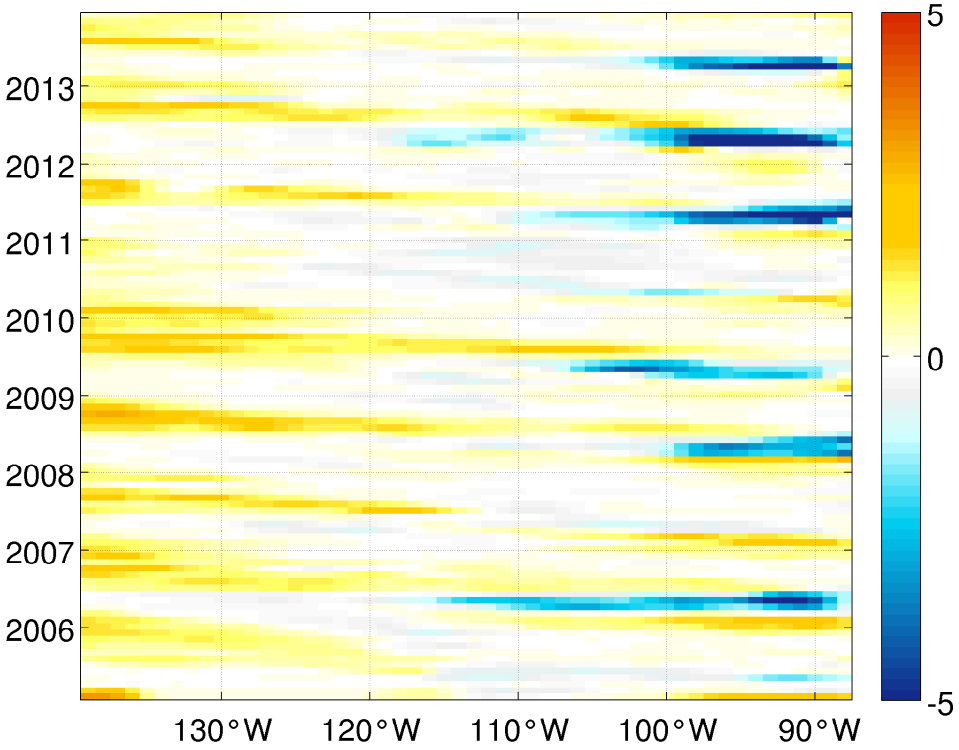

Figure 5.12.: Meridional freshwater transport $[10^3 m^3 s^{-1}]$ across 3 °S from OSCAR velocities and Argo mixed layer salinity assuming a depth of 30 m in which the surface velocities are representative.

As outlined in Fig. 5.11, in March and April the highest southward freshwater transports occur, usually east of 110 °W. Interannual variability though is clearly evident, showing less intensity in 2005, 2007 and 2010. For comparison, the same analysis was carried out using the monthly climatological velocity instead of the OSCAR velocity time series. Results (not shown) reveal much stronger meridional freshwater advection in boreal spring. The salinity

budget (above) using the drifters' climatological data could not be closed either, and a stronger southward advection would require an even stronger salinity minimum as was observed. The advection of the low salinity water is related to an intense surface current probably forced by the Panama gap wind. For illustration, Fig. 5.13 shows the situation in February from the climatological drifters' velocity data, in this data set indicating a strong southward flow near the Galapagos island. The SMOS SSS anomalies averaged for the 4 months of February available between 2010 and 2013 are underlaid and show the coexistence of low salinity and the southward flow across the equator around the Galapagos island. The seasonal circulation within the Panama bight was described by *Rodriguez-Rubio et al.* (2003). They showed that the geostrophic adjustment to the Panama gap wind in February and March leads to a strong southward current and forms an anticyclone reaching down to 3 °N but not crossing the equator. In contrast, the drifters' velocity climatology shown in Fig. 5.13 suggests that the anticyclone can extend southward to the equator, feeding there a westward current just north of the equator. Moreover, Ekman divergence may contribute for the low salinity water crossing the equator around the Galapagos islands in February discharging the freshwater from the EPFP into the present study region. This idea is confirmed by *Yu* (2014) who established the salinity budget for the tropical Pacific ocean north of 5 °S and showed strong Ekman salt advection in February (her Fig. 9a) to contribute to a decrease of salinity in the eastern Pacific at 5 °S. Whereas the oceanic response to the more northerly gap winds in the Gulfs of Papagayo and Tehuantepec are reported to be associated to high kinetic energy and the formation of anticyclonic eddies along 10 °N (*Liang et al.*, 2009), this was not reported for the Panama gap wind response. The flow continues southwestward advecting the low salinity water from the freshwater pool which had formed in December (*Alory et al.*, 2012). The southward current feeds into an intense current along 5 °S, corroborating the previous observation above that the salinity minimum in spring continues more westward than the region of precipitation, thus, that advection is responsible for carrying the low salinity signal westward. How far the climatology is more realistic than the OSCAR velocity data cannot be answered in the present study due to the lack of more observations. The freshwater budget does correspond better to the OSCAR velocities than to the drifter velocity climatology, which errors alias are too small to account for the differences of the results.

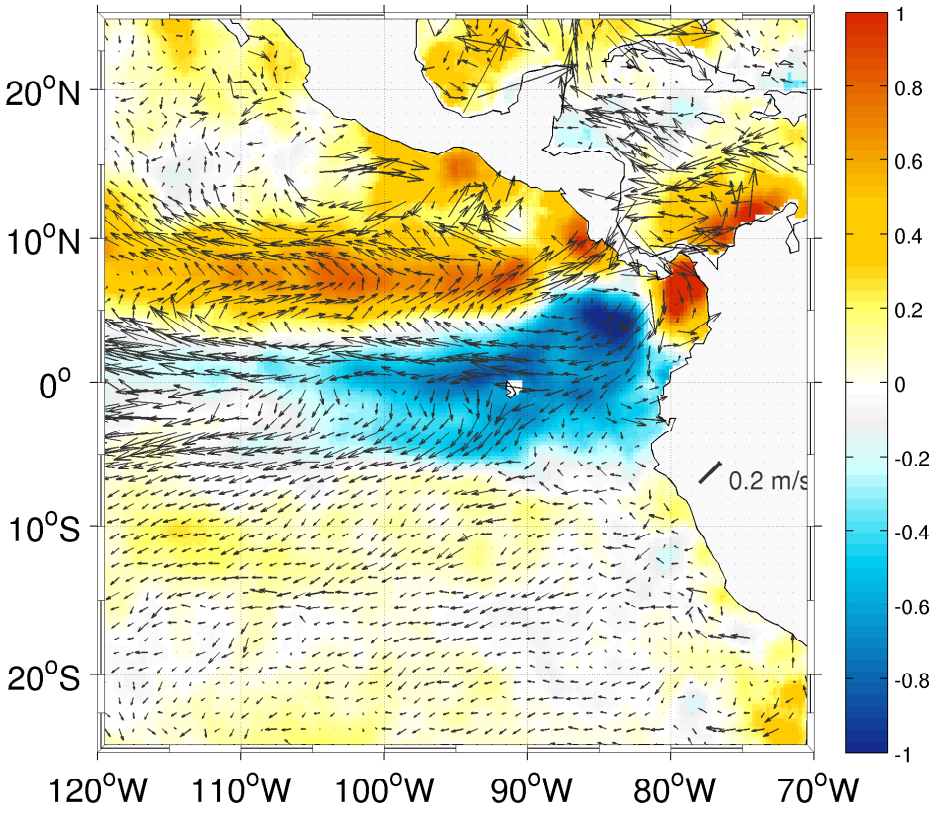

Figure 5.13.: Surface velocity from the climatological drifters' velocity February field (arrows, in [m/s]) and mean February SSS anomaly from SMOS BEC L3 (color shading).

5.6. Summary

The present study investigates the precipitation in the south Pacific dITCZ and associated fresh salinity pattern along about 5 °S. SMOS and Aquarius salinity fields are the first ones to reveal this seasonally appearing band of low salinity in detail between February and May/June. In contrast, objectively interpolated salinity fields derived from Argo data are insufficient to resolve this feature; however, it is shown here that using single profile data this narrow band can be detected also in the Argo data thereby confirming that the SMOS data do depict a real phenomenon in this area. A comparison between SMOS and Aquarius data and uppermost Argo profile data, respectively, reveal a higher satellite-in situ data difference between 5 °S and 1 °N, which will result from uncertainties in satellite and Argo data alike, but also from difference in resolved processes. However, the Argo bias reported by *Yin et al.* (2014) using objectively analyzed fields during August 2010 and September 2011 using ascending orbits only seems to be overestimated; in this study it appears to be about 0.2.

The salinity budget, computed for the eastern tropical Pacific region between 2005 to 2013 revealed that not only local precipitation is the main driver for the low salinity pattern,

but that advection of low salinity water from the eastern fresh pool (*Alory et al.*, 2012) just north of the equator also seems to play an important role. My conclusion is therefore, that more emphasis should to be placed on observing and studying the near-surface velocity field in the eastern tropical Pacific. Based on the available data, and given their uncertainties, I cannot estimate in detail the horizontal advection of salinity. The satellite observations show decreasing salinity in the study area even during ENSO years when precipitation is essentially absent, calling for salinity advection as one of the essential mechanisms for salinity changes in this area. The entrainment rate was also estimated in a simplified manner, as I don't have vertical velocity profile data. However, the salinity budget could not be closed in detail, pointing to other potential error sources such as unresolved processes. At least, the tendency of salinity could mostly be explained by the components considered, and this is a satisfying achievement considering the errors involved in the observational data sets.

We note that the study region is exceptional in that it is very shallow and has a strong pycnocline. In other regions, contributions from advection or entrainment could be much stronger and the relative contribution of E-P considering the deep mixed layer much weaker. Even in this ideal region, with weak mean currents and with a shallow and sharp pycnocline, regionally and temporarily confined precipitation repeating regularly and showing a high correlation with SSS, it is not possible to use the salinity changes as a rain gauge because the contribution by advection has an effect of equal size.

Salinity retrieved from satellite measurements represent the very first centimeters of the ocean, though -in the present study- it is very similar to the S_{ml} from in situ values when averaged monthly and regionally, even in months of rain. That means, that the mixing of the freshened surface salinity is on time scales less than a month and that we cannot resolve the temporal nor the vertical derivatives. More process studies about the mixing scales in the vertical and in the time domain are still necessary. In the present study, it was only possible to examine the contributions of monthly averaged components to the salinity budget.

6. Summary and outlook

The satellite missions SMOS by ESA and Aquarius by NASA have the objective of providing global salinity fields averaged on a weekly or monthly basis and regularly gridded with an accuracy sufficient to monitor annual and interannual changes in sea surface salinity (SSS). However, the technology has its caveats, and basic research, calibration and validation still has to be performed in order to improve the quality of SSS data.

Until some years ago, SSS maps were solely based on in situ data which were objectively mapped on scales adapted to the availability of data and not to the statistics of the data itself. Therefore, the knowledge of the detailed SSS variability is of relevance when constructing SSS maps and also when validating space borne salinity data. The first question addressed in the present dissertation concerned the

Characteristics of the sea surface salinity variability in the existing in situ data and specifically the salinity variability within the averaging time and space intervals used for typical fields of salinity products:

The sea surface salinity variability within the satellite footprint size or within the grid size used for averaging is poorly documented due to the scarcity of in situ data. The present study contributes to providing detailed information about the characteristics of the SSS variability, here focusing the Atlantic Ocean.

The amplitude of the annual salinity cycle was calculated from more of 30 years of in situ data in the Atlantic ocean and the study was extended into poorly sampled regions by using a high resolution model. The geographical distribution of the annual amplitude confirms earlier point-wise estimates, however, now provides a more accurate view for the Atlantic than the previous estimates which were based on objectively analyzed maps using a large decorrelation radius. The ratio up to which the observed annual salinity cycle explains the total salinity variance ranges from 60 to 70 % in the tropics and in some western coastal regions to less than 10 % in the open ocean. The simulated salinity variability in the circulation model shows higher percentages of the total variability being explained by the annual variability, than the observational results show. This is due to a lower simulated salinity variability on the small scales especially in the tropics. The decorrelation radii of salinity variability in the model are also slightly higher than the decorrelation scales found in high-resolution in situ measurements. This overall underestimation of the small scale salinity variability in the model, in spite of its high spatial and temporal resolution, is partly due to the relaxation of the salinity values to monthly climatological values at the surface and at its boundaries, which damps the salinity variability. However, this relaxation is necessary because the freshwater forcing of the model simulation is based on uncertain data of precipitation and evaporation and also on not fully known river discharge which would otherwise lead to a long-term drift in the model salinity fields. Here again, the necessity of high accurate and high resolution salinity data becomes

obvious, to which the model could be relaxed to. Another reason for the suppression of small scale variability is the mixing scheme applied in the model. The biharmonic operator is a scale selecting mixing scheme. Nevertheless, it damps the small scale variability especially in the tropics, and therefore increases the averaged decorrelation scales.

The decorrelation scales of salinity variability amount to regionally different values, in the open ocean the model results show 70 to 200 km whereas at the ocean boundaries and in frontal regions, the scales are considerably lower. The observational results could partly confirm the ones from the model, showing in general about 10 % smaller decorrelation scales. In the Atlantic Ocean, the mean quasi meridional observed decorrelation scales are 100 km with a high uncertainty and the mean simulated decorrelation scales are 120 km. A mean sampling of 38 km, as performed in the SMOS mission, could capture the larger scales of variability in the open ocean, but it gets critical when investigating small scale processes in fronts or coastal regions of high SSS variability.

The intra-monthly small-scale temporal decorrelation scales resulting from the model and the observational data are around 4 days, so that the monthly averages contain about 7 to 8 independent values. A sampling of 3 days is critical to capture this small scale variability, however, monthly averages based on this sampling frequency promise to have a good reliability.

The modeled SSS standard deviation within the scales of averaging (100 km$\times$100 km) is $>$ 0.1 in almost half of the Atlantic Ocean. In frontal regions or regions of strong river-runoff this std value rises to 1. Taking into consideration that the small scale variability is underestimated in the circulation model, also for the sampling error in the open ocean the value of 0.1 represents a lower limit for the true sampling error. My conclusion therefore is, that the validation of satellite derived salinity data with single in situ data cannot reach a better accuracy than 0.1 in the open ocean.

This conclusion already leads to the answer of the second question: **The accuracy of the SMOS sea surface salinity and the suitability of the in situ data for validation and bias correction**

The salinity retrieval from satellite is very complex and based on many models for geophysical and atmospheric corrections, introducing uncertainties and biases. Therefore, the validation of the salinity data is an important and still on-going process, helping to improve the retrieval in the subsequent steps of reprocessing. The validation is based on the comparison to in situ salinity data, which poses in question how far the existing salinity data is representative for the space born salinity fields. One difference between the space born and in situ salinity is their depths of origin: Due to the short penetration depth of microwave radiation into the ocean, satellite retrieved salinity is measured at the first centimeters of the ocean, whereas the in situ data are commonly measured at several meters depth. Another difference is due to the fact that the satellite measures salinity as a spatial average over the satellite's footprint, whereas in situ sensors provide data at a single point.

In the present study I analyzed the global Argo profiler data for salinity gradients within the upper 12 m. Negative salinity gradients were detected in regions of known high precipitation, in regions of river runoff and salinity fronts. However, only 1 % percent of the profiles revealed a salinity gradient. The vertical salinity gradients at the depth levels of the upper Argo measurements are mostly small except in regions of strong or intermittent precipitation,

and in most cases the mixing in the surface layer is strong and rapid enough to dissolve the vertical gradient quickly, i.e. within hours. Most precipitation events are hardly detectable by in situ measurements, because the uppermost measurements are at several meters depth. Whereas the salinity gradient in the upper layer is not the major problem for the validation except for the mentioned regions, the point to area problem is a matter of concern due to the sampling error.

The present study a validation effort on the basis of SMOS L2 salinity data. The comparison of the single orbit data and the Argo profiler data within $\pm$ 3 days has the advantage of a very close collocation aiming at reducing the sample error. The resulting bias shows a dependency on SST, on wind speed and on latitude, different for the ascending and descending half orbits. The SST dependent bias could be associated to the model of the dielectric constant, which works well for moderate ocean temperatures but less so at low SST. At SST $<4\,^{\circ}$C the satellite SSS shows a strong positive bias. The evolution of the bias with time shows a seasonal dependence, mostly due to insufficient atmospheric and ionospheric correction, and near land due to the seasonal variation of the constellation between satellite, sun and coast line. The disturbing effects on the salinity retrieval mix and no functional relationship could be developed. Therefore, an empirical approach for the bias mitigation is proposed to correct the L2 salinity data, including an error estimate from the underlying observational data base. Monthly SSS maps were produced by weighting the data with their inverse errors. The global bias could be reduced considerably, however, the bias mitigation near land needs improvement. The data basis for a bias correction is sparse in these areas, an issue also pointed out by (*Kolodziejczyk et al.*, 2016). The global RMS difference between the resulting L3 SMOS data (monthly averages) and the EN4 objectively analyzed fields amounts to 0.7. Excluding the most critical regions poleward of 40 °latitude, the global RMS salinity difference amounts to 0.47 which is still higher in comparison to other bias corrected products, however, when considering a regional estimate with surface drifters, the RMS difference could be reduced to 0.28. The sampling error of the in situ data is often non-negligible, it is estimated in the present study to be between 0.13 and 0.2 in the open ocean based on TSG and drifter measurements, confirmed by (e.g. *Boutin et al.*, 2015) who found in more than 35 % of the sampled grid boxes a salinity variability of >0.15. The estimated error of the monthly objectively analyzed fields is also high, especially in coastal areas, with or sparse data sampling or high salinity variability.

The third issue investigated in the present thesis is **at what extent the atmospheric freshwater forcing contributes to changes in the sea surface salinity**.

The relation between the net atmospheric freshwater forcing (precipitation minus evaporation) and SSS is not as straightforward as presumed, because ocean processes such as advection and mixing contribute with relevant amounts to the salinity budget. An experiment of computing the salinity budget was conducted for a small box in the southeastern tropical Pacific which is well suited for a relative simple approach, due to its shallow mixed layer depth, weak currents and weak winds. The SSS is representing the mixed layer salinity well in the range of the estimated error. Mixing seems to be carried out rapidly, i.e. within one month, because no lag between precipitation, SSS and mixed layer salinity is evident. However, even in this region, the advection of fresh water explains as much of the salinity anomaly as the net sum of evaporation minus precipitation. Moreover, the freshwater balance could not be closed because

the nonlinear terms, the mixing and diffusion as well as entrainment could not be estimated or only estimated with a high uncertainty by the monthly mean observational data fields. Establishing such a freshwater or salinity budgets with high resolution models can contribute to the understanding and quantifying of the processes involved in the salinity conservation equation.

Outlook

Reducing the errors in the SMOS satellite derived fields and carrying out a bias correction on the basis of in situ salinity fields promises to contribute to the quality of the space borne SSS fields. The next version of the SMOS SSS data set (Version 6.22) contains improvements in many aspects. The full reprocessing chain was carried out for the last 5 years of data, so that a new bias charcterization will be carried out, and a more sophisticated outlier selection will improve the uncertainty in the bias-corrected salinity fields. There are not many other possibilities to validate the radiometric measurements, brightness temperature is measured only at single stations and serve mainly for controlling the longterm drift of the antenna. However, the in situ data basis is still sparse and therefore a clear recommendation is to continue the global Argo mission and the collection of TSG measurements, and to foster high-resolution salinity measurements also in frontal and coastal areas. More studies about the SSS autocorrelation scales and probability distributions of SSS in the satellite footprint size are necessary for estimating the sampling error and scales averaging.

For overcoming the problem of estimating the vertical salinity gradient, we need high-resolution salinity measurements at and near the ocean surface and process studies involving the effects of precipitation. Understanding these phenomena at the temporal scales of a precipitation event and spatial scales of the satellite footprint size will help improve parametrizing the salinity stratification in the upper 10 m in ocean circulation models (as done e.g. in *Song et al.*, 2015).

Vertical turbulent mixing and horizontal advection at mesoscale has been shown to contribute significantly in governing the SSS in regional estimates derived from observations (*Hasson et al.*, 2013b; *Busecke et al.*, 2014; *Gordon and Giulivi*, 2014), however, these estimates are difficult to be calculated due to non-synopticity and poor resolution of the data. In order to understand all processes contributing to change the surface salinity fields, high-resolution ocean circulation models can also help closing the salinity budget calculations.

The ocean dynamics needs to be accurately assessed to link E–P field's variability with change in SSS (*Sommer et al.*, 2015), the most beneficial advantage is reached by using a synthesis of all available data in assimilating them into a general ocean circulation model as done in *Köhl et al.* (2014). From a first version of SMOS data also calculated by the present author, the large errors were artificially reduced in order to effectively adapt the atmospheric forcing in the model to the SMOS SSS fields. The better the error estimates and the lower the errors of the satellite salinity fields are, the better the assimilation can take advantage of the innovative salinity fields and improve simulating the ocean circulation, and furthermore to decrease the uncertainty in the atmospheric forcing fields.

As soon as the bias characterization and mitigation of SMOS, but also of Aquarius and the validation of the third satellite mission, the NASA's Soil Moisture Active Passive (SMAP)

mission, has been advanced, the salinity fields of all missions can be merged to provide a high resolution SSS product. Thorough validation efforts should continue on all processing levels of the satellite data in order to get a profound base of geophysical and atmospheric models with which the salinity can successfully be retrieved.

A. Appendix

A.1. Salinity measurements with SVP drifter

A.1.1. Launch of the SVP drifter

Drifter ID	Station	Date (MM/DD/YYYY) - Time (UTC)	Latitude	Longitude	Water Depth [m]
82040	PS 76/027-5	06/20/2010-17:08	74°59.99´ N	06°3.65´ W	3526
82041	PS 76/027-5	06/20/2010-17:10	74°59.99´ N	06°3.56´ W	3526
82042	PS 76/027-5	06/20/2010-17:12	74°59.98´ N	06°3.48´ W	3526
82043	PS 76/027-5	06/20/2010-17:14	74°59.96´ N	06°3.30´ W	3526
83298	PS 76/050	06/24/2010-13:33	74°59.57´ N	02°9.06´ W	3714
82044	PS 76/050	06/24/2010-13:35	74°59.62´ N	02°8.78´ W	3713
92783	PS 76/050	06/24/2010-13:37	74°59.64´ N	02°8.66´ W	3712
92785	PS 76/050	06/24/2010-13:37	74°59.66´ N	02°8.53´ W	3711
92786	PS 76/052	06/24/2010-20:07	74°59.34´ N	0°54.94´ W	3748
92791	PS 76/052	06/24/2010-20:10	74°59.30´ N	0°54.42´ W	3748
92794	PS 76/052	06/24/2010-20:14	74°59.38´ N	0°54.32´ W	3748
92796	PS 76/057	06/25/2010-16:00	75°1.46´ N	1°0.97´ E	3775
92799	PS 76/057	06/25/2010-16:02	75°1.45´ N	1°1.14´ E	3775
92800	PS 76/057	06/25/2010-16:00	75°1.42´ N	1°1.52´ E	3775
83299	KV Svalbard	09/14/2010-18:58	78°36.65´ N	2°24.74´ E	
92784	Sonne	03/05/2010-1:10	13°59.98'S	163°59.91'W	5550
92787	Sonne	03/05/2010-2:33	14°00.00'S	163°50.04'W	5462
92788	Sonne	03/05/2010-3:54	14°00.00'S	163°40.00'W	5025
92789	Sonne	03/05/2010-4:53	14°00.00'S	163°30.00'W	5163
92790	Sonne	03/05/2010-5:52	14°00.00'S	163°20.00'W	5107
92792	Sonne	03/06/2010-0:56	14°00.00'S	160°0.00'W	5144
92793	Sonne	03/06/2010-2:00	14°00.00'S	159°49.98'W	5126
92795	Sonne	03/06/2010-2:59	14°00.00'S	159°40.00'W	5101
92797	Sonne	03/06/2010-3:58	14°00.00'S	159°30.00'W	5174
92798	Sonne	03/06/2010-4:57	14°00.00'S	159°20.00'W	5106

Table A.1.: Launch positions and time for the SVP drifters with identifying number (ID) equipped with a salinity sensor unit. 15 drifters were launched from the research vessels (RV) Polarstern (PS) and the Norwegian vessel (KV) Svalbard in the Greenland Sea; and 10 drifters were launched from the German RV Sonne in the tropical Pacific.

	Drifter Id.	Date (MM/DD/YY-2000)	Days alive	Days w drogue	Battery Voltage	Sal Days	Temp Days	Trans Rate	Rate S nans
NA	82041	06/20/10-12/04/10	168	119	10V	167	167	98%	41%
NA	82042	06/20/10-11/20/11	519	476	8V	515	518	99%	37%
NA	82043	06/20/10-09/15/12	819	699	0V	702	818	96%	50%
NA	82044	06/24/10-02/23/11	245	145	8V	244	244	97%	34%
NA	83298	06/24/10-05/21/12	697	467	0V	697	697	89%	34%
NA	83299	09/14/10-10/10/10	27	26	12V	26	26	100%	44%
NA	92783	06/24/10-03/17/12	633	579	0V	579	633	89%	31%
PO	92784	03/08/10-11/22/11	625	232	0V	433	625	65%	33%
NA	92785	06/24/10-07/25/11	397	350	2V	390	396	81%	91%
NA	92786	06/24/10-09/14/12	813	117	0V	117	813	78%	39%
PO	92787	03/08/10-08/23/12	899	428	0V	615	899	70%	49%
PO	92788	03/09/10-10/27/11	597	583	0V	400	597	66%	55%
PO	92789	03/09/10-07/05/12	849	340	0V	540	849	68%	58%
PO	92790	03/08/10-11/30/11	633	223	0V	514	633	65%	61%
NA	92791	06/24/10-11/03/11	498	497	0V	427	497	87%	61%
PO	92792	03/09/10-10/13/11	583	531	2V	467	582	68%	49%
PO	92793	03/09/10-01/24/12	686	234	0V	405	686	58%	53%
PO	92795	03/10/10-05/29/11	445	252	0V	232	445	77%	73%
PO	92797	03/09/10-09/20/12	927	283	4V	879	927	63%	68%
PO	92798	03/09/10-01/17/12	679	584	0V	558	679	59%	52%
NA	92800	06/25/10-01/11/12	566	565	0V	447	565	85%	46%

Table A.2.: Life time and transmission quality and duration of data from SVP drifters. NA stands for North Atlantic and PO for Pacific Ocean. The battery voltage is the last voltage indicating if the drifter was damaged before battery voltage ended or worked until battery voltage deceased.

A.1.2. Quality of SVP drifter's data

Submergence and Temperature data

The mean submergence of 95 % during the last 5 days is the indicator for the existence of the drogue. After over one year of measurements, 4 drifters are working with their drogue still attached, namely, the drifters 83298, 92783, 92791 and 92800, all operating in the Greenland Sea. They show lower submergence during the winter months (December 2010 to April 2011) (see A2a in the attachment). If this is due to a thin ice cap, modified electronic behavior with negative temperatures or due to the low stability of the water column is an open question. Due to the second temperature sensor, it became obvious, that the SBE temperature sensor was working and calculating the exact salinity with negative temperature, but negative temperatures were not recorded, instead the minus sign was missing. The operating temperature range of this instrument was configured working in the range of only 0 °to 30 °C. This was communicated to the manufacturer of the surface drifters (Pacific Gyre) and newer drifters

will be configured to work in the range of -5 °to 30 °C. Those wrong temperature values were corrected in the following way:

In the case of the newer drifter type, this was no problem: Whenever the second temperature was negative, the SBE temperature record was corrected to negative values, too. Eventual temperature gradients between the two sensors near 0 °C were deleted this way. For the older drifter types without a second sensor, AMSRE data were extracted corresponding to thamelioratese date and position of the drifter. Whenever the AMSRE data showed negative values, the drifter data were corrected to negative values, too. This is a rather crude method, because the accuracy of the satellite temperature data only is of about 0.5 °C. Though a ten day moving average of the AMSRE data was taken, the temperatures between the 2 sources do not always coincide. A flag is set when the temperatures were corrected.

Stability of salinity measurements:

The drifter's salinity standard deviations (std) over one week were calculated with the aim to inspect irregularities during time. The drifters showed regional differences in the std: in the Greenland Sea salinity is regionally very stable whereas the salinity in the subtropical Pacific is varying relatively strongly. Single periods of high std may be due to sparse data or to regional salinity changes. But no trends could be detected in the salinity std during its lifetime, showing the salinity sensor being very stable.

Comparison with climatological values

In order to check for possible drifts in the conductivity cells, the salinity data were compared over time to the coinciding Argo data, chosen as described above, and to WOA09 climatology (*Antonov et al.*, 2010). The results are not conclusive, no significant drift could be inferred. This is due to the fact, that the climatological field is not representative for the situation in 2010/2011. During 2010 the southward extension of the Pacific Warm Pool is much greater and the axis of the subtropical salinity maximum is shifted to the south. Therefore, only Argo data may serve as a reference for sea surface salinity. The bias inferred from the comparison with the Argo data is less than the standard deviation. So, the salinity data of the drifters is assumed to be correct within this interval of standard deviation.

List of Figures

List of Tables

Bibliography

().

Adler, R. F., et al. (2003), The Version-2 Global Precipitation Climatology Project (GPCP) monthly precipitation analysis (1979-present), *J. Hydrometeorol.*, *4*(6), 1147–1167, doi:http://dx.doi.org/10.1175/1525-7541(2003)004$\langle$1147:TVGPCP$\rangle$2.0.CO;2.

Aksoy, M., and J. T. Johnson (2013), A comparative analysis of low-level radio frequency interference in SMOS and Aquarius microwave radiometer measurements, *IEEE Trans. Geosci. Remote Sens.*, *51*(10), 4983–4992, doi:10.1109/TGRS.2013.2266278.

Alory, G., C. Maes, T. Delcroix, N. Reul, and S. Illig (2012), Seasonal dynamics of sea surface salinity off Panama: The far Eastern Pacific Fresh Pool, *J. Geophys. Res. Oceans*, *117*(C4), C04,028, doi:10.1029/2011JC007802.

Anderson, J. E., and S. C. Riser (2014), Near-surface variability of temperature and salinity in the near-tropical ocean: Observations from profiling floats, *J. Geophys. Res. Oceans*, *119*(11), 7433–7448, doi:10.1002/2014JC010112.

Anterrieu, E. (2007), On the reduction of the reconstruction bias in synthetic aperture imaging radiometry, *IEEE Trans. Geosci. Remote Sens.*, *45*(3), 592–601, doi:10.1109/TGRS.2006.888850.

Anterrieu, E., M. Suess, F. Cabot, P. Spurgeon, and A. Khazaal (2015), An additive mask correction approach for reducing the systematic floor error in imaging radiometry by aperture synthesis, *IEEE Geosci. Remote Sens. Lett.*, *12*(7), 1441–1445, doi:10.1109/LGRS.2015.2406912.

Antonov, J. I., et al. (2010), *World Ocean Atlas 2009 Volume 2: Salinity*, 184 pp., Sydney Levitus, NOAA Atlas NESDIS 69, U.S. Government Printing Office, Washington, D.C.

Asher, W. E., A. T. Jessup, R. Branch, and D. Clark (2014), Observations of rain-induced near-surface salinity anomalies, *J Geophys. Res. Oceans*, *119*(8), 5483–5500, doi:10.1002/2014JC009954.

Ballabrera, J. (2015), Sea surface salinity: Results and recommendations, *Euro-Argo Improvements for the GMES Marine Service*, (D4.4.3), ref: E-AIMS: D4.443-v2.

Bilitza, D. (2001), International reference ionosphere 2000, *Radio Sci.*, *36*(2), 261–275, doi:10.1029/2000RS002432.

Bingham, F. M., G. R. Foltz, and M. J. McPhaden (2012), Characteristics of the seasonal cycle of surface layer salinity in the global ocean, *Ocean Sci.*, *8*(5), 915–929, doi:10.5194/os-8-915-2012.

Blumen, W. (1978), A note on horizontal boundary conditions and stability of quasi-geostrophic flow, *J. Atmos. Sci.*, *35*(7), 1314–1318, doi:10.1175/1520-0469(1978)035⟨1314:ANOHBC⟩2.0.CO;2.

Boutin, J., and N. Martin (2006), Argo upper salinity measurements: Perspectives for L-band radiometers calibration and retrieved sea surface salinity validation, *IEEE Geosci. Remote Sens. Lett.*, *3*(2), 202–206, doi:10.1109/LGRS.2005.861930.

Boutin, J., N. Martin, X. Yin, J. Font, N. Reul, and P. Spurgeon (2012), First assessment of SMOS data over open ocean: Part II - sea surface salinity, *IEEE Trans. Geosci. Remote Sens.*, pp. 1662–1675.

Boutin, J., N. Martin, G. Reverdin, X. Yin, and F. Gaillard (2013), Sea surface freshening inferred from SMOS and Argo salinity: Impact of rain, *Ocean Sci.*, *9*(1), 183–192, doi:10.5194/os-9-183-2013.

Boutin, J., N. Martin, G. Reverdin, S. Morisset, X. Yin, L. Centurioni, and N. Reul (2014), Sea surface salinity under rain cells: SMOS satellite and in situ drifters observations, *J. Geophys. Res. Oceans*, pp. 5533–5545, doi:10.1002/2014JC010070.

Boutin, J., et al. (2015), Satellite and in situ salinity: Understanding near-surface stratification and sub-footprint variability, *Bull. Am. Meteorol. Soc.*, doi:10.1175/BAMS-D-15-00032.1.

Boyer, T., S. Levitus, H. Garcia, R. A. Locarnini, C. Stephens, and J. Antonov (2005), Objective analyses of annual, seasonal, and monthly temperature and salinity for the world ocean on a 0.25°grid, *Int. J. Climatol.*, *25*(7), 931–945, doi:10.1002/joc.1173.

Boyer, T. P., and S. Levitus (2002), Harmonic analysis of climatological sea surface salinity, *J. Geophys. Res. Oceans*, *107*(C12), SRF 7–1–SRF 7–14, doi:10.1029/2001JC000829, 8006.

Brandt, P., F. A. Schott, A. Funk, and C. S. Martins (2004), Seasonal to interannual variability of the eddy field in the Labrador Sea from satellite altimetry, *J. Geophys. Res. Oceans*, *109*(C2), doi:10.1029/2002JC001551.

Busecke, J., A. L. Gordon, Z. Li, F. M. Bingham, and J. Font (2014), Subtropical surface layer salinity budget and the role of mesoscale turbulence, *J. Geophys. Res.*, *119*(7), 4124–4140, doi:10.1002/2013JC009715.

Callies, J., and R. Ferrari (2013), Interpreting energy and tracer spectra of upper-ocean turbulence in the submesoscale range (1–200 km), *J. Phys. Oceanogr.*, *43*(11), 2456–2474, doi:10.1175/JPO-D-13-063.1.

Callies, J., R. Ferrari, J. M. Klymak, and J. Gula (2015), Seasonality in submesoscale turbulence, *Nat Commun*, *6*, doi:http://dx.doi.org/10.1038/ncomms786210.1038/ncomms7862.

Camps, A., et al. (2003), L-band sea surface emissivity: Preliminary results of the WISE-2000 campaign and its application to salinity retrieval in the SMOS mission, *Radio Sci.*, *38*(4), 8071–, doi:10.1029/2002RS002629.

Corbella, I., N. Duffo, M. Vall-Llossera, A. Camps, and F. Torres (2004), The visibility function in interferometric aperture synthesis radiometry, *IEEE Trans. Geosci. Remote Sens.*, *42*(8), 1677–1682, doi:10.1109/TGRS.2004.830641.

Corbella, I., F. Torres, N. Duffo, V. Gonzalez-Gambau, I. Duran, M. Pablos, and M. Martin-Neira (2010), Some results on SMOS-MIRAS calibration and imaging, in *Geoscience and Remote Sensing Symposium (IGARSS), 2010 IEEE International*, pp. 3768–3771, doi:10.1109/IGARSS.2010.5651518.

Corbella, I., L. Wu, F. Torres, N. Duffo, and M. Martin-Neira (2015), Faraday rotation retrieval using SMOS radiometric data, *IEEE Geosci. Remote Sens. Lett.*, *12*(3), 458–461, doi:10.1109/LGRS.2014.2345845.

de Boyer Montegut, C., J. Mignot, A. Lazar, and S. Cravatte (2007), Control of salinity on the mixed layer depth in the world ocean: 1. General description, *J. Geophys. Res. Oceans*, *112*(C6), C06,011, doi:10.1029/2006JC003953.

Dee, D. P., et al. (2011), The ERA-Interim reanalysis: configuration and performance of the data assimilation system, *Q. J. Roy. Meteor. Soc.*, *137*(656), 553–597, doi:10.1002/qj.828.

Delcroix, T., and C. Hénin (1991), Seasonal and interannual variations of sea surface salinity in the tropical Pacific ocean, *J. Geophys. Res. Oceans*, *96*(C12), 22,135–22,150, doi:10.1029/91JC02124.

Delcroix, T., M. J. McPhaden, A. Dessier, and Y. Gouriou (2005), Time and space scales for sea surface salinity in the tropical oceans, *Deep-Sea Res. I*, *52*(5), 787–813, doi:10.1016/j.dsr.2004.11.012.

Delhez, E. J., and E. Deleersnijder (2007), Overshootings and spurious oscillations caused by biharmonic mixing, *Ocean Modelling*, *17*(3), 183–198, doi:10.1016/j.ocemod.2007.01.002.

Dessier, A., and J. Donguy (1994), The sea surface salinity in the tropical Atlantic between 10°S and 30°N - seasonal and interannual variations (1977-1989), *Deep-Sea Res. I*, *41*(1), 81–100.

Dickson, R. R., J. Meincke, S.-A. Malmberg, and A. J. Lee (1988), The "great salinity anomaly" in the northern North Atlantic 1968–1982, *Prog. Oceano.*, *20*(2), 103–151, doi:10.1016/0079-6611(88)90049-3.

Dinnat, E., J. Boutin, X. Yin, and D. Le Vine (2014), Inter-comparison of SMOS and Aquarius sea surface salinity: Effects of the dielectric constant and vicarious calibration, in *Microwave Radiometry and Remote Sensing of the Environment (MicroRad), 2014 13th Specialist Meeting on*, pp. 55–60, doi:10.1109/MicroRad.2014.6878907.

Dinnat, E. P., J. Boutin, G. Caudal, J. Etcheto, and P. Waldteufel (2002), Influence of sea surface emissivity model parameters at L-band for the estimation of salinity, *Int. J. Remote Sens.*, *23*(23), 5117–5122, doi:10.1080/01431160210163119.

Dinnat, E. P., J. Boutin, G. Caudal, and J. Etcheto (2003), Issues concerning the sea emissivity modeling at L band for retrieving surface salinity, *Radio Science*, *38*(4), doi: 10.1029/2002RS002637, 8060.

Dong, S., J. Sprintall, and S. T. Gille (2006), Location of the Antarctic polar front from AMSR-E satellite sea surface temperature measurements, *J. Phys. Oceanogr.*, *36*(11), 2075–2089, doi:http://dx.doi.org/10.1175/JPO2973.1, doi: 10.1175/JPO2973.1.

Dow, J., R. Neilan, and G. Gendt (2005), The International GPS Service: Celebrating the 10th anniversary and looking to the next decade, *Adv. Space Res.*, *36*(3), 320–326, doi: 10.1016/j.asr.2005.05.125, Satellite Dynamics in the Era of Interdisciplinary Space Geodesy.

Durack, P. J., and S. E. Wijffels (2010), Fifty-Year Trends in Global Ocean Salinities and Their Relationship to Broad-Scale Warming, *Journal of Climate*, *23*(16), 4342–4362, doi: 10.1175/2010JCLI3377.1.

Durand, F., G. Alory, R. Dussin, and N. Reul (2013), SMOS reveals the signature of Indian Ocean Dipole events, *Ocean Dynam.*, *63*(11), 1203–1212, doi:10.1007/s10236-013-0660-y.

Durden, S., and J. Vesecky (1985), A physical radar cross-section model for a wind-driven sea with swell, *IEEE J. Ocean. Eng.*, *10*(4), 445–451, doi:10.1109/JOE.1985.1145133.

Eden, C. (2007), Eddy length scales in the North Atlantic Ocean, *J. Geophys. Res.*, *112*(C6), C06,004, doi:10.1029/2006JC003901.

Fekete, B., C. Vorosmarty, and W. Grabs (1999), Global, composite runoff fields based on observed river discharge and simulated water balances, *Tech. Rep. 22*, Federal Institute of Hydrology (BfG), Koblenz, Germany.

Fofonoff, P., and R. J. Millard (1983), Algorithms for computation of fundamental properties of seawater.

Font, J., G. Lagerloef, D. Le Vine, A. Camps, and O.-Z. Zanife (2004), The determination of surface salinity with the European SMOS space mission, *IEEE Trans. Geosci. Remote Sens.*, *42*(10), 2196–2205, doi:10.1109/TGRS.2004.834649.

Font, J., A. Camps, A. Borges, M. Martin-Neira, J. Boutin, N. Reul, Y. Kerr, A. Hahne, and S. Mecklenburg (2010), SMOS: The challenging sea surface salinity measurement from space, *Proc. IEEE*, *98*(5), 649–665, doi:10.1109/JPROC.2009.2033096.

Frajka-Williams, E., P. B. Rhines, and C. C. Eriksen (2009), Physical controls and mesoscale variability in the Labrador Sea spring phytoplankton bloom observed by seaglider, *Deep-Sea Res. I*, *56*(12), 2144–2161, doi:http://dx.doi.org/10.1016/j.dsr.2009.07.008.

Good, S. A., M. J. Martin, and N. A. Rayner (2013), EN4: Quality controlled ocean temperature and salinity profiles and monthly objective analyses with uncertainty estimates, *J. Geophys. Res. Oceans*, *118*(12), 6704–6716, doi:10.1002/2013JC009067.

Gordon, A. L., and C. F. Giulivi (2014), Ocean eddy freshwater flux convergence into the North Atlantic subtropics, *J. Geophys. Res. Oceans*, *119*(6), 3327–3335, doi:10.1002/2013JC009596.

Gould, J., et al. (2004), Argo profiling floats bring new era of in situ ocean observations, *EOS, Trans. Am. Geophys. Union*, *85*(19), 185, doi:10.1029/2004EO190002.

Gouriou, Y., and T. Delcroix (2002), Seasonal and ENSO variations of sea surface salinity and temperature in the south Pacific convergence zone during 1976-2000, *J. Geophys. Res. Oceans*, *107*(C12), 8011, doi:10.1029/2001JC000830.

Grodsky, S. A., J. A. Carton, and F. O. Bryan (2014), A curious local surface salinity maximum in the northwestern tropical Atlantic, *J. Geophys. Res. Oceans*, *119*(1), 484–495, doi:10.1002/2013JC009450.

Guimbard, S., J. Gourrion, M. Portabella, A. Turiel, C. Gabarro, and J. Font (2012), SMOS semi-empirical ocean forward model adjustment, *IEEE Trans. Geosci. Remote Sens.*, *50*(5), 1676–1687, doi:10.1109/TGRS.2012.2188410.

Hasson, A., T. Delcroix, and J. Boutin (2013a), Formation and variability of the south Pacific sea surface salinity maximum in recent decades, *J. Geophys. Res. Oceans*, *118*(10), 5109–5116, doi:10.1002/jgrc.20367.

Hasson, A., T. Delcroix, J. Boutin, R. Dussin, and J. Ballabrera-Poy (2014), Analyzing the 2010–2011 La Niña signature in the tropical Pacific sea surface salinity using in situ data, SMOS observations, and a numerical simulation, *119*(6), 3855–3867, doi:10.1002/2013JC009388.

Hasson, A. E., T. Delcroix, and R. Dussin (2013b), An assessment of the mixed layer salinity budget in the tropical Pacific ocean. Observations and modelling (1990-2009), *Ocean Dynam.*, *63*(2-3), 179–194.

Held, I. M., and B. J. Soden (2006), Robust responses of the hydrological cycle to global warming, *J. Climate*, *19*(21), 5686–5699, doi:10.1175/JCLI3990.1.

Henocq, C., J. Boutin, G. Reverdin, F. Petitcolin, S. Arnault, and P. Lattes (2010), Vertical variability of near-surface salinity in the tropics: Consequences for L-band radiometer calibration and validation, *J. Atmos. Oceanic Technol.*, *27*(1), 192–209, doi:10.1175/2009JTECHO670.1.

Hernandez, O., J. Boutin, N. Kolodziejczyk, G. Reverdin, N. Martin, F. Gaillard, N. Reul, and J. L. Vergely (2014), SMOS salinity in the subtropical North Atlantic salinity maximum: 1. comparison with Aquarius and in situ salinity, *J. Geophys. Res. Oceans*, *119*(12), 8878–8896, doi:10.1002/2013JC009610.

Hormann, V., L. R. Centurioni, and G. Reverdin (2015), Evaluation of drifter salinities in the subtropical North Atlantic, *J. Atmos. Ocean Tech.*, *32*(1), 185–192, doi:doi:10.1175/JTECH-D-14-00179.1.

Ingleby, B., and M. Huddleston (2007), Quality control of ocean temperature and salinity profiles - historical and real-time data., *J. Marine Syst.*, *65*, 158–175, doi:10.1016/j.jmarsys.2005.11.019.

IOC, S., and IAPSO (2010), The international thermodynamic equation of seawater – 2010: Calculation and use of thermodynamic properties., *Tech. Rep. 56*, Intergovernmental Oceanographic Commission, Manuals and Guides No., www.teos-10.org.

Jakobsen, P. K., M. H. Ribergaard, D. Quadfasel, T. Schmith, and C. W. Hughes (2003), Near-surface circulation in the northern North Atlantic as inferred from Lagrangian drifters: Variability from the mesoscale to interannual, *J. Geophys. Res. Oceans*, *108*(C8), doi:10.1029/2002JC001554, 3251.

Johnson, J., and M. Zhang (1999), Theoretical study of the small slope approximation for ocean polarimetric thermal emission, *IEEE Trans. Geosci. Remote Sens.*, *37*(5), 2305–2316, doi:10.1109/36.789627.

Kao, H.-Y., and G. S. E. Lagerloef (2015), Salinity fronts in the tropical Pacific ocean, *J. Geophys. Res. Oceans*, pp. n/a–n/a, doi:10.1002/2014JC010114.

Kessler, W. S. (2006), The circulation of the eastern tropical Pacific: A review, *Prog. Oceano.*, *69*(2), 181–217.

Khazâal, A., J. Tenerelli, and F. Cabot (2016), Impact of sun glint on the SMOS retrieved brightness temperature maps for almost four years of data, *Rem. Sens. Environm.*, doi:10.1016/j.rse.2016.02.003.

Klein, L., and C. Swift (1977), An improved model for the dielectric constant of sea water at microwave frequencies, *IEEE Trans. Antennas Propag.*, *25*(1), 104–111, doi:10.1109/TAP.1977.1141539.

Köhl, A., M. Sena Martins, and D. Stammer (2014), Impact of assimilating surface salinity from SMOS on ocean circulation estimates, *J. Geophys. Res. Oceans*, *119*(8), 5449–5464, doi:10.1002/2014JC010040.

Köhler, J., M. Sena Martins, N. Serra, and D. Stammer (2015), Quality assessment of spaceborne sea surface salinity observations over the northern North Atlantic, *J. Geophys. Res. Oceans*, *120*(1), 94–112, doi:10.1002/2014JC010067.

Kolodziejczyk, N., G. Reverdin, J. Boutin, and O. Hernandez (2015), Observation of the surface horizontal thermohaline variability at mesoscale to submesoscale in the northeastern subtropical Atlantic ocean, *J. Geophys. Res. Oceans*, *120*(4), 2588–2600, doi:10.1002/2014JC010455.

Kolodziejczyk, N., J. Boutin, J.-L. Vergely, S. Marchand, N. Martin, and G. Reverdin (2016), Mitigation of systematic errors in SMOS sea surface salinity, *Remote Sensing of Environment*, doi:10.1016/j.rse.2016.02.061.

Lagerloef, G., C. Swift, and D. Le Vine (1995), Sea surface salinity: The next remote sensing challenge., *Oceanography*, *8*(2), 44–50, doi:10.5670/oceanog.1995.17.

Lang, R., Y. Zhou, C. Utku, and D. Le Vine (2016), Accurate measurements of the dielectric constant of seawater at L-band, *Radio Science*, *51*(1), 2–24, doi:10.1002/2015RS005776, 2015RS005776.

Le Vine, D., A. Griffis, C. Swift, and T. Jackson (1994), ESTAR: a synthetic aperture microwave radiometer for remote sensing applications, *Proc. IEEE*, *82*(12), 1787–1801, doi:10.1109/5.338071.

Le Vine, D., E. Dinnat, T. Meissner, S. Yueh, F. Wentz, S. Torrusio, and G. Lagerloef (2015), Status of Aquarius/SAC-D and Aquarius salinity retrievals, *IEEE J. Sel. Topics Appl. Earth Observ.*, *8*(12), 5401–5415, doi:10.1109/JSTARS.2015.2427159.

Lee, T., G. Lagerloef, M. M. Gierach, H.-Y. Kao, S. Yueh, and K. Dohan (2012), Aquarius reveals salinity structure of tropical instability waves, *Geophys. Res. Lett.*, *39*(12), L12,610, doi:10.1029/2012GL052232.

Lefèvre, N., D. Diverrès, and F. Gallois (2010), Origin of CO2 undersaturation in the western tropical Atlantic, *Tellus B*, *62*(5), 595–607, doi:10.1111/j.1600-0889.2010.00475.x.

Liang, J.-H., J. C. McWilliams, and N. Gruber (2009), High-frequency response of the ocean to mountain gap winds in the northeastern tropical Pacific, *J. Geophys. Res. Oceans*, *114*(C12), C12,005, doi:10.1029/2009JC005370.

Lietzke, C. E., C. Deser, and T. H. Vonder Haar (2001), Evolutionary structure of the eastern Pacific double ITCZ based on satellite moisture profile retrievals, *J. Climate*, *14*(5), 743–751, doi:10.1175/1520-0442(2001)014$⟨$0743:ESOTEP$⟩$2.0.CO;2.

Locarnini, R., A. Mishonov, J. Antonov, T. Boyer, H. Garcia, O. Baranova, M. Zweng, and D. Johnson (2010), *World Ocean Atlas 2009 Volume 1: Temperature*, 184 pp., NOAA Atlas NESDIS 69, U.S. Government Printing Office, Washington, D.C.

Lorenz, C., and H. Kunstmann (2012), The hydrological cycle in three state-of-the-art reanalyses: Intercomparison and performance analysis, *J. Hydrometeorol.*, *13*(5), 1397– 1420, doi:10.1175/JHM-D-11-088.1.

Lumpkin, R., and S. L. Garzoli (2005), Near-surface circulation in the tropical Atlantic ocean, *Deep-Sea Res. I*, *52*(3), 495–518, doi:http://dx.doi.org/10.1016/j.dsr.2004.09.001.

Lumpkin, R., and G. C. Johnson (2013), Global ocean surface velocities from drifters: Mean, variance, ENSO response, and seasonal cycle, *J. Geophys. Res. Oceans*, *118*(6), 2992–3006, doi:10.1002/jgrc.20210.

Maes, C., N. Reul, D. Behringer, and T. O'Kane (2014), The salinity signature of the equatorial Pacific cold tongue as revealed by the satellite SMOS mission, *Geoscience Letters*, pp. 1–17, doi:10.1186/s40562-014-0017-5.

Marquardt, D. W. (1963), An algorithm for least-squares estimation of nonlinear parameters, *J. Soc. Ind. Appl. Math.*, *11*(2), 431–441, doi:10.1137/0111030.

Marshall, J., A. Adcroft, C. Hill, L. Perelman, and C. Heisey (1997), A finite-volume, incompressible Navier Stokes model for studies of the ocean on parallel computers, *J. Geophys. Res.*, *102*(C3), 5753–5766.

Masson, S., and P. Delecluse (2001), Influence of the Amazon river runoff on the tropical Atlantic, *Phys. Chem. Earth*, *26*(2), 137–142.

Masunaga, H., and T. S. L'Ecuyer (2010), The southeast Pacific warm band and double ITCZ, *J. Climate*, *23*(5), 1189–1208, doi:10.1175/2009JCLI3124.1.

Masunaga, H., and T. S. L'Ecuyer (2011), Equatorial asymmetry of the east Pacific ITCZ: Observational constraints on the underlying processes, *J. Climate*, *24*(6), 1784–1800, doi:10.1175/2010JCLI3854.1.

Meissner, F. W. D. L. V., T., and J. Scott (2014), Appendum iii to atbd, *Tech. Rep. 060414*, PODAAC, Santa Rosa, California.

Meissner, T., and F. Wentz (2004), The complex dielectric constant of pure and sea water from microwave satellite observations, *IEEE Trans. Geosci. Remote Sens.*, *42*(9), 1836–1849, doi:10.1109/TGRS.2004.831888.

Meissner, T., and F. Wentz (2012), The emissivity of the ocean surface between 6 and 90 GHz over a large range of wind speeds and earth incidence angles, *IEEE Trans. Geosci. Remote Sens.*, *50*(8), 3004–3026, doi:10.1109/TGRS.2011.2179662.

Mignot, J., and C. Frankignoul (2003), On the interannual variability of surface salinity in the Atlantic, *Clim. Dynam.*, *20*(6), 555–565, doi:10.1007/s00382-002-0294-0.

Monahan, E. C., and I. G. O'Muircheartaigh (1986), Whitecaps and the passive remote sensing of the ocean surface, *Int. J. Remote Sensing*, *7*(5), 627–642, doi:10.1080/01431168608954716.

Njoku, E., W. Wilson, S. Yueh, and Y. Rahmat-Samii (2000), A large-antenna microwave radiometer-scatterometer concept for ocean salinity and soil moisture sensing, *IEEE Trans. Geosci. Remote Sens.*, *38*(6), 2645–2655, doi:10.1109/36.885211.

Oliva, R., M. Martin-Neira, I. Corbella, F. Torres, J. Kainulainen, J. Tenerelli, F. Cabot, and F. Martin-Porqueras (2013), SMOS calibration and instrument performance after one year in orbit, *IEEE Trans. Geosci. Remote Sens.*, *51*(1), 654–670, doi:10.1109/TGRS.2012.2198827.

Oliva, R., et al. (2014), Status of RFI in the 1400–1427 MHz passive band: The SMOS perspective, in *General Assembly and Scientific Symposium (URSI GASS), 2014 XXXIth URSI*, pp. 1–4, doi:10.1109/URSIGASS.2014.6929667.

Percival, D. B., and A. T. Walden (1993), *Spectral analysis for physical applications*, Cambridge University Press.

Planck, M. (1901), On the law of distribution of energy in the normal spectrum, *Ann. Phys. (Berlin)*, *4*, 553ff.

Price, James F. (1979), Observations of a rain-formed mixed layer, *J. Phys. Oceanogr.*, *9*(3), 643–649, doi:10.1175/1520-0485(1979)009⟨0643:OOARFM⟩2.0.CO;2.

Qu, T., S. Gao, and I. Fukumori (2011), What governs the North Atlantic salinity maximum in a global GCM?, *Geophys. Res. Lett.*, *38*(7), L07,602, doi:10.1029/2011GL046757.

Reagan, J., T. Boyer, J. Antonov, and M. Zweng (2014), Comparison analysis between Aquarius sea surface salinity and World Ocean Database in situ analyzed sea surface salinity, *J. Geophys. Res. Oceans*, *119*(11), 8122–8140, doi:10.1002/2014JC009961.

Reul, N., J. Tenerelli, J. Boutin, B. Chapron, F. Paul, E. Brion, F. Gaillard, and O. Archer (2012), Overview of the first SMOS sea surface salinity products. Part I: Quality assessment for the second half of 2010, *IEEE Trans. Geosci. Remote Sens.*, *50*(5), 1636–1647, doi: 10.1109/TGRS.2012.2188408.

Reul, N., et al. (2013), Sea surface salinity observations from space with the SMOS satellite: A new means to monitor the marine branch of the water cycle, *Surv. Geophys.*, pp. 1–42, doi:10.1007/s10712-013-9244-0.

Reverdin, G., S. Morisset, J. Boutin, N. Martin, M. Sena-Martins, F. Gaillard, P. Blouch, J. Rolland, and J. Font (2014), Validation of salinity data from surface drifters, *J. Atmos. Ocean Tech.*, *31*(4), 967–983, doi:10.1175/JTECH-D-13-00158.1.

Richardson, P. L., and D. Walsh (1986), Mapping climatological seasonal variations of surface currents in the tropical Atlantic using ship drifts, *J. Geophys. Res. Oceans*, *91*(C9), 10,537–10,550, doi:10.1029/JC091iC09p10537.

Rodriguez-Rubio, E., W. Schneider, and R. Abarca del Rio (2003), On the seasonal circulation within the Panama Bight derived from satellite observations of wind, altimetry and sea surface temperature, *Geophys. Res. Lett.*, *30*(7), 1410, doi:10.1029/2002GL016794.

Rudnick, D. L., and R. Ferrari (1999), Compensation of horizontal temperature and salinity gradients in the ocean mixed layer, *Science*, *283*(5401), 526–529, doi:10.1126/science.283.5401.526.

Sabia, R., A. Cristo, M. Talone, D. Fernandez-Prieto, and M. Portabella (2014), Impact of sea surface temperature and measurement sampling on the SMOS Level 3 salinity products, *IEEE Geosci. Remote Sens. Lett.*, *11*(7), 1245–1249, doi:10.1109/LGRS.2013.2290710.

Schmidt, S., and U. Send (2007), Origin and composition of seasonal Labrador Sea freshwater, *J. Phys. Oceanogr.*, *37*(6), 1445–1454, doi:10.1175/JPO3065.1.

Sena Martins, M., and D. Stammer (2015), Pacific Ocean surface freshwater variability underneath the double ITCZ as seen by satellite sea surface salinity retrievals, *J. Geophys. Res. Oceans*, *120*(8), 5870–5885, doi:10.1002/2015JC010895.

Sena Martins, M., N. Serra, and D. Stammer (2015), Spatial and temporal scales of sea surface salinity variability in the Atlantic ocean, *J. Geophys. Res. Oceans*, *120*(6), 4306–4323, doi:10.1002/2014JC010649.

Serra, N., R. H. Käse, A. Köhl, D. Stammer, and D. Quadfasel (2010), On the low-frequency phase relation between the Denmark strait and the Faroe-bank channel overflows, *Tellus A*, *62*(4), 530–550, doi:10.1111/j.1600-0870.2010.00445.x.

Smith, W. H. F., and D. T. Sandwell (1997), Global sea floor topography from satellite altimetry and ship depth soundings, *Science*, *277*(5334), 1956–1962, doi:10.1126/science.277.5334.1956.

SMOS–BEC Team (2014), SMOS - BEC ocean and land products description, *Tech. Rep. 1.2*, SMOS Barcelona Expert Centre, Barcelona, Spain.

Soldo, Y., A. Khazaal, F. Cabot, and Y. Kerr (2015), An RFI Index to quantify the contamination of SMOS data by radio-frequency interference, *IEEE J. Sel. Topics Appl. Earth Observ.*, *PP*(99), 1–13, doi:10.1109/JSTARS.2015.2425542.

Sommer, A., G. Reverdin, N. Kolodziejczyk, and J. Boutin (2015), Sea surface salinity and temperature budgets in the North Atlantic subtropical gyre during SPURS experiment: August 2012-August 2013., *Front. Mar. Sci.*, *2*(107), doi:10.3389/fmars.2015.00107.

Song, Y. T., T. Lee, J.-H. Moon, T. Qu, and S. Yueh (2015), Modeling skin-layer salinity with an extended surface-salinity layer, *Journal of Geophysical Research: Oceans*, *120*(2), 1079–1095, doi:10.1002/2014JC010346.

Stammer, D. (1997), Global characteristics of ocean variability estimated from regional topex/poseidon altimeter measurements, *J. Phys. Oceanogr.*, *27*(8), 1743–1769, doi:10.1175/1520-0485(1997)027$⟨$1743:GCOOVE$⟩$2.0.CO;2.

Steele, Michael, Morley, Rebecca, and Ermold, Wendy (2001), PHC: A Global Ocean Hydrography with a High-Quality Arctic Ocean, *J. Climate*, *14*(9), 2079–2087, doi:10.1175/1520-0442(2001)014⟨2079:PAGOHW⟩2.0.CO;2, doi: 10.1175/1520-0442(2001)014¡2079:PAGOHW¿2.0.CO;2.

Stommel, H. M. (1993), A conjectural regulating mechanism for determining the thermohaline structure of the oceanic mixed layer, *J. Phys. Oceanogr.*, *23*, 142–148, doi:10.1175/1520-0485(1993)023⟨0142:ACRMFD⟩2.0.CO;2.

Talone, M. (2010), *Contribution to the Improvement of the Soil Moisture and Ocean Salinity SMOS Mission Sea Surface Salinity Retrieval Algorithm*, Universidad Politecnica de Cataluna, Barcelona, Spain, PhD thesis.

Tang, W., S. H. Yueh, A. G. Fore, and A. Hayashi (2014), Validation of Aquarius sea surface salinity with in situ measurements from Argo floats and moored buoys, *J. Geophys. Res. Oceans*, pp. 6171–6189, doi:10.1002/2014JC010101.

Tenerelli, J., N. Reul, A. Mouche, and B. Chapron (2008), Earth-viewing L-band radiometer sensing of sea surface scattered celestial sky radiation – Part I: General characteristics, *IEEE Trans. Geosci. Remote Sens.*, *46*(3), 659–674, doi:10.1109/TGRS.2007.914803.

Thomson, D. J. (1982), Spectrum estimation and harmonic analysis, *Proc. IEEE*, *70*(9), 1055–1096, doi:10.1109/PROC.1982.12433.

Tian-Kunze, X., L. Kaleschke, N. Maaß, M. Mäkynen, N. Serra, M. Drusch, and T. Krumpen (2014), SMOS-derived thin sea ice thickness: algorithm baseline, product specifications and initial verification, *The Cryosphere*, *8*(3), 997–1018, doi:10.5194/tc-8-997-2014.

Ulaby, F., R. Moore, and A. K. Fung (1982), *Microwave Remote Sensing: Active and Passive – volume II: Radar remote sensing and surface scattering and emission theory*, Addison-Wesley Publishing Company, ISBN: 978-0-472-11935-6.

UNESCO, S., ICES, and IAPSO (1981), The Practical Salinity Scale 1978 and the international equation of state of seawater 1980., *Tech. Rep. 36*, Intergovernmental Oceanographic Commission, UNESCO technical papers in marine science.

Vergely, J.-L., P. Waldteufel, J. Boutin, X. Yin, P. Spurgeon, and S. Delwart (2014), New total electron content retrieval improves SMOS sea surface salinity, *J. Geophys. Res.*, *119*(10), 7295–7307, doi:10.1002/2014JC010150.

Vine, D. M. L., and S. Abraham (2002), The effect of the ionosphere on remote sensing of sea surface salinity from space: absorption and emission at L-band, *IEEE Trans. Geosci. Remote Sens.*, *40*(4), 771–782, doi:10.1109/TGRS.2002.1006342.

Vinogradova, N. T., and R. M. Ponte (2012), Assessing temporal aliasing in satellite-based surface salinity measurements, *J. Atmos. Ocean Tech.*, *29*(9), 1391–1400, doi:10.1175/JTECH-D-11-00055.1.

Vinogradova, N. T., and R. M. Ponte (2013a), Clarifying the link between surface salinity and freshwater fluxes on monthly to interannual time scales, *J. Geophys. Res. Oceans*, *118*(6), 3190–3201, doi:10.1002/jgrc.20200.

Vinogradova, N. T., and R. M. Ponte (2013b), Small-scale variability in sea surface salinity and implications for satellite-derived measurement, *J. Atmos. Ocean Tech.*, *30*(11), 2689–2694, doi:10.1175/JTECH-D-13-00110.1.

von Schuckmann, K., P. Brandt, and C. Eden (2008), Generation of tropical instability waves in the Atlantic Ocean, *J. Geophys. Res. Oceans*, *113*(C8), doi:10.1029/2007JC004712, c08034.

Wüst, G. (1936), Oberflächensalzgehalt, Verdunstung und Niederschlag auf dem Weltmeere, in *Festschrift Norbert Krebs (Länderkundliche Forschung)*, pp. 347–359, Stuttgart, Germany.

Xie, P., et al. (2014), An in situ-satellite blended analysis of global sea surface salinity, *J. Geophys. Res. Oceans*, *119*(9), 6140–6160, doi:10.1002/2014JC010046.

Yeager, S. G., and W. G. Large (2007), Observational Evidence of Winter Spice Injection, *J. Phys. Oceanogr.*, *37*(12), 2895–2919, doi:10.1175/2007JPO3629.1.

Yin, X., J. Boutin, and P. Spurgeon (2013), Biases between measured and simulated SMOS brightness temperatures over ocean: Influence of sun, *IEEE J. Sel. Topics Appl. Earth Observ. in Remote Sens.*, *6*(3), 1341–1350.

Yin, X., J. Boutin, N. Martin, P. Spurgeon, J.-L. Vergely, and F. Gaillard (2014), Errors in SMOS sea surface salinity and their dependency on a priori wind speed, *Remote Sens. Environ.*, *146*(0), 159–171, doi:http://dx.doi.org/10.1016/j.rse.2013.09.008.

Yu, L. (2011), A global relationship between the ocean water cycle and near-surface salinity, *J. Geophys. Res.*, *116*, doi:10.1029/2010JC006937.

Yu, L. (2014), Coherent evidence from Aquarius and Argo for the existence of a shallow low-salinity convergence zone beneath the Pacific ITCZ, *J. Geophys. Res. Oceans*, *119*(11), 7625–7644, doi:10.1002/2014JC010030.

Yueh, S., W. Tang, A. Fore, A. Hayashi, Y. T. Song, and G. Lagerloef (2014), Aquarius geophysical model function and combined active passive algorithm for ocean surface salinity and wind retrieval, *J. Geophys. Res. Oceans*, pp. 5360–5379, doi:10.1002/2014JC009939.

Zhang, C. (2001), Double ITCZs, *J. Geophys. Res. Atmos.*, *106*(D11), 11,785–11,792, doi:10.1029/2001JD900046.

Zine, S., et al. (2008), Overview of the SMOS sea surface salinity prototype processor, *IEEE Trans. Geosci. Remote Sens.*, *46*(3), 621–645, doi:10.1109/TGRS.2008.915543.

B. Acknowledgements I

The Argo data were collected and made freely available by the International Argo Project and the national initiatives which contribute to it (http://www.argo.net). The EN3 and EN4 data are made available by the Met Office/Hadley Center (www.metoffice.gov.uk/hadobs). Data from the PIRATA array were retrieved from http://www.brest.ird.fr/pirata and BATS station data from http://bats.bios.edu/ bats_form_bottle.html. Other time series were downloaded from the EuroSITES Project website (http://www.eurosites.info/data.php). Sea surface salinity data derived from thermosalinograph instruments installed onboard voluntary observing ships were collected, validated, archived, and made freely available by the French Sea Surface Salinity Observation Service (http://www.legos. obs-mip.fr/observations/sss/), and the RV "Polarstern" data were retrieved from http://www.pangaea.de. I thank all persons having contributed to the efforts in collecting, validating, and distributing the oceanographic data.

The CATDS Sea Surface Salinity maps have been produced by LOCEAN/IPSL (UMR CNRS/UPMC/IRD/MNHN) laboratory and ACRI-st company that participate to the Ocean Salinity Expertise Center (CECOS) of Centre Aval de Traitemenent des Donnees SMOS (CATDS). This product is distributed by the Ocean Salinity Expertise Center (CECOS) of the CNES-IFREMER Centre Aval de Traitemenent des Donnees SMOS (CATDS), at IFREMER, Plouzane (France).

The Aquarius satellite SSS data were supplied through the NASA/CONAE Aquarius/ SAC-D Project and can be downloaded from http://podaac.jpl.nasa.gov. At the time of the study, the SMOS SSS L3 product was available at http://cp34- bec.cmima.csic.es/ocean-reprocessed- dataset. These data were produced by the Barcelona Expert Center (http:// www.smos-bec.icm.csic.es), a joint initiative of the Spanish Research Council (CSIC) and the Technical University of Catalonia (UPC), mainly funded by the Spanish National Program on Space.

The ocean heat flux and evaporation products were provided by the WHOI OAFlux project (http://oaflux.whoi.edu) funded by the NOAA Climate Observations and Monitoring (COM) program. The GPCP combined precipitation data were developed and computed by the NASA/Goddard Space Flight Center's Laboratory for Atmospheres as a contribution to the GEWEX Global Precipitation Climatology Project.

The OSCAR currents can be downloaded from http://podaac.jpl.nasa.gov/. The drifter velocity climatology is available at http://www.aoml.noaa.gov/phod/ dac/.

My work was funded by the DLR Project "SMOS CAL/VAL" 50EE0934 and 50EE1245, and by the DFG-funded "Forschergruppe FOR1740." All numerical simulations were performed at the Deutsches Klimarechenzentrum (DKRZ), Hamburg, Germany, in the frame of DKRZ project 704.

C. Acknowledgements II

Zuallerst sei Herrn Professor Dr. Detlef Stammer gedankt, mir die Möglichkeit gegeben zu haben, am Institut für Meereskunde an der Universität Hamburg in dem wissenschaftliches Projekt “SMOS Cal Val” zu arbeiten. Ihm sei auch für die nach wie vor sehr vertrauensvolle Zusammenarbeit gedankt, durfte ich doch die Abwicklung des Projektes, dessen Inhalte und Resultate auch diese Doktorarbeit füllen, von Anfang an sehr eigenständig durchführen. Hiermit sei auch all meinen Fürsprechern gedankt, insbesondere Nuno Serra und der leider schon verstorbene Peter Herrmann.

Die Arbeit in einen Doktortitel umzusetzen, ergab sich mit den Ergebnissen, die nach und nach hervorgebracht wurden, mit der Folge, dass die vorliegende Arbeit zwei Publikationen beinhaltet. Herr Professor Stammer hat mich in diesem Vorhaben konstruktiv unterstützt, ihm sei auch hier für den Vertrauensvorschuss gedankt.

Die Arbeitsatmosphäre in der Abteilung des Institutes ist sehr konstruktiv und freundlich, mit gutem Kaffee all die Jahre und vielen Gespräche auf dem Flur und nebenbei, dafür sei Euch allen gedankt! Insbesonders bedanke ich mich bei Nuno Serra, der immer bereit ist, eingehend und konstruktiv zu diskutieren, nach Details zu forschen und mich nicht nur bei den Modellauswertungen zu unterstützen; ich bedanke mich bei meiner Bürokollegin Julia Köhler, deren Werdegang als Wissenschaftlerin und als Mutter ich hautnah miterleben durfte, und die immer für gute Stimmung und Witz in unserem Büro sorgte, auch wenn sie viele Stresssituationen durchgestanden hat. Vielen Dank auch an die Kollegen, die meine Arbeit Korrektur gelesen haben, Martin Scharffenberg und Xiangshan Tian-Kunze.

Mein grundlegender Halt und Antrieb ist natürlich meine Familie: Mein Mann hat mich nachhaltig unterstützt und mir mit Vertrauen und Liebe die Kraft gegeben, den vielseitigen Familienalltag und die wissenschaftlichen Herausforderungen gleichzeitig zu meistern. Meine Kinder fanden es schon besonders, dass ihre Mutter sich an der Uni einschreibt, und hatten viel Verständnis, wenn mal wieder die Kante erreicht war. In ihrem Sinne wäre es mir auch nicht möglich gewesen, die Arbeit zu einem früheren Zeitpunkt anzufertigen. Ich danke meinen eigenen Eltern für das Interesse an Naturwissenschaften, das sie schon früh in mir und meinen Brüdern geweckt haben, und das große Vertrauen, das sie schon immer in mich gesetzt haben. Auch meine Schwiegereltern waren Kraftquellen für mich, die mir ein Beispiel für ungewöhnliche Lebensläufe sind, mir schon von Ferne immer viel Mut zusprachen und letztendlich zu Hause tatkräftig geholfen haben.